NYU WIRELESS TR 2016-001

Technical Report

Indoor and Outdoor 5G Diffraction Measurements and Models at 10, 20, and 26 GHz

Sijia Deng, George R. MacCartney, Jr., and Theodore S. Rappaport

sijia@nyu.edu, gmac@nyu.edu, and tsr@nyu.edu

NYU WIRELESS
NYU Tandon School of Engineering
2 MetroTech Center
Brooklyn, NY 11201

May 2016

ABSTRACT

Indoor and Outdoor 5G Diffraction Measurements and Models at 10, 20, and 26 GHz

This report presents diffraction measurements, analysis, and signal strength prediction models around objects such as corners, pillars, and irregular objects, at 10, 20, and 26 GHz. The measurement results and models will be helpful for wireless system engineers to simulate potential channel loss from diffraction around objects and the impact of diffraction at centimeter-wave and millimeter-wave frequencies in indoor and outdoor environments. The measurements were conducted indoors and outdoors by using a continuous wave channel sounder with three pairs of identical directional horn antennas at the transmitter and receiver. The measurement results are compared with theoretical predictions based on the Knife Edge Diffraction (KED) in order to determine how well the theoretical model compares to real-world measurements. An empirical creeping wave model with a fixed reference point is also presented and provides a better fit to the measured data in the outdoor environment for the co-polarized antennas. The model validation and new models may be used in ray-tracers and other wireless network simulators by wireless engineers. From the measurement results, diffraction is expected to be less important at mmWave than cmWave due to smaller wavelengths, and diffraction is not a major propagation mechanism in microcell and femtocell deployments with directional antennas.

Contents

List of Figures

List of Tables

Chapter 1

Introduction

The growth of mobile communications and advances in wireless technology are leading the world towards a fully connected network society. In order to support increasing capacity demand, future wireless systems are expected to operate in higher centimeter-wave (cmWave) and millimeter-wave (mmWave) frequencies, harmoniously with the saturated sub-6 GHz frequencies of current cellular systems [1]. The performance of a radio communications system is strongly determined by the propagation mechanisms that give rise to the received signals [2]. In many situations, mechanisms such as attenuation due to transmission through obstacles [3], depolarization, specular reflection, diffraction, or scattering will significantly improve or limit the quality of the radio link.

The development of cmWave and mmWave communication systems will require accurate models of radio channel properties [4–6]. While the feasibility of signal transmission in the mmWave frequency range has been successfully demonstrated [7–9], the reliable prediction of coverage and system performance based on computer simulation and design tools, such as ray tracers, requires accurate knowledge of reflection, scattering, and diffraction effects. These mechanisms are important to understand at cmWave and mmWave frequencies because of the small transmission wavelength and also the need to overcome the additional free space path loss in the first meter of propagation when compared with traditional UHF/microwave frequencies [10, 11].

Diffraction is a phenomenon that occurs when a wave encounters an obstacle or obstruction, and is often described as the bending of a wave around an obstacle or obstruction [2]. When a mobile user turns around the corner, moving from a line-of-sight (LOS) environment to a non-LOS (NLOS) environment, the user is still able to receive a significant signal strength. Diffraction plays a significant role in directing signals to regions that would otherwise receive little or no signal [12]. In today's cellular systems, diffraction is a relatively strong propagation mechanism, however, as we move to mmWave bands, due to the small wavelength, the attenuation of a diffracted wave may be quite severe and in fact may be too lossy to be relied on for mmWave propagation [1, 13]. The purpose of this report is to investigate on the diffraction mechanism in cmWave and mmWave bands and develop models that can accurately predict diffraction.

1.1 Motivation

This report focuses on diffraction measurements around building corners and irregular objects at 10, 20, and 26 GHz in indoor and outdoor environments. These measurements were performed in order to understand, quantify and model the behavior of diffraction mechanism. This report is concerned with the additional loss that an obstructing building corner introduces into a radio link, which is in excess of free-space path loss, also called diffraction loss.

The basic motivation of this work is the need for development of accurate and general diffraction loss models with simple calculation, which can be used in building ray tracers for cmWave and mmWave. The results of this study are useful for development of ray-based channel models, as well as for calibration of existing ray tracing tools. The ability to accurately predict the effects of the propagation environment on a communications channel is essential in the development and optimal design of future mmWave communications system. Current methods of channel characterization, while having the

advantage of simplicity, do not adequately address the issue and there is a need for significant improvement in the prediction of radio wave propagation.

1.2 Contribution

This report makes the following contributions:

- This report presents measurements at three cmWave and mmWave frequencies: 10, 20, and 26 GHz for indoor and outdoor environments, and compares results in these three frequencies to investigate the frequency dependence of the diffraction models.
- The diffraction measurements are conducted at building corners and irregular objects of different material types, to investigate on the dependence of material and shape of the object.
- The extensive diffraction measurements make the results more reliable compared with the previous diffraction measurements with few data points.
- Comparison of measurement results to electromagnetic theory and measurements made by other researchers.
- Development of simplified mathematical models that can accurately characterizes the diffraction measurement results. Measurement results are used to validate mathematical models.

1.3 Organization

Chapter 2 introduces a comprehensive literature review of diffraction measurements and models. Chapter 3 presents diffraction theory, as well as Knife Edge Diffraction model, Geometry Theory of Diffraction model and a creeping wave model based on diffraction

over a convex surface. Chapter 4 describes the measurement hardware, measurement environments, and measurement procedures. Chapter 5 presents the indoor diffraction measurement results and analysis, and Chapter 6 presents the outdoor diffraction measurement results and analysis. Chapter 7 concludes the entire report.

Chapter 2

Literature Review

2.1 Diffraction Measurements

Over the past few decades, diffraction has been thoroughly studied at conventional bands below 6 GHz [14–16], yet it has not been sufficiently explored in the cmWave and mmWave bands.

2.1.1 Diffraction Measurements below 6 GHz

Future wireless communications are expected to serve densely populated urban areas with the deployment of many small cells. Therefore, resolution of urban areas increases as well as the impact of individual buildings on signal strength. Russell *et al.* proposed a deterministic site-specific propagation prediction approach that applied Fresnel-Kirchhoff diffraction theory to a collection of arbitrarily oriented buildings of simple shapes noindent [15]. In their software, building edges were constructed using finite knife-edge models and every possible diffraction path was simulated using a terrain diffraction method that recursively computed the multiple diffraction introduced by successive diffracting edges. The buildings were approximated with simple rectangular volumes which provided necessary information to compute the diffraction models.

The simulation results were compared with measurements conducted at 914 MHz, showing that the transition regions were well predicted and the diffraction predictions gave worst-case estimations of the signal strength.

Zhang proposed a fast two-dimensional (2-D) diffraction model in a horizontal plane for site-specific propagation prediction for TX and RX antennas lower than the surrounding buildings in urban micro cell (UMi) environments [16]. A number of CW measurements at 900 MHz and 1800 MHz were performed in the city of Helsinki, Finland. The results showed that without a building height database, the fast 2-D diffraction model was in good agreement with measurements in most cases for NLOS locations. There were three novel efforts in the 2-D diffraction model; an extended formula for multiple forward diffraction, a novel equivalent source simplification for parallel street level scenarios, and the inclusion of reflections from curved surfaces of street building corners. The computation time for the 2-D diffraction model was significantly reduced; by introducing the extended formula, the computation time was $1/n$ less than the existing formula. Moreover, the good agreement between measurement results and simulation results validated the accuracy of the 2-D model which overcame the limitation and difficulty of traditional methods for multiple diffraction.

2.1.2 Diffraction Measurements above 6 GHz

Channel characteristics and phenomena at 10 GHz have been investigated for a few decades, but few diffraction measurements were conducted at this frequency [17]. Tervo *et al.* presented results and analysis of diffraction measurements around a building corner at 10 GHz using a 4-port vector network analyzer (VNA) and virtual antenna arrays at the TX and RX. As observed in diffraction measurements at other frequencies, a small change in the antenna position were observed to incur large diffraction loss, especially when the direct path and diffracted path both exist. The virtual antenna arrays were used to enable antenna shifts in only a fraction of a wavelength, in order to observe the propagation as a transit from LOS to NLOS environments. Angle of arrival

analysis was carried out to distinguish the diffracted path from other multipath. The analysis of corner diffraction showed that a building corner at 10 GHz can be modeled by the Knife-Edge Diffraction (KED). The results can be used for path loss estimation of diffracted paths, and can provide a valid diffraction model for ray tracing (RT) analysis at 10 GHz.

Tenerelli *et al.* presented a building corner diffraction measurement campaign at 28 GHz using a continuous wave (CW) transmission and they used a simple model to predict building corner diffraction loss [18]. The measurements employed a 2.5° parabolic antenna at the TX and a horn antenna with a 17° HPBW at the RX. The measurements were conducted at three separate buildings with 90° sharp corners, for T-R separation distances (path lengths) that ranged from 39.1 m to 50.0 m. Common building materials of brick and concrete block (with rougher surfaces) were investigated. The measurement results showed that the diffraction loss increased as diffraction angle increased (as the RX moved into the shadow region of the building corner). Specifically, for "small diffraction angles" (from 0° to 5°), the diffraction loss exhibited a logarithmic growth as diffraction angles increased. For "large diffraction angles" (from 5° to 40°), the diffraction loss grew linearly as the diffraction angles increased. This paper developed a simple mathematical model for two measured diffraction angle clusters: "small diffraction angles" and "large diffraction angles", due to the different performance in these two regions. In addition, the results indicated that the dependence on building materials was small, but still noticeable. The concrete block corner attenuated the signal by 3 dB more than the brick corner for diffraction angles from 5° to 40°. The measured diffraction loss indicated a lack of dependence on polarization (typical differences of 1.5 dB between two linear polarizations).

Alejos *et al.* investigated propagation mechanisms and measured electromagnetic properties of common building materials in order to validate the applicability of site-shielding techniques for the 40 GHz frequency band [19]. The idea of site-shielding is to isolate radio terminals from unwanted transmissions and to reduce co-channel interference, by

taking advantage of attenuation and depolarization induced by obstacles. Therefore, site-shielding techniques require an accurate characterization of propagation mechanisms, specifically transmission and reflection. Several measurement campaigns were conducted to characterize different scattering mechanisms, including direct transmission (penetration), depolarization, specular reflection, and wedge diffraction. The campaigns tested various common building materials that included wood, plywood, chip wood, plasterboard, glass, mortar, reinforced concrete, and brick. The measurement results were compared with theoretical models for the previously described scattering mechanisms. The internal successive reflection (ISF) model demonstrated better performance than the Fresnel model for transmission and reflection mechanisms, since the ISF model considered the width of obstacles. The paper presented site-shielding attenuation factors (SSAF) for different building materials, and defined a new shielding parameter called the site-shielding normalized attenuation factor (SSANF) as a function of the material thickness. The attenuation results showed that various materials, such as brick, mortar, and concrete walls, exhibited large attenuation (large SSANF values) in decibels per centimeter, and can be considered as shielded base stations, in order to reduce the frequency reuse distance in radio cellular networks. The measurement results demonstrated that reflection and diffraction cannot be neglected for the 40 GHz band, and indicated that there was a significant diffracted field in the shadow region of brick corners. The Luebbers and Holm diffraction models were found to overestimate the diffraction field in the shadow region, which can in fact be simplified to a linear angular dependence.

Jacob *et al.* presented extensive measurements and ray tracing based investigations of diffraction for 60 GHz and 300 GHz indoor propagation channels for current and future communications systems operated in mmWave and sub-mmWave bands [20]. Three types of diffraction measurements were performed, namely the angular dependence of diffraction, diffraction around closed objects and the effect of human-induced shadowing. The measurements employed a VNA connected with external transmit and receive test heads, and 20 dBi WR-15 and WR-3 standard gain horn antennas with similar antenna patterns. The angular dependent measurements investigated diffraction attenuation

caused by metallic and wooden edges, wedges, and cylinders, which were typical shapes of objects in the indoor environments. The movement of these objects through a direct path on a translation stage were studied. Furthermore, the impact of human-induced shadowing was measured. The measurement results were compared to predictions from the commonly used KED and uniform geometrical theory of diffraction (UTD) models, to validate the applicability of these models at 60 GHz and 300 GHz. A ray tracing tool was employed to assess the impact of diffraction on transmission channels for 60 GHz and 300 GHz communication systems. The results were presented in terms of coverage maps, the average path loss, and the temporal channel characteristics.

Lu *et al.* conducted 60 GHz narrowband measurements to investigate diffraction at building corners, and scattering caused by cars, lampposts, and buildings, as well as blockage by humans [21]. The measurements employed a pair of V-band horn antennas with 24 dBi of gain and 11° half-power beamwidth at TX and RX. For diffraction and scattering measurements, the TX and RX antennas were placed at a height of 1.33 m above the ground to emulate a mobile-to-mobile scenario. A building corner was modeled as a conducting right angle wedge and an absorbing screen with a knife-edge. The results of the diffraction measurements at 60 GHz were found to be well predicted by the absorbing screen diffraction model with standard deviations of error less than 2.6 dB. Scattering measurements around cars and lampposts showed that the minimal scattering loss was found near a specular direction. The comparison of the contributions from scattered rays and diffracted rays in a NLOS environment indicated that vehicular and lamppost scattering was dominant compared to the building corner diffraction. This indicated the need to include scattering models of common urban furniture in mmWave propagation simulators. Human blocking measurements were performed for mobile to mobile (the TX and RX antennas were placed at 1 m height) and access link scenarios (the TX antenna was elevated to 2.65 m and the RX antenna was 0.9 m). The measurements were recorded as human blockers moved from the TX to the RX antenna. The human blockers were modeled as semi-infinite absorbing screens with knife-edges. The results showed that the absorbing screen model was quite accurate in computing

human blockage loss with the error standard deviations between measurements and prediction less than 5 dB.

It was concluded by Hansryd *et al.* from Ericsson that small cell backhaul in bands above 20 GHz outperformed sub-6 GHz systems under most NLOS conditions, and therefore the vast amount of spectrum available above 20 GHz can provide fiber-like multi-gigabit capacity as well as high backhaul performance for small cells in NLOS locations [22]. The paper investigated three main propagation mechanisms in NLOS scenarios, namely, diffraction, reflection, and penetration. Diffraction loss was known to be proportional to both the sharpness of the edge the wave encountered and the frequency of the wave, and consequently, the diffraction loss at higher frequencies (above 6 GHz) was too high to deploy feasible systems considering the diffraction loss. In the paper, diffraction measurements at 5.8 GHz and 28 GHz were presented with the TX antenna positioned on the roof of an office building and the RX antenna located on a mobile lift placed 11 m behind a parking garage with a height of 13 m, which blocked the LOS path. The effect of diffraction was measured by lowering the mobile lift below the LOS path. The measured results compared well with the theoretical knife-edge models, however, due to the simplicity of the model, the theoretical diffraction losses were slightly underestimated. The differences were compensated by simply adding a few extra decibels to the loss margin. The comparison between 28 GHz and 5.8 GHz showed that the 28 GHz system can provide signal at farther NLOS locations than the 5.8 GHz system, due to higher link margin. The full throughput of 400 Mbps was achieved at 28 GHz up to 6 m below the LOS path, while the 5.8 GHz system dropped to under 50 Mbps at 3 m below the LOS path. In terms of diffraction, the 28 GHz system outperformed the 5.8 GHz system with comparable antenna size.

Maltsev *et al.* conducted diffraction measurement in a library room with half of the RX antenna track in the LOS environment and other half of the track blocked by a metallic bookshelf [23]. The bookshelf can be approximately considered as infinitely thin in order to apply KED. It was showed that the signal power drops by 20 dB when bringing the

antenna into the shadow region by 80 mm. This confirmed that the propagation due to diffraction is not significant for 60 GHz WLANs.

It is worth noting that experimental results from [24] have also demonstrated that even human blockage of a millimeter-wave link (at 60 GHz) can be described with a good accuracy with knife edge diffraction theory. The measured attenuation of a human body at 60 GHz was estimated to be in the range from 10 to 30 dB [24, 25]

Kvicera *et al.* presented terrain diffraction measurements condected at 2, 11, and 38 GHz [26]. It was observed that the diffraction loss increased with frequency, and decreased with RX antenna height. A very good match between measurements and predictions can be found for the highest heights of the Rx station, while differences between measurements and predictions were about 10 dB for the case of lowest Rx heights.

Rodriguez *et al.* presented a detailed measurement-based analysis of urban outdoor and outdoor-to-indoor propagation characteristics at 38 GHz [27]. Different sets of measurements were performed in order to understand, quantify and model the behavior of the different underlying propagation mechanisms, considering line-of-sight propagation, reflection, scattering, diffraction, transmission, as well as polarization effects. it was concluded that propagation in urban outdoor scenarios at 38 GHz was mainly determined by line-of-sight propagation and reflection. In the scenario considered, a maximum reflection loss of approximately 20 dB was found for normal incidence over a modern building. Diffraction loss was found to be very strong, and predictable by using simple knife-edge calculations. The different measurements in NLOS conditions, confirmed how reflection becomes dominant over diffraction for interaction angles larger than 5°, which in typical urban scenarios is translated into a distance of just a few meters inside street canyons. Polarization issues were also addressed, finding a very similar behavior for both vertical and horizontal polarizations.

2.2 Geometrical Theory of Diffraction

KED is the most widely adopted model for making deterministic predictions of diffraction loss. There have been many cases in the literature, where the knife edge diffraction model was reported to have a reasonably good agreement with the measurement data. And KED approximation has received wide application for path loss prediction due to its simplicity. However, in other cases, poor agreement was observed, because the KED approximation ignores the material of the object, shape of the object and antenna polarization [28].

In the 1800's, Thomas Young, made his initial attempt to explain the phenomenon of wave bending around edges as diffraction in his single-slit and double-slit experiments. In the 1950's, Joseph Keller first introduced a profound and revolutionary theory of diffraction, which was referred to as the Geometrical Theory of Diffraction (GTD) [29]. The GTD, for the first time, systematically represented diffraction waves in terms of rays, and viewed the diffraction rays as an extension to Geometrical Optics (GO), which is associated with direct, reflected, and refracted rays. The GO rays, which obey Fermat's principle, can describe incidence, reflection, and refraction of electromagnetic (EM) waves and thus result in a zero EM field in shadow regions of impenetrable obstacles. The diffracted rays introduced by Keller, can penetrate into the shadow regions, and therefore overcame the failure of GO for not considering the diffraction effects. The GTD is widely adopted in industries and academia, since it provided a vivid physical image for wave mechanics in terms of rays, and avoids the computational complexity of integration. The GTD field can be expressed as the sum of the GO field and diffracted field, where the GO field is most dominant. GO rays can be characterized by the reflection and transmission coefficient, and diffracted rays can be characterized by diffraction coefficients, which can be solved by the asymptotic high frequency solution. The GTD exhibited a singularity at the shadow-boundary transition region and caustics. The size of the transition regions depends on the angular distance from the shadow boundary and frequency. In order to use the GTD in solving practical EM problems, the Uniform

Geometrical Theory of Diffraction (UTD) was developed to improve Keller's original version of GTD, such that the total field was bounded and continuous.

In 1947, Kouyoumjian and Pathak first introduced the uniform geometrical theory of diffraction for an electromagnetic wave incident on an edge for a perfectly conducting surface [30]. Since then, researchers around the world have proposed various solutions for approximating diffraction coefficient in UTD for diffraction on wedges with impedance faces. These solutions can be generally categorized into rigorous solutions and heuristic solutions. Most of the rigorous solutions were computationally prohibitive for real-time propagation prediction, and because of this the diffracted rays were neglected for simplicity purposes in early propagation prediction models. Heuristic solutions offered efficient evaluation of the diffracted field, but could not provide an accurate estimation of the diffracted field in the shadow region. In order to improve the estimation of wedge diffraction, Wang *et al.* introduced a new solution to approximate the diffracted field within the context of the UTD, and exploited the inverse problem theory to find a better approximation of the diffraction coefficient at a faster computation speed [31]. The comparison with one rigorous solution and two heuristic solutions showed that the proposed modeling method was advantageous, due to a simpler calculation than the rigorous solution and higher accuracy than the two heuristic solutions.

In 1994, Erceg *et al.* from Bell Laboratories proposed two modeling approaches to predict the received signal power in urban and dense suburban environments, by combining ray theory and the uniform geometrical theory of diffraction (UTD) [32]. At lower frequencies (less than 2 GHz), they suggested using the Power-of-Complex-Sum (PS) method, where the total signal power was obtained by summing the individual complex rays, while at higher frequencies (larger than 2 GHz), it was more suitable to use the Sum-of-Individual-Ray-Powers (SP) method, where the total signal power was obtained by summing the individual ray powers. Theoretical predictions were compared with the measurement results at 900 MHz, 2 GHz, and 6 GHz. The 900 MHz CW measurements

were conducted in downtown Manhattan, NY, and the 2 GHz and 6 GHz CW measurement data were performed in Boston, MA. The TX antenna was set at a height of 10 m (below the rooftops of the surrounding buildings), located in the intersection of a crossroad (for 900 MHz and 2 GHz measurements), and the RX antenna was set at a height of 2 m. The measurement results were in agreement with the theoretical analyses and the experimental data for different frequencies and locations. For the 900 MHz measurement, the PS prediction method provided better agreement with the experimental data than the SP method. Both methods demonstrated similar performance in evaluating the signal path loss at 2 GHz. For 2 GHz and 6 GHz measurements, the SP method exhibited better performance (smaller prediction error) than the PS method. Furthermore, the 900 MHz and 2 GHz measurements showed diamond-shaped cell coverage approximations with the TX antenna located in the intersection of a crossroad.

Imai *et al.* proposed a method to calculate multiple diffraction losses, in order to improve the propagation prediction accuracy of ray tracing technique. Ray tracing is a method to predict propagation loss based on Geometrical Optical (GO), where rays launched from the TX reach to the RX through transmission and multiple reflection and diffraction [33]. The arrival time of each ray is calculated based on the length of the GO path from the TX to the RX, and the field strength of each ray is obtained by calculating transmission loss, reflection loss, and diffraction loss through the GO path. The transmission and reflection loss can be calculated by Fresnel's transmission and reflection coefficients, and diffraction loss can be calculated using GTD. An imaging method was developed to determine the exact path through transmission and multiple reflections from the TX to the RX. Imai *et al.* introduced a method to determine the exact path through multiple diffractions. Imai's method of calculating multiple diffraction losses combined with the imaging method, provided a rigorous prediction of the propagation loss.

The Geometrical Theory of Diffraction model has advantages of including finite conductivity, local surface roughness effect, and diffracting edge profile. The GTD is three-dimensional, at the expense of computational complicity, it can be used to predict path

loss effects of three-dimensional irregularities.

Methods for calculation of diffraction coefficients for metal or materials with finite conductivity were developed [28, 30, 34, 35]. A comparison among the perfectly absorbing wedge method, UTD, and UTD heuristic methods can be found in [36]. It is found that errors given by these three methods are comparable.

Rizk *et al.* [37] proposed a method to include the slope diffraction from wedges to improve the accuracy of calculation of the diffracted field in transition regions using classical UTD. Several decibels (approximately 6 dB) of improvement can be achieved. The diffraction from building corners (wedges) is taken into account in [38]. New diffraction coefficients for objects with finite conductivity are developed [32]. The artificial dip in the usual diffraction calculation is removed. Comparison with FDTD shows that the results of the new method are of good accuracy.

Anderson presented measurements of the electric field around a building corner at 1823 MHz with an unmodulated sine-wave carrier and compared the measurement results with the theoretical prediction using the UTD for dielectric wedges and simple specular ground reflections [39]. The measurements were taken every 0.5 m along tracks starting from LOS region to shadow region. A directional horn antenna with a HPBW of about 26° was used at the TX side, and an omnidirectional antenna with 0 dB gain was used at the RX side. A spectrum analyzer were used to measure the amplitude of the received signal. The predicted results showed an oscillatory pattern in the LOS region due to direct and diffracted wave adding in and out of phase but since the spacing between measurement points was too wide to discern the oscillating pattern. At the shadow boundary, the field strength fallen by about 20 dB from its average LOS value. In the shadow region, the filed continues to decrease as bending angle around the corner got increasing acute. These measurements also showed that signal penetration through the corner of the building was negligible.

Nechayev *et al.* presented comparison of the predictions of theoretical wedge diffraction models with measured diffraction coefficients at 2.4 GHz, and demonstrated that

the widely used heuristic diffraction coefficients were not applicable in the case when backscattering occurs [40]. A method of modifying the heuristic diffraction coefficients to mitigate this problem was suggested, which resulted in an improved prediction in the backscattering scenario in the deep shadow region.

Chapter 3

Diffraction Theory and Models

3.1 Knife Edge Diffraction Model

The knife-edge effect can explained by Huygens–Fresnel principle, which states that a well-defined obstruction to an electromagnetic wave acts as a secondary source, that is all points on a planar wavefront can be considered as point sources which produce secondary wavelets, and these wavelets combine to create a new wavefront in the direction of propagation [2]. This new wavefront propagates into the geometric shadow area of the obstacle, resulting in the phenomenon of diffraction. A knife edge difracction object in free space would induce a loss that increases as the square of the frequency.

Assume a transmitter and receiver separated in the free space as shown in Fig. 3.1 and Fig. 3.2. It is advantageous to simplify the geometry by reducing all heights by the smallest height without changing the values of the angles, as shown in Fig. 3.3. Let h be the effective height of the obstructing screen with infinite width placed between the TX and RX at the distance d_1 and d_2, respectively. The wave propagates from the TX to the RX through the top of the screen, which is a longer distance than a direct line-of-sight (LOS) path. Assume that $h << d_1, d_2$ and $h >> \lambda$, with the difference

between the diffracted path and LOS path called excess path length ($\triangle$), which can be calculated from the geometry of Fig. 3.3 as:

$$\triangle \approx \frac{h^2}{2}\frac{(d_1+d_2)}{d_1 d_2} \tag{3.1}$$

The corresponding phase difference ϕ is:

$$\phi = \frac{2\pi\triangle}{\lambda} = \frac{2\pi}{\lambda}\frac{h^2}{2}\frac{(d_1+d_2)}{d_1 d_2} \tag{3.2}$$

and when $\tan x \approx x$, then $\alpha \approx \beta + \gamma$ (from Fig. 3.3), and

$$\alpha \approx h(\frac{(d_1+d_2)}{d_1 d_2}) \tag{3.3}$$

The function for phase difference is commonly normalized to use the dimensionless Fresnel-Kirchoff diffraction parameter ν which can be written as:

$$\nu = h\sqrt{\frac{2(d_1+d_2)}{\lambda d_1 d_2}} = \alpha\sqrt{\frac{2d_1 d_2}{\lambda(d_1+d_2)}} \tag{3.4}$$

Therefore, the phase difference between a direct LOS path and diffracted path can be expressed in a convenient form as

$$\phi = \frac{\pi}{2}\nu^2 \tag{3.5}$$

Diffraction loss as a function of path difference can be explained by Fresnel zones. Fresnel zone is a series of concentric ellipsoidal regions where secondary waves travel a path from the TX to the RX $n\lambda/2$ longer than the direct LOS path, e.g. the first zone is the ellipse with chords $\lambda/2$ longer than the direct path, resulting in constructive and destructive interference as the different length paths go in and out of phase. If there are reflective surfaces along the direct path between the TX and RX, the waves reflecting off those surfaces may arrive either out of phase or in phase with the signals that travel directly

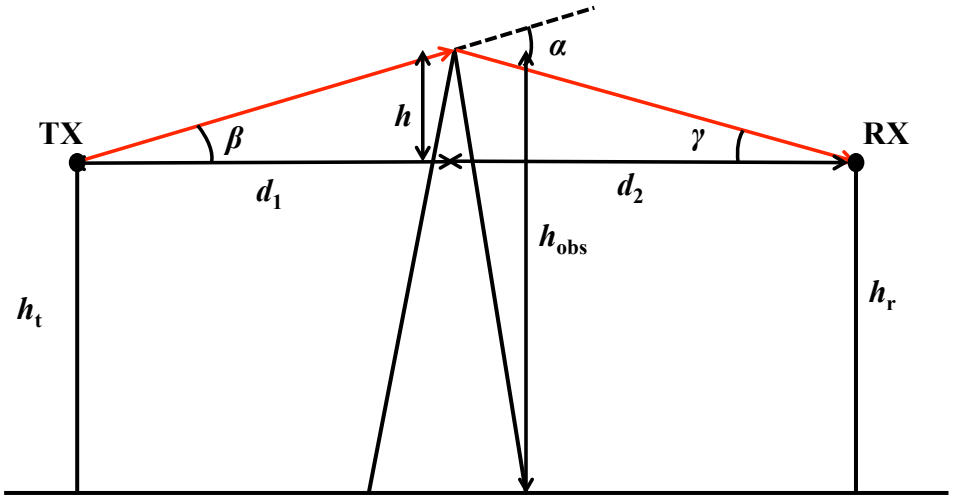

FIGURE 3.1: Knife edge diffraction geometry when the transmitter and receiver are at the same height. The point TX represents the transmitter and RX represents the receiver, with an infinite knife-edge obstruction blocking the line-of-sight path.

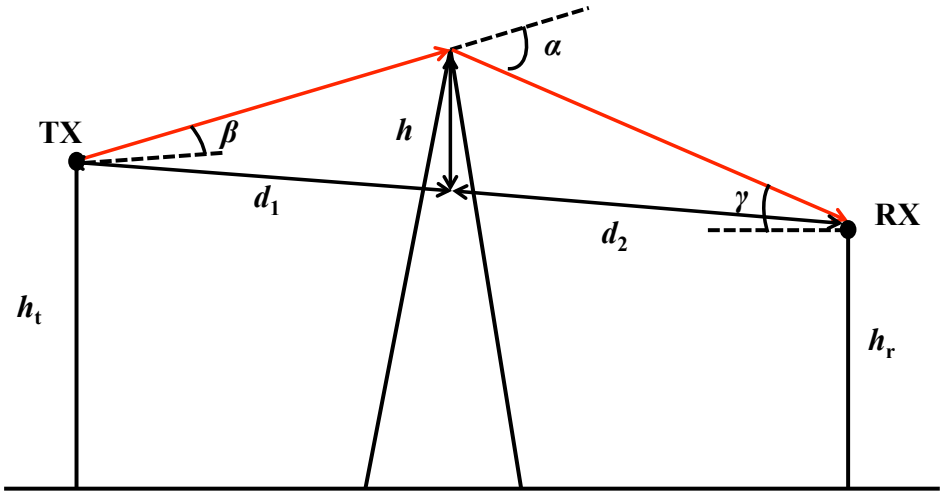

FIGURE 3.2: Knife edge diffraction geometry when the transmitter and receiver are not at the same height. The point TX represents the transmitter and RX represents the receiver, with an infinite knife-edge obstruction blocking the line-of-sight path.

to the RX. Waves that reflect off of surfaces within an even Fresnel zone create signals with phase shifts of 180°, which are out of phase with the direct path wave and reduce the power of the received signal. Waves that reflect off of surfaces within an odd Fresnel zone create signals with phase shifts of 360°, which are in phase with the direct-path wave and can enhance the power of the received signal.

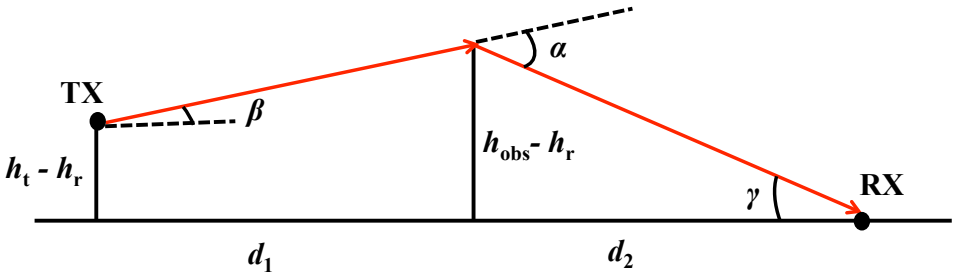

FIGURE 3.3: Equivalent knife edge diffraction geometry where the smallest height (in this case h_r) is subtracted from all other heights. The point TX represents the transmitter and RX represents the receiver, with an infinite knife-edge obstruction blocking the line-of-sight path.

Fig. 3.4 and Fig. 3.5 demonstrate the diagrams of the Fresnel zones. The radius of the nth Fresnel zone circle is expressed by r_n in terms of n, λ, d_1, and d_2

$$r_n = \sqrt{\frac{n\lambda d_1 d_2}{d_1 + d_2}} \tag{3.6}$$

For $d_1, d_2 >> r_n$

Diffraction loss occurs from the obstruction blockage of secondary waves such that a portion of the energy is diffracted and some of the energy reaches the RX, depending on the obstruction geometry. The received energy in the shadow region is the vector sum of the energy from the unobstructed Fresnel zones. In general, if the obstruction does not block energy in the first Fresnel zone, the diffraction loss can be neglected. In microwave mobile communication system design, as long as 55% of the first Fresnel zone is not blocked, the further Fresnel zones do no have significant impact on diffraction loss.

Diffraction loss over complex and irregular obstruction can be difficult to calculate, here we focus on some simple obstructions, which can provide good prediction into the order of magnitude of diffraction loss. Single objects, such as a corner or mountain can be considered as a diffracting knife edge, which is the simplest diffraction model.

The electric field strength E_d at the RX is a vector sum of the the field of all secondary Huygen's source in the plane above the knife edge, which is given by

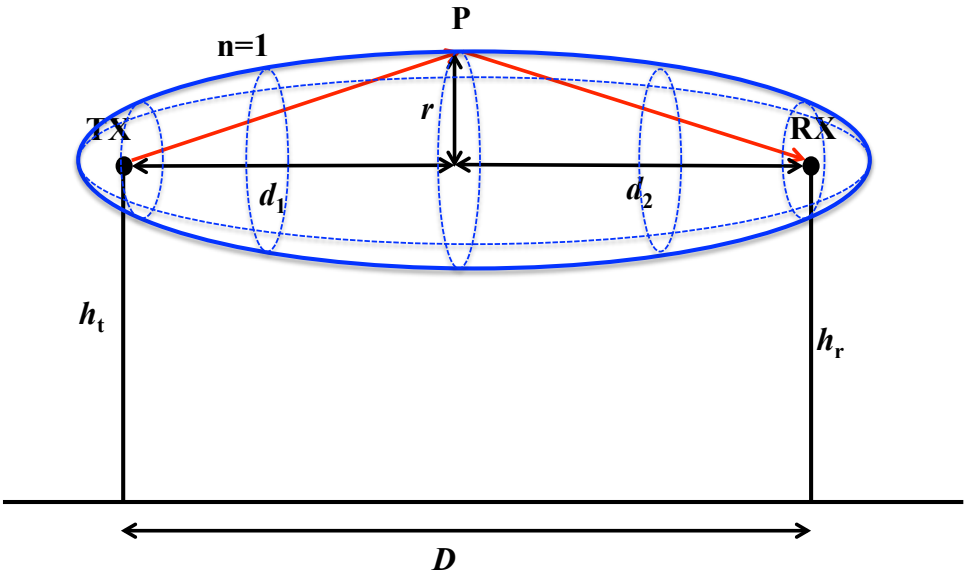

FIGURE 3.4: 3-D geometry of the first Fresnel zone ($n = 1$). D is the distance between the TX and RX, and r is the radius of the first Fresnel zone at point P. P is d_1 away from the TX, and d_2 away from the RX.

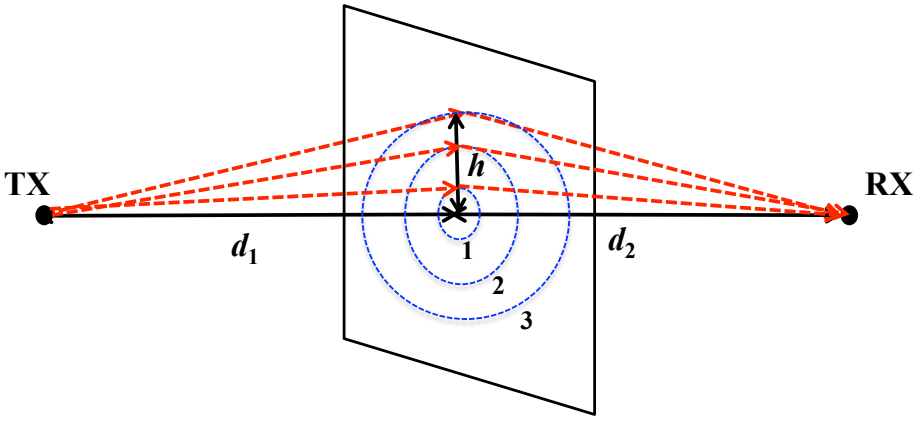

FIGURE 3.5: Concentric circles which define the boundaries of successive Fresnel zones.

$$E_d = E_0 \frac{e^{-jk(d_1+d_2)}}{d_1+d_2} \cdot \frac{1+j}{2} \int_v^\infty e^{-j(\pi/2)t^2} dt \tag{3.7}$$

where the diffraction parameter ν can be written as

$$\nu = h\sqrt{\frac{2(d_1+d_2)}{\lambda d_1 d_2}} = \alpha\sqrt{\frac{2d_1 d_2}{\lambda(d_1+d_2)}} \tag{3.8}$$

under the conditions that d_1, $d_2 >> h$, and d_1, $d_2 >> \lambda$.

Fig. 3.6 is knife edge diffraction simulation result for $d_1 = 2$ m and $d_2 = 1$ m at 10, 20, and 26 GHz. The diffraction loss for all frequencies is approximately 30 - 35 dB as the diffraction angle increases (far away from the corner). Diffraction loss also increases with frequency, due to decrease in wavelength.

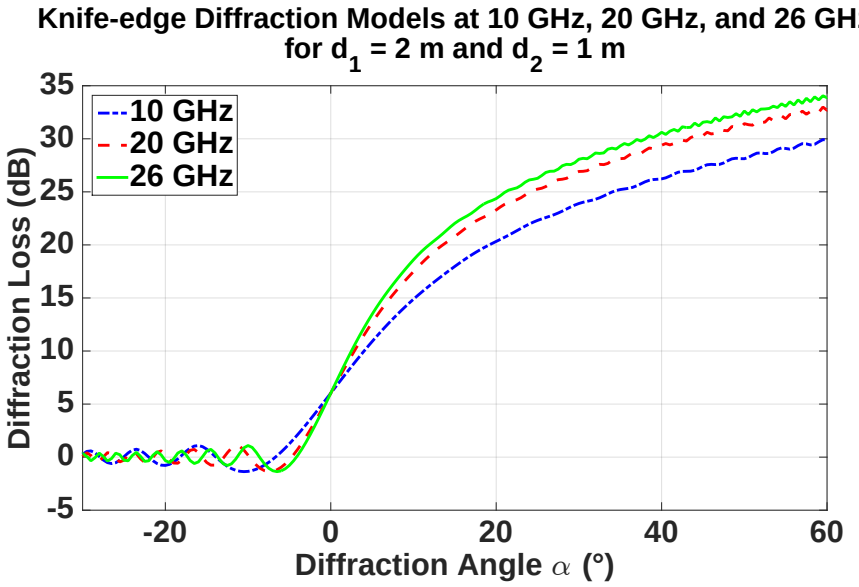

FIGURE 3.6: Knife edge diffraction simulation when the transmitter and receiver are at the same height for $d_1 = 2$ m and $d_2 = 1$ m.

3.2 Geometrical Theory of Diffraction

Fresnel knife edge diffraction model has the advantage of simplicity and accuracy for diffraction loss prediction for many geometries, but in some cases, the results are in serious disagreement with measurements since it neglects the shape and material of the diffracting surface [28, 41–46]. In this section, Geometrical theory of diffraction (GTD) model will be introduced, which significantly improve the accuracy of the prediction.

Fig. 3.7 consider a field point in the shadow region, and the electric field in GTD formulation at the field point is given by:

$$E_{GTD} = E_0 \frac{e^{-jks'}}{s'} D \sqrt{\frac{s'}{s(s'+s)}} e^{-jks} \tag{3.9}$$

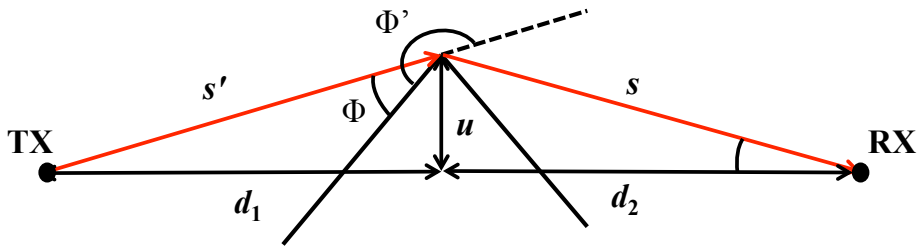

FIGURE 3.7: Geometry and coordinates for application of GTD.

where D represents the diffraction coefficient. The diffraction coefficient depends upon the polarization of the incident field on the edge. Assume the corner edge is perfectly conducting, the diffraction coefficient when polarization of the incident field is parallel to the plane of incidence is given as:

$$D_{\parallel} = \frac{e^{-j(\pi/4)\sin(\pi/n)}}{n\sqrt{2\pi k}} \left[\frac{1}{\cos(\pi/n) - \cos(\frac{\phi-\phi'}{n})} + \frac{1}{\cos(\pi/n) - \cos(\frac{\phi+\phi'}{n})} \right] \tag{3.10}$$

The diffraction coefficient when polarization of the incident field is perpendicular to the plane of incidence is given as:

$$D_{\perp} = \frac{e^{-j(\pi/4)\sin(\pi/n)}}{n\sqrt{2\pi k}} \left[\frac{1}{\cos(\pi/n) - \cos(\frac{\phi-\phi'}{n})} - \frac{1}{\cos(\pi/n) - \cos(\frac{\phi+\phi'}{n})} \right] \tag{3.11}$$

where ϕ' and ϕ are the angles of incidence and diffraction. $n\pi$ is the exterior edge angle. The expression for diffraction coefficient of a perfectly conducting edge is provided as:

$$\begin{aligned} D_{\parallel} = \frac{-e^{-j(\pi/4)}}{2n\sqrt{2\pi k}} \times \Bigg[& \cot(\frac{\pi + (\phi - \phi')}{2n}) \cdot F(kLa^{+}(\phi - \phi')) \\ & + \cot(\frac{\pi - (\phi - \phi')}{2n}) \cdot F(kLa^{-}(\phi - \phi')) \\ & + R_0^{\parallel} \cot(\frac{\pi - (\phi + \phi')}{2n}) \cdot F(kLa^{-}(\phi + \phi')) \\ & + R_n^{\parallel} \cot(\frac{\pi + (\phi + \phi')}{2n}) \cdot F(kLa^{-}(\phi + \phi')) \Bigg] \end{aligned} \tag{3.12}$$

$$
\begin{aligned}
D_{\perp} = \frac{-e^{-j(\pi/4)}}{2n\sqrt{2\pi k}} \times \Bigg[& \cot\left(\frac{\pi + (\phi - \phi')}{2n}\right) \cdot F(kLa^{+}(\phi - \phi')) \\
& + \cot\left(\frac{\pi - (\phi - \phi')}{2n}\right) \cdot F(kLa^{-}(\phi - \phi')) \\
& + R_0^{\perp} \cot\left(\frac{\pi - (\phi + \phi')}{2n}\right) \cdot F(kLa^{-}(\phi + \phi')) \\
& + R_n^{\perp} \cot\left(\frac{\pi + (\phi + \phi')}{2n}\right) \cdot F(kLa^{-}(\phi + \phi')) \Bigg]
\end{aligned}
\tag{3.13}
$$

where the Fresnel integral is calculated as:

$$
F(x) = 2j\sqrt{x}e^{jx} \int_{\sqrt{x}}^{\infty} e^{-jt^2} dt \tag{3.14}
$$

$$
a^{+}(\beta) = 2\cos^2\left(\frac{2n\pi N^{+} - \beta}{2}\right) \qquad \text{and} \qquad \beta = \pi + \pi'
$$

$$
a^{-}(\beta) = 2\cos^2\left(\frac{2n\pi N^{-} - \beta}{2}\right) \qquad \text{and} \qquad \beta = \pi - \pi'
$$

in which N^{+} and N^{-} are the integers which most nearly satisfy the equations:

$$
2\pi n N^{+} - (\beta) = \pi \tag{3.15}
$$

$$
2\pi n N^{-} - (\beta) = -\pi \tag{3.16}
$$

with

$$
\beta = \phi \pm \phi' \tag{3.17}
$$

L is a distance parameter, which is defined for several types of illumination.

$$L = \frac{ss'}{s+s'} \tag{3.18}$$

for cylindrical-wave incidence.

$$L = s \tag{3.19}$$

for plane-wave incidence.

3.2.1 Diffraction From an Absorbing Screen

A rigorous study of diffraction by wedges having absorbing faces has been carried out by Felsen [47]. For a plane wave with an incident angle of ϕ', the results of the rigorous approach give the GTD diffraction coefficient as:

$$D = \frac{-1}{\sqrt{2\pi k}}\left[\frac{1}{\pi - |\phi - \phi'|} + \frac{1}{\pi + |\phi - \phi'|}\right] = \frac{-1}{\sqrt{2\pi k}}\left[\frac{1}{\theta} + \frac{1}{2\pi + \theta}\right] \tag{3.20}$$

where ϕ is angle of the diffracted wave, and θ is the diffraction angle, which is defined as $\theta = \pi - (\phi - \phi')$. All the angle values are in radians. The diffraction coefficient is independent of the incident angle ϕ'.

3.2.2 Diffraction From a Conducting Screen

A plane wave incident on a thin conductor screen will be reflected, so that the diffraction coefficient must be singular at the incident wave shadow boundary. The GTD diffraction coefficient is given as [47, 48]:

$$D = \frac{-1}{2\sqrt{2\pi k}}\left[\frac{1}{\cos\frac{\phi-\phi'}{2}} + \frac{\Gamma_E}{\cos\frac{\phi+\phi'}{2}}\right] \tag{3.21}$$

where $\Gamma_E = 1$ is used for the polarization of the incident wave parallel to the edge. The first term inside the bracket is singular at the shadow boundary of the incident wave where $\phi = \phi' + \pi$, and the second term inside the bracket is singular at the shadow boundary of the reflected wave where $\phi = \pi - \phi'$.

3.2.3 Diffraction From a Right-Angle Wedge

The GTD diffraction coefficient for a right angle conducting wedge is found to be [48]:

$$D = D_1 + D_2 + \Gamma_E(D_3 + D_4) \tag{3.22}$$

$$D_{1,2} = \frac{-1}{3\sqrt{2\pi k}} \cot \frac{\pi \pm (\phi - \phi')}{3} \tag{3.23}$$

$$D_{3,4} = \frac{-1}{3\sqrt{2\pi k}} \cot \frac{\pi \pm (\phi + \phi')}{3} \tag{3.24}$$

where $\Gamma_E = 1$ is used for the polarization of the incident wave parallel to the edge. The first two terms inside the bracket are singular along the shadow boundary of the incident wave where $\phi = \phi' + \pi$, and the other two terms inside the bracket are singular along the shadow boundary of the reflected wave where $\phi = \pi - \phi'$. The UTD diffraction coefficient is given by multiplying each term in the above equation with a transition function [48].

The magnitude of diffraction loss calculated using the diffraction coefficients from the three equations (3.20) (3.21) (3.22) are plotted in Fig. 3.8, 3.9, 3.10, 3.11, 3.12, and 3.13 at 10, 20, and 26 GHz. The diffraction losses calculated from these models are compared with the KED model at the same frequency. The wave number k in these models is calculated $k = \frac{2\pi f\sqrt{\epsilon_r}}{c}$, where ϵ_r is the relative dielectric constant. In the simulation, two values of the relative dielectric constant are used, which are $\epsilon_r = 5$

and $\epsilon_r = 10$ [49, 50]. Fig. 3.8 and 3.9 show the magnitude of diffraction loss for the KED model, absorbing screen model, conducting screen model, and right angle wedge model at 10 GHz for relative dielectric constant $\epsilon_r = 5, 10$, respectively. Fig. 3.10 and 3.11 show the magnitude of diffraction loss for four different models at 20 GHz for relative dielectric constant $\epsilon_r = 5, 10$, respectively. Fig. 3.12 and 3.13 show the magnitude of diffraction loss for four different models at 26 GHz for relative dielectric constant $\epsilon_r = 5, 10$, respectively. All the simulation results are converted and expressed in degree, not in radians.

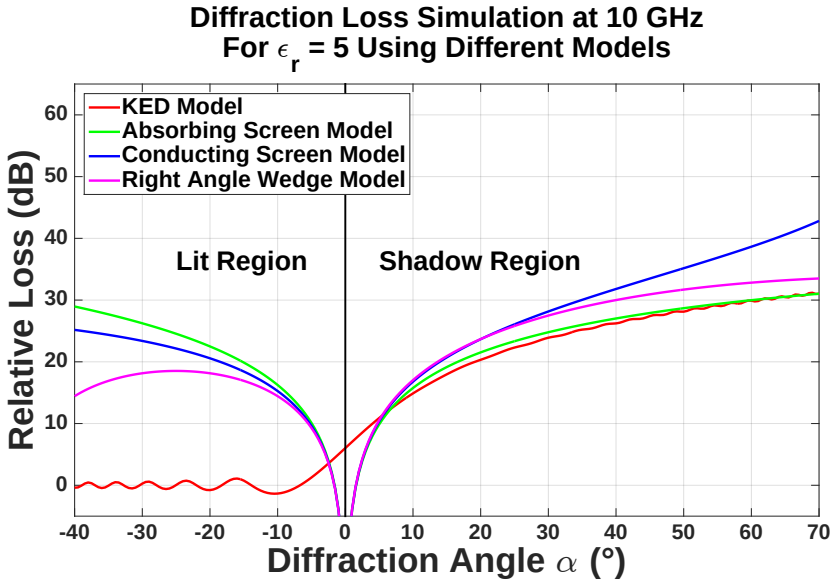

FIGURE 3.8: Diffraction loss simulation at 10 GHz $\epsilon_r = 5$ using the KED model, absorbing screen model, conducting screen model, and right angle wedge model based on GTD.

3.2.4 Diffraction From A Convex Surface

The KED model is one of the most commonly used methods of prediction but can only be used for sharp knife edges, and does not account for the radius of curvature of an obstacle. Many natural terrain features and building features exhibit curved surfaces, indicating that the radius of curvature should be accounted for.

A creeping wave is the wave that is diffracted around the surface of a rounded obstacle such as a circular cylinder, as shown in Fig. 3.14. The asymptotic representation for

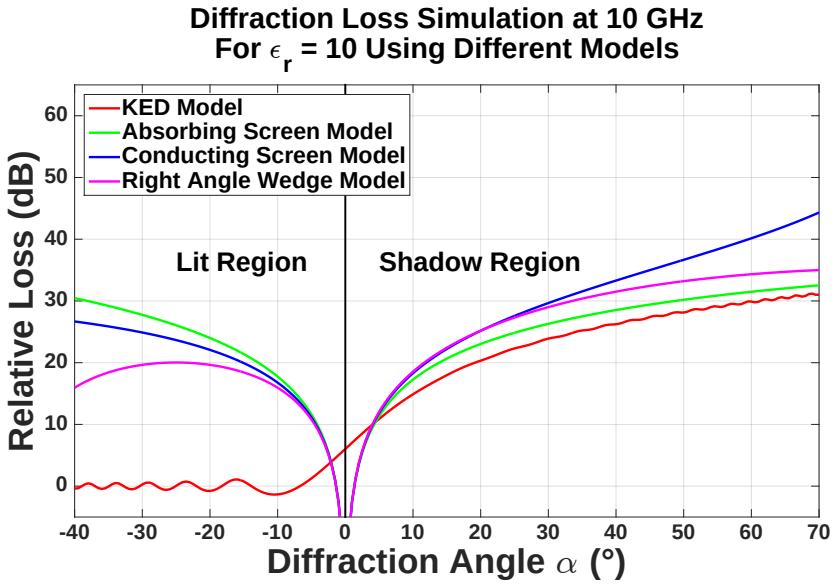

FIGURE 3.9: Diffraction loss simulation at 10 GHz $\epsilon_r = 10$ using the KED model, absorbing screen model, conducting screen model, and right angle wedge model based on GTD.

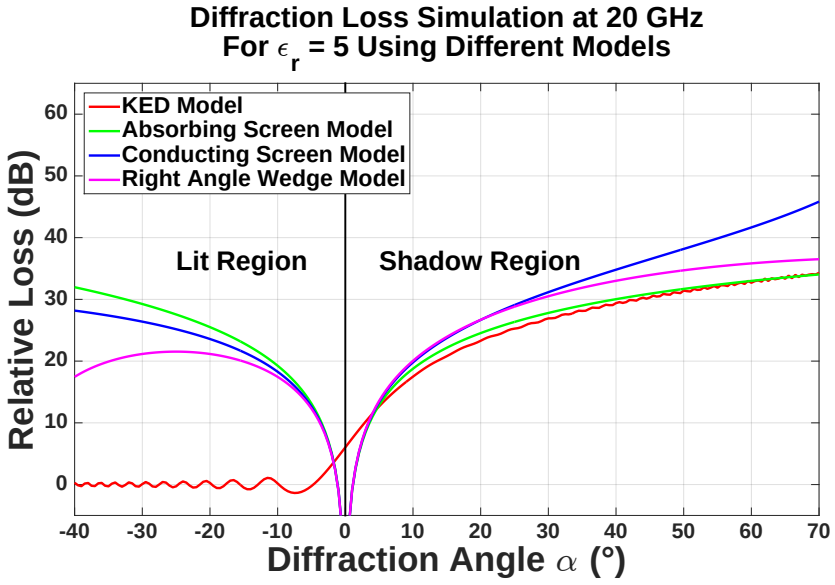

FIGURE 3.10: Diffraction loss simulation at 20 GHz $\epsilon_r = 5$ using the KED model, absorbing screen model, conducting screen model, and right angle wedge model based on GTD.

the creeping ray field [12, 51–53] at the RX antenna behind the cylinder for an incident plane wave is proportional to:

$$E \sim E_i e^{-jk\alpha R_h} \frac{e^{-jkd_2}}{\sqrt{kd_2}} \sum_{p=1}^{\infty} D_p R_h \cdot \exp(-\psi_p \alpha) \tag{3.25}$$

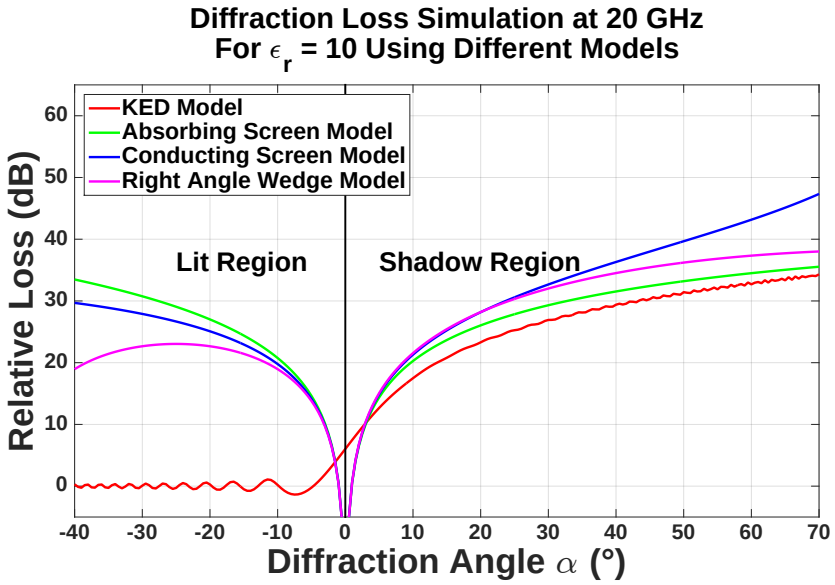

FIGURE 3.11: Diffraction loss simulation at 20 GHz $\epsilon_r = 10$ using the KED model, absorbing screen model, conducting screen model, and right angle wedge model based on GTD.

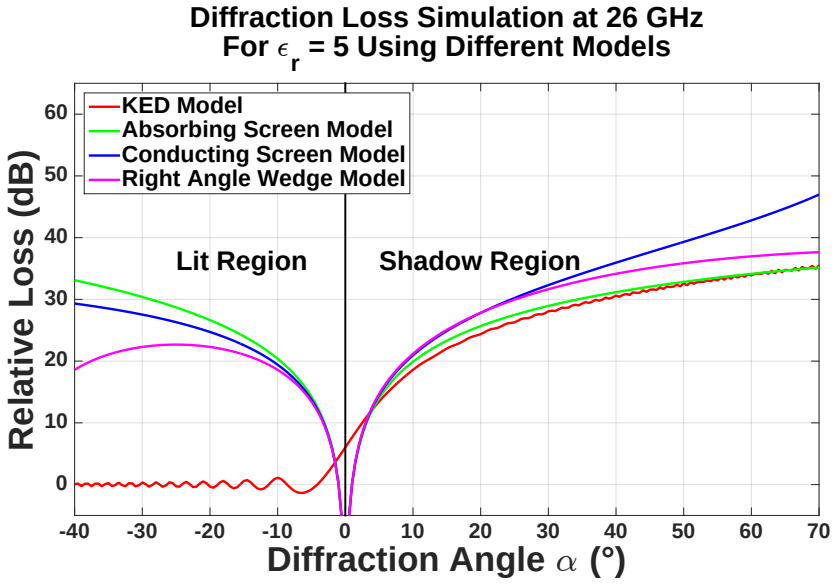

FIGURE 3.12: Diffraction loss simulation at 26 GHz $\epsilon_r = 5$ using the KED model, absorbing screen model, conducting screen model, and right angle wedge model based on GTD.

where E_i is the incident field at the TX, d_2 is the distance from the launch point to the RX antenna, k is the wave number, and α is the diffraction angle. D_p is excitation coefficient and ψ_p is the attenuation constance, which are functions of cylinder radius and frequency:

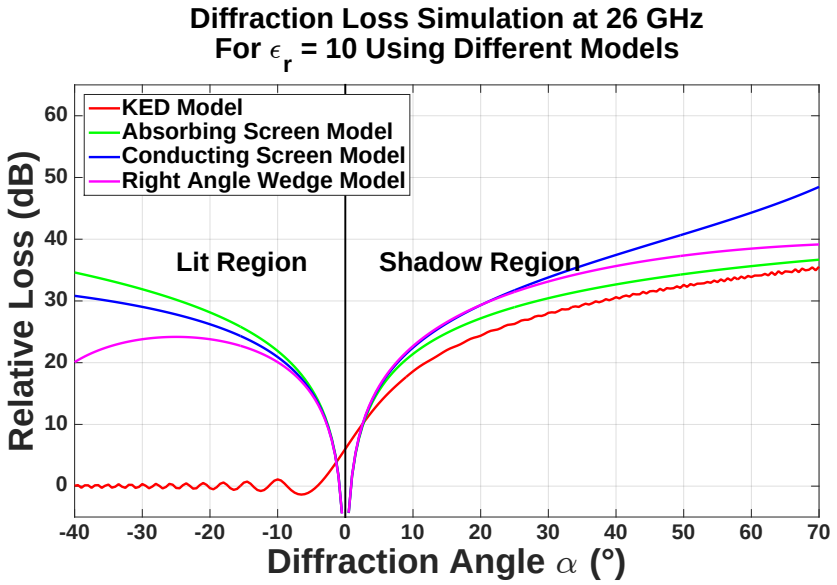

FIGURE 3.13: Diffraction loss simulation at 26 GHz $\epsilon_r = 10$ using the KED model, absorbing screen model, conducting screen model, and right angle wedge model based on GTD.

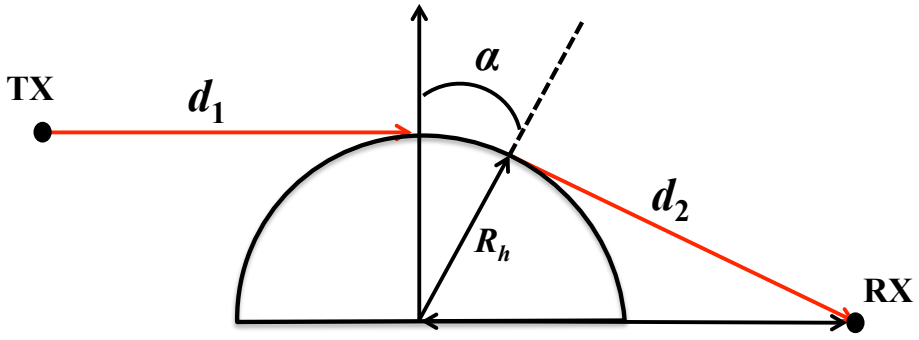

FIGURE 3.14: Diffraction by a circular cylinder

$$D_p, \psi_p \sim \left(\frac{kP_h}{2}\right)^{\frac{1}{3}} \tag{3.26}$$

The mathematical derivation of the asymptotic representation for the creeping ray can be found in [54]. A reasonable approximation can be obtained by keeping only the $p = 1$ term in (3.25). The representation of the creeping ray field is proportional to:

$$E \sim D_p R_h \cdot \exp(-\psi_p \alpha) \tag{3.27}$$

The diffraction gain/loss in dB due to the presence of an obstacle, as compared to the free space signal, can be calculated as

$$G(\alpha)[\text{dB}] = -P(\alpha) = 20\log_{10} E = -A(R_h, f)\psi_p\alpha + C(R_h, f) \tag{3.28}$$

where $A(R_h, f)$ and $C(R_h, f)$ are functions of the radius of the object and frequency, which are computationally extensive. According to (3.28), a creeping wave model [17] can estimate diffraction loss from a curved surface at one frequency.

$$P(\alpha) = n \cdot \alpha + c \tag{3.29}$$

n is the slope value of the creeping wave model, which can be obtained from measurement data using minimum mean square error (MMSE) estimation. c is the anchor point of the creeping wave model, which is determined to be 6.03 dB, corresponding to the diffraction loss predicted by the KED model at the 0° diffraction angle.

3.2.5 Statistics Between Measurements And Prediction

The agreement between the measurement and theoretical prediction can be evaluated in terms of two parameters: mean error (ME) and standard deviation (SD) [55]. The error (in dB) between the measurement and the theoretical prediction for each diffraction angle (α) is defined as,

$$\Delta(\alpha_i)[\text{dB}] = P_{meas}(\alpha_i) - P_{pred}(\alpha_i) \tag{3.30}$$

The ME is an indicator for the overall trend of the prediction and zero value of ME indicates that the estimation matches well to the measurement, which is defined as,

$$\mathrm{ME[dB]} = \frac{1}{N}\sum_{i=1}^{N}\Delta(\alpha_i) \tag{3.31}$$

where N is the total number of diffraction angles measured in the shadow region.

The SD is computed as,

$$\mathrm{SD[dB]} = \left[\frac{1}{N-1}\sum_{i=1}^{N}\left(\Delta(\alpha_i) - \mathrm{ME}\right)^2\right]^{\frac{1}{2}} \tag{3.32}$$

where $N-1$ is used for sample standard deviation calculation [55].

Chapter 4

Measurement Environments and Procedures

4.1 Measurement Overview

Diffraction is a natural phenomenon that occurs when a wave encounters an obstacle or obstruction, and is often described as the bending of a wave around an obstacle or obstruction. The measurements proposed in this document are designed to gain insight into the phenomenon of diffraction around corners, pillars, and irregular objects in both outdoor and/or indoor environments. The measurements were performed at 10, 20, and 26 GHz using a continuous wave (CW) channel sounder with directional horn antennas at the transmitter (TX) and receiver (RX). The TX and RX antennas were located 1.4 m above ground level, for V-V (vertical-vertical) and H-V (horizontal-vertical) TX-RX antenna polarization combinations.

4.2 Measurement Hardware

The measurements were performed by transmitting an unmodulated CW tone at 10, 20, and 26 GHz generated by an Agilent E8257D analog signal generator. The signal were fed directly into a waveguide adapter that was attached to a directional horn antenna (the TX set up is shown in Fig. 4.5). Fig. 4.1 shows a block diagram of the general TX and RX systems to be used for the diffraction measurements. The TX and RX made use of identical directional horn antennas. The flange type, antenna gain, and half-power-beamwidth (HPBW) for measurements at each frequency are provided in in Table 4.1. The size of these antennas are shown in Fig. 4.2. The far field distances of these antennas are 0.47, 0,46, and 0.83 m at 10, 20 and 26 GHz, respectively. The received signal at the RX antenna was measured by an Agilent E4407B spectrum analyzer. The TX and RX antennas were held by waveguide standoffs (shown in Fig. 4.3) that were mounted on rotatable gimbals. The standoffs held the antennas for either vertical or horizontal polarization orientations. The gimbal allowed the antenna pointing angle to be adjusted in the azimuth and elevation planes and fixed in specific angular directions for each measurement procedure described below. The TX antenna was mounted on a tripod, and the RX antenna on top of the gimbal was mounted on a 35.3 cm long linear track (shown in Fig. 4.4). The linear track has a resolution less than 0.01 mm, and the antenna position can be precisely controlled by a computer with LabVIEW software. The RX set up is shown in Fig. 4.6 and Fig. 4.7).

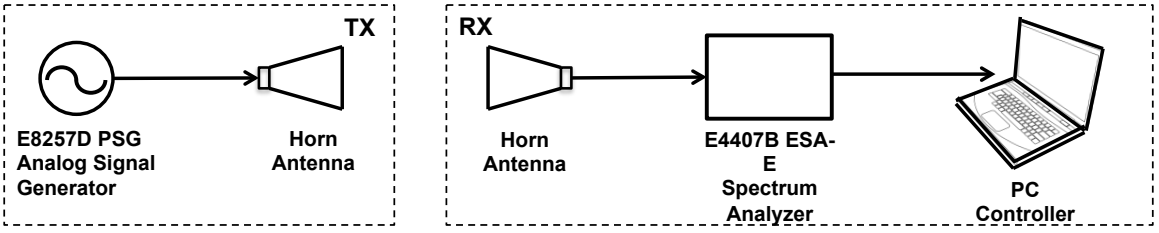

FIGURE 4.1: Block diagrams for the 10, 20, and 26 GHz measurements. The TX and RX antennas are different for each frequency measured, but each have the same gain and similar HPBW.

TABLE 4.1: Antenna Parameters, including flange type, antenna gain, and half-power beam width (HPBW) used for 10, 20, and 26 GHz measurements.

Measured Frequency	Flange Type	Antenna Gain	HPBW
10 GHz	**WR-75**	**20 dBi**	**17°**
20 GHz	**WR-51**	**20 dBi**	**17°**
26 GHz	**WR-28**	**24.5 dBi**	**10.9°**

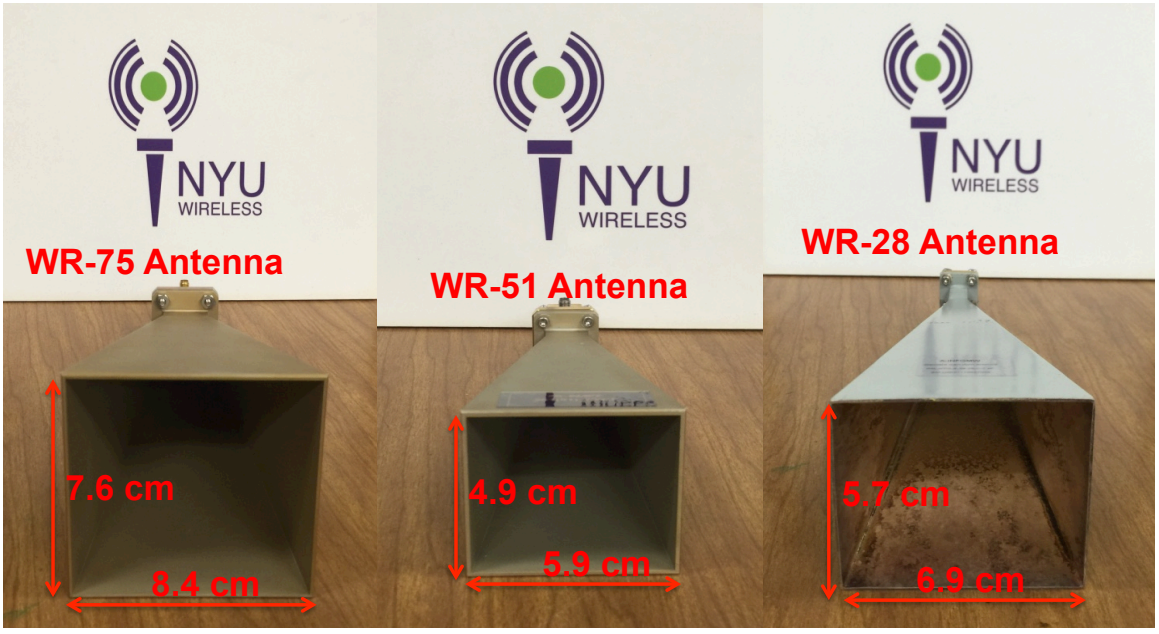

FIGURE 4.2: The horn antennas used in the diffraction measurements. WR-75 flange type is used for 10 GHz measurement, WR-51 flange type is used for 20 GHz measurement, and WR-28 flange type is used for 26 GHz measurement.

4.3 Measurement Locations

4.3.1 Indoor Measurements

4.3.1.1 Corner Measurements

Indoor corner measurements were performed at two 90° right-angle corners made of drywall and wood in the NYU WIRELESS research center on the 9th floor of 2 MetroTech Center as shown in Fig. 4.8 and Fig. 4.9. The TX antenna was located on one side of

FIGURE 4.3: Waveguide standoffs used to secure the TX and RX antennas.

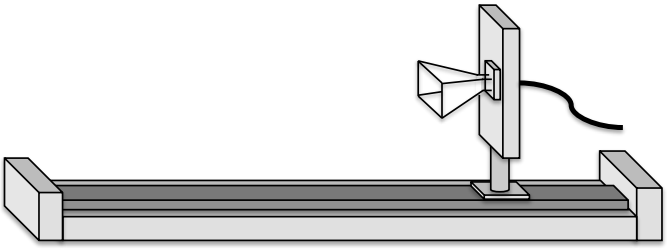

FIGURE 4.4: Schematic diagram of the RX linear track.

FIGURE 4.5: Measurement Set up at the TX side.

the corner, while the RX moved along a simulated arc using a linear track placed on the other side of the corner.

FIGURE 4.6: Measurement Set up at the RX side.

4.3.1.2 Irregular Object Measurements

Indoor irregular object measurements were performed at a plastic board with a thickness of 2 cm outside NYU classrooms on the 9^{th} floor of 2 MetroTech Center as shown in Fig. 4.10. The TX antenna was located on one side of the board, while the RX moved along a simulated arc using a linear track placed on the other side of the board.

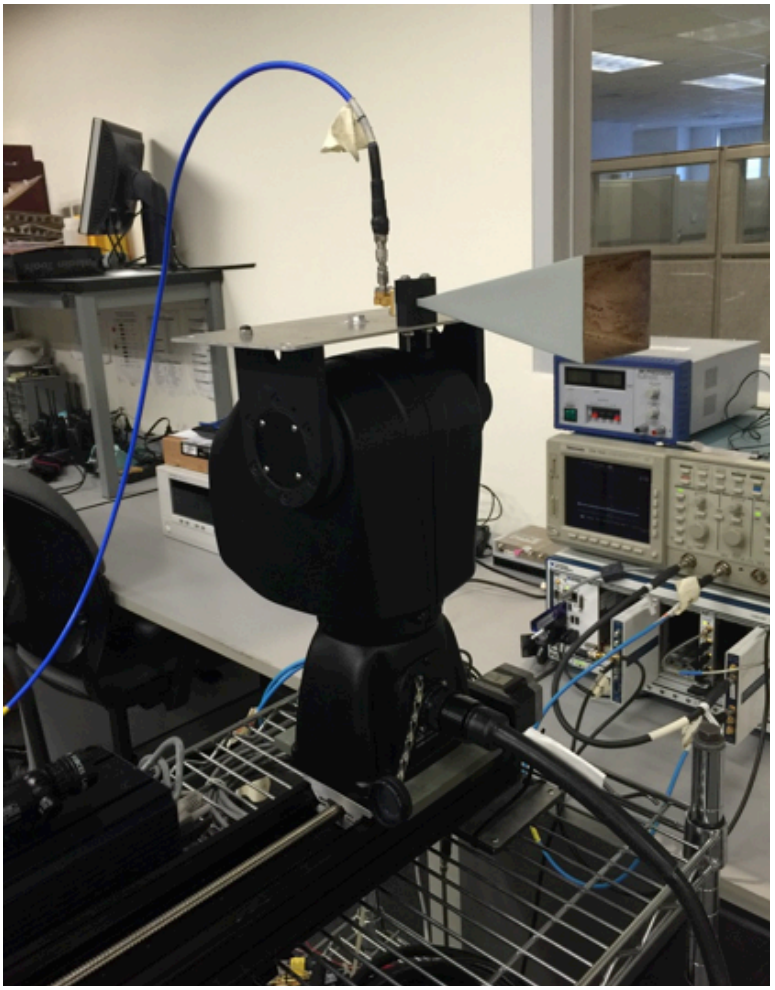

FIGURE 4.7: Measurement Set up at the RX side.

4.3.2 Outdoor Measurements

4.3.2.1 Corner Measurements

The outdoor building corner measurements were performed at a 90° right-angle corner made of marble in NYU Brooklyn campus. Fig. 4.12 shows the outdoor corner measurement location, and Fig. 4.13 shows the simulated measurement setup at the corner using Google Sketch Up. The TX antenna was located on one side of the corner (along the sidewalk), while the RX antenna moved along the linear track on the other side of the corner (on an open area).

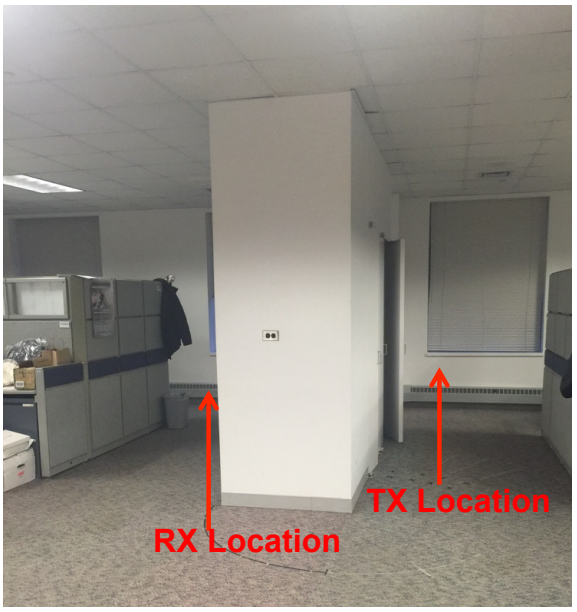

FIGURE 4.8: TX and RX locations for indoor corner measurements in the NYU WIRELESS research center on the 9th floor of 2 MetroTech Center. The material of the corner is drywall.

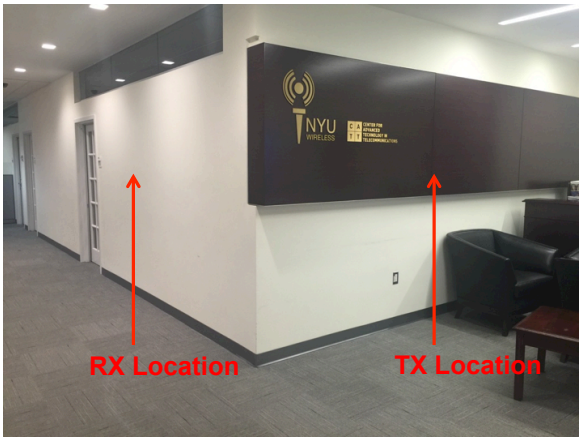

FIGURE 4.9: TX and RX locations for indoor corner measurements in the NYU WIRELESS research center on the 9th floor of 2 MetroTech Center. The material of the corner is wood.

4.3.2.2 Irregular Object Measurements

The irregular object measurements were performed at a stone pillar outside of the Dibner Building as shown in Fig. 4.14. For the irregular object measurements, the TX antenna was located on one side of the object, while the RX moved along the linear track on the other side of the object. At the beginning of the measurements, the TX and RX antennas were always pointed toward a common edge of the object. Fig. 4.15 shows

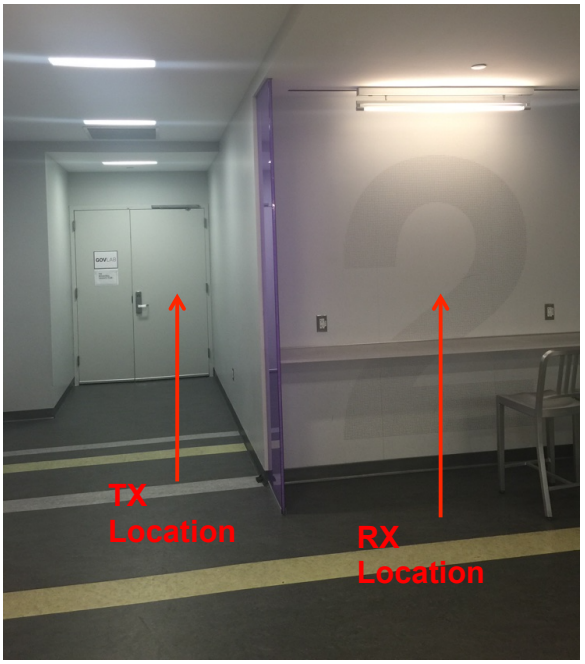

FIGURE 4.10: TX and RX locations for indoor irregular object measurements outside NYU classrooms on the 9th floor of 2 MetroTech Center. The material of the irregular object is plastic.

measurements at the stone pillar and marble corner. Fig. 4.16 demonstrates a close look at the five tested materials, including drywall, wood, plastic, marble and stone.

4.4 Measurement Procedures

4.4.1 Indoor Measurements

The indoor measurements were performed at 10, 20, and 26 GHz for V-V and H-V antenna polarization configurations with the TX and RX antennas set at heights of 1.4 m above the ground. The TX antenna was located on one side of a corner, and the RX antenna located on the other side of the corner was mounted on a rotating gimbal, which moved along a linear track. The distance from the TX antenna to the edge of the diffracted corner was in the far field of the antenna and the diffraction object and was constant at 2 m (d_1), and the distance from the edge of the corner to the RX antenna was in the far field constant at 1 m (d_2) as shown in Fig. 4.17 (for the 26 GHz

FIGURE 4.11: TX and RX locations for indoor measurements outside NYU classrooms on the 9^{th} floor of 2 MetroTech Center. Test materials include: drywall, plastic, and wood.

FIGURE 4.12: TX and RX locations for the outdoor marble corner measurements in NYU Brooklyn campus.

antenna, the far field distance is 1.38 m, a little bit larger than d_2). The TX antenna was adjusted to point to the edge of the corner for three fixed incident angles (β), from

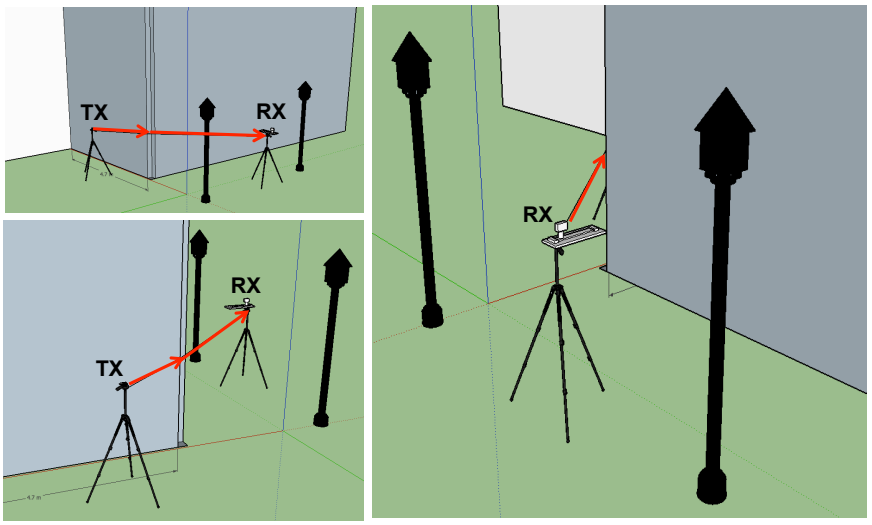

FIGURE 4.13: Simulated building corner measurement setup using Google SketchUp.

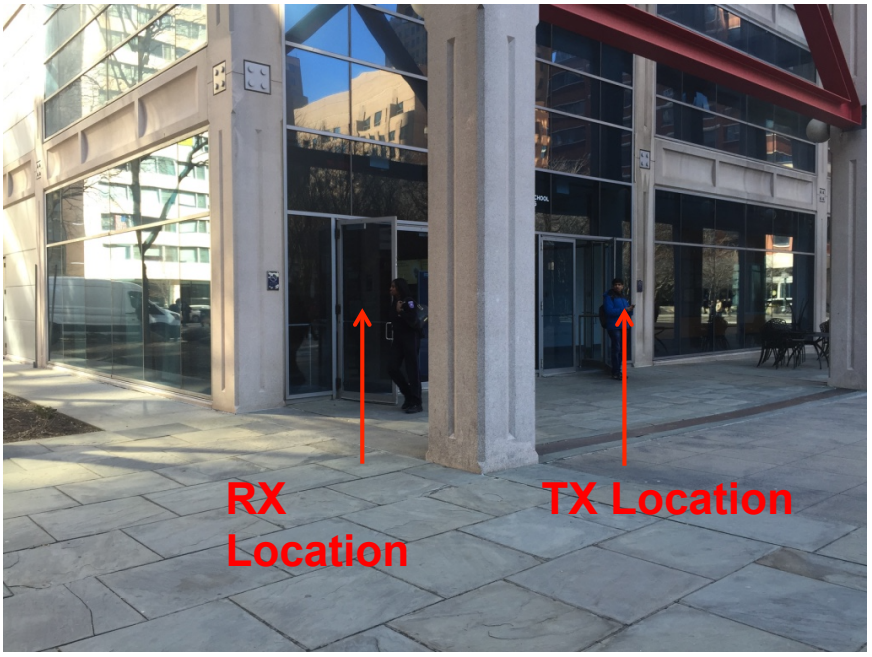

FIGURE 4.14: Pillar measurement location outside of the Dibner Building.

approximately 10° to 35°. The RX antenna moved along the track in step increments of 0.875 cm, which corresponds to approximately 0.5° increments of the diffraction angle (α). The RX antenna was adjusted to point to the edge of the corner at each track increment, with the RX power level measured by an Agilent E4407B spectrum analyzer. For each track location, the 35.5 cm long linear track was used to measure a 20° swath of diffraction angles in the horizontal plane (parallel to the ground). Five consecutive

FIGURE 4.15: TX and RX locations for outdoor diffraction measurements on the NYU campus. The test materials include stone and marble.

RX linear track locations were used to simulate a contiguous arc around the corner to measure a 100° swath of total diffraction angles, which enabled the RX antenna to move from the deep shadow region to the lit region. There were five consecutive RX linear track locations formed in an arc, as shown in Fig. 4.20. The corresponding diffraction angles for different incident angles can be found in Fig. 4.18 and Table 4.2. A free space calibration was performed at each measured frequency at a TX-RX separation distance of 3 m (d_1+d_2 = 3 m). The relative diffraction loss was obtained by computing the difference between the calibration received power and the measured power level at each diffraction angle measurement.

FIGURE 4.16: The measured materials include drywall, wood, plastic, marble and stone.

- Measurement Preparation

  1. Calculate a track and angle plan based on the TX and RX track location, and write a LabView program to control the movement of the track and the orientation of the gimbal at the RX side.

  2. Place tape markers on the ground for three TX locations (TX1, TX2, TX3), which correspond to three incident angles β (ranging from 10° to 40°) (refer to Fig. 4.18). The TX locations are chosen to ensure that the distance from the TX antenna to the edge of the diffracted corner is constant at $d_1 = 2$ m.

  3. Place tape markers on the ground for six RX linear track locations (refer to Fig. 4.18). The track locations were the same for different TX locations. Since the total length of the track is 35.3 cm and d_2 is constant at 1 m, the corresponding angle from one end to the other end of the track is 20° (refer to Fig. 4.19). Note that the orientation of the linear track is perpendicular

to the line drawn from the corner to the center of the track. During the measurements, the RX track is initially located at the first track location and subsequently moves to the other track locations for a total of 5 track locations. The RX antenna moves along the track in steps of 0.875 cm, which corresponds to a diffraction angle of approximately 0.5°. The movement of the track and RX antenna forms an artificial arc route (refer to Fig. 4.20).

4. Measure the height of RX antenna, and adjust the height to be 1.4 m above the ground level. Adjust the height of the TX tripod to ensure the height of the TX antenna is identical to the RX antenna height (1.4 m).

- Measurement Procedures

1. Indoor diffraction measurements start with a free space calibration at a TX-RX separation distance of 3 m (d_1+d_2 = 3 m). The power level at 3 m is used as a reference power level to calculate diffraction loss. Note that when changing frequencies, a new calibration at that frequency is needed, although individual frequencies are measured one at a time.
2. Set up the TX side, the TX antenna is placed at the first TX location (TX1) for incident angle of 10°. Use laser pointer to make sure that the TX antenna is pointed to the edge of the corner.
3. Set up the RX side, the RX track is placed at the first RX track location. The RX antenna mounted on one side of the track is first be pointed to the edge of the corner in the line-of-sight (LOS) environment. Fix the laser pen on top of the RX antenna to make sure that the RX antenna is always be pointed to the edge of the corner while the RX antenna is moved from one side of the track to the other.
4. Measure the power level at the first RX antenna location (M1).
5. Move the RX antenna along the track in step increments of 0.875 cm, corresponding to approximately 0.5 ° diffraction angle increments. Each RX antenna increment corresponds to one measurement (M). For the first track

location, the diffraction angle changes from 0° to 20°, corresponding to M1 to M20. The RX antenna moves from a LOS environment to non-LOS (NLOS) environment (shadow region). The computer adjusts the RX antenna pointing angle for every RX antenna movement and record the measured power level from the spectrum analyzer at each track increment.

6. Move the RX track to the next track location, and move the RX antenna to the starting point on the track. Repeat the same procedures (Step 3 - 5) for each RX track location set.

7. Move the TX antenna to the next TX location, and repeat the same procedures (Step 2 - 6) for the following TX locations (TX2 and TX3) as done for TX1.

8. Change the TX antenna polarization from vertical to horizontal. Repeat the same procedures (Step 2 - 7) for H-V polarization combination as those for V-V combination.

TABLE 4.2: Indoor measurement procedures parameters.

Measurement No.	**Frequency (GHz)**	**Polarization**	d_1 **(m)**	d_2 **(m)**	β **(°)**	α **(°)**
1	10; 20; 26	**V-V**	2	1	10	-20 to 80
2	10; 20; 26	**V-V**	2	1	20	-30 to 70
3	10; 20; 26	**V-V**	2	1	30	-40 to 60
4	10; 20; 26	**H-V**	2	1	10	-20 to 80
5	10; 20; 26	**H-V**	2	1	20	-30 to 70
6	10; 20; 26	**H-V**	2	1	30	-40 to 60

4.4.2 Outdoor Measurements

The outdoor measurements were performed at 10, 20, and 26 GHz for V-V and H-V antenna polarization configurations with the TX and RX antennas set at heights of 1.4 m above the ground. The TX antenna was located on one side of a corner, and the

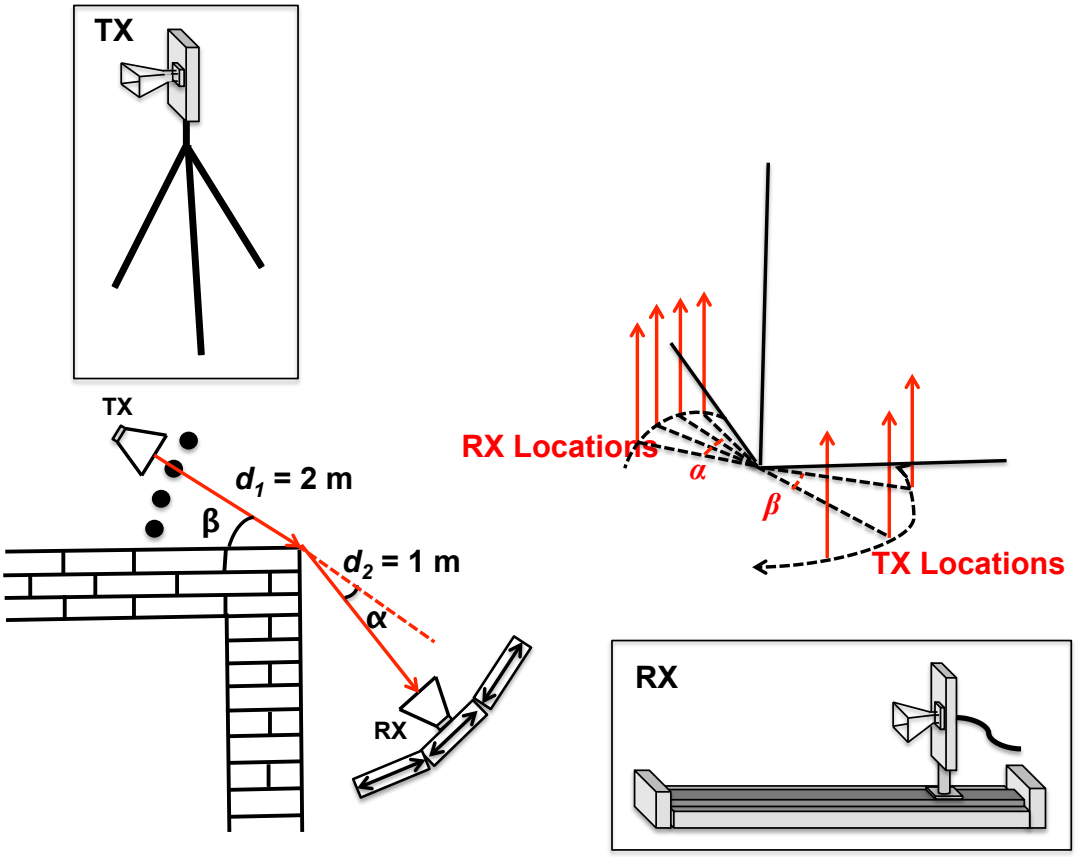

FIGURE 4.17: TX and RX locations for indoor corner measurements in the NYU WIRELESS research center on the 9th floor of 2 MetroTech Center. The distance from the TX antenna to the edge of the diffracted corner is constant at $d_1 = 2$ m, and the distance from the edge of the corner to the RX antenna is constant at $d_2 = 1$ m.

RX antenna located on the other side of the corner was mounted on a rotating gimbal, which moved along a linear track. The distance from the TX antenna to the edge of the diffracted corner was in the far field of the antenna and the diffraction object and was constant at 2 m (d_1), and the distance from the edge of the corner to the RX antenna was in the far field constant at 1 m (d_2) as shown in Fig. 4.17 (for the 26 GHz antenna, the far field distance is 1.38 m, a little bit larger than d_2). The TX antenna was adjusted to point to the edge of the corner for two fixed incident angles (β), from approximately 10° to 35°. The RX antenna moved along the track in step increments of 0.875 cm, which corresponds to approximately 0.5° increments of the diffraction angle (α). The RX antenna was adjusted to point to the edge of the corner at each track increment, with the RX power level measured by an Agilent E4407B spectrum analyzer. For each track

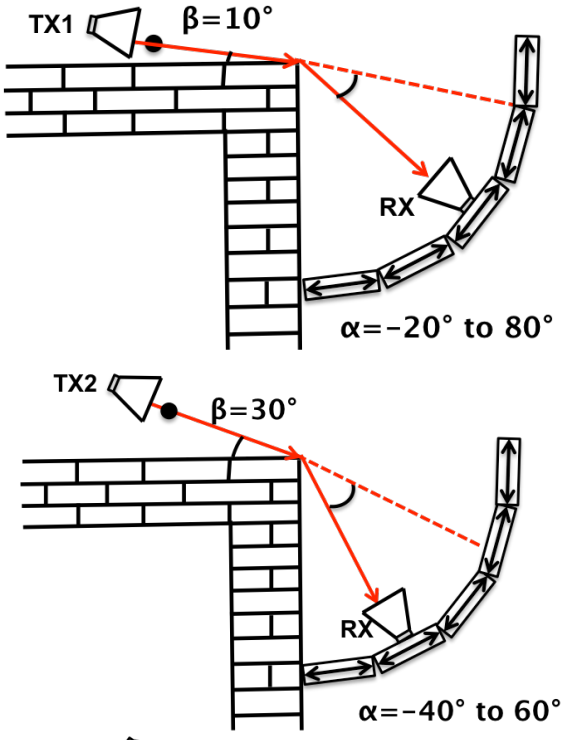

FIGURE 4.18: Two examples of TX locations and their corresponding RX track locations for indoor corner measurements. The TX antenna is point to the edge of the corner with different incident angles (β) from 10° to 40° (incident angles are different for different frequencies). If the incident angle for TX1 is $\beta = 10°$, and the diffraction angle α is ranging from -20° to 80°. If the incident angle for TX2 is $\beta = 30°$, and the diffraction angle α is ranging from -40° to 60°.

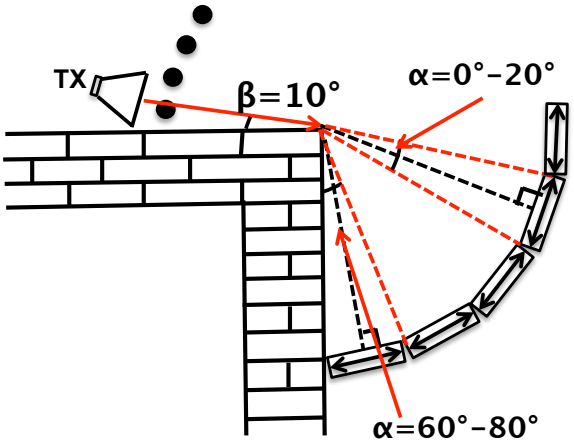

FIGURE 4.19: The RX track locations and corresponding diffraction angles. The track locations remain the same for different TX locations. The total length of the track is 35.3 cm and d_2 is 1 m, thus the corresponding diffraction angle from one end to the other end of the track is 20°. Note that the orientation of the linear track need to be perpendicular to the line drawn from the corner to the center of the track.

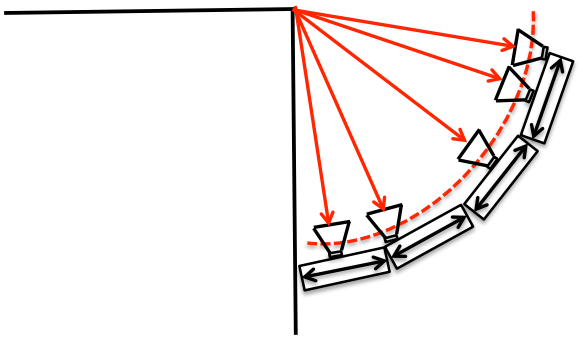

FIGURE 4.20: RX antenna moves from one side to the other side of the linear track, and the track moves from the first track location to the last track location. The entire sets of track locations form an arc route.

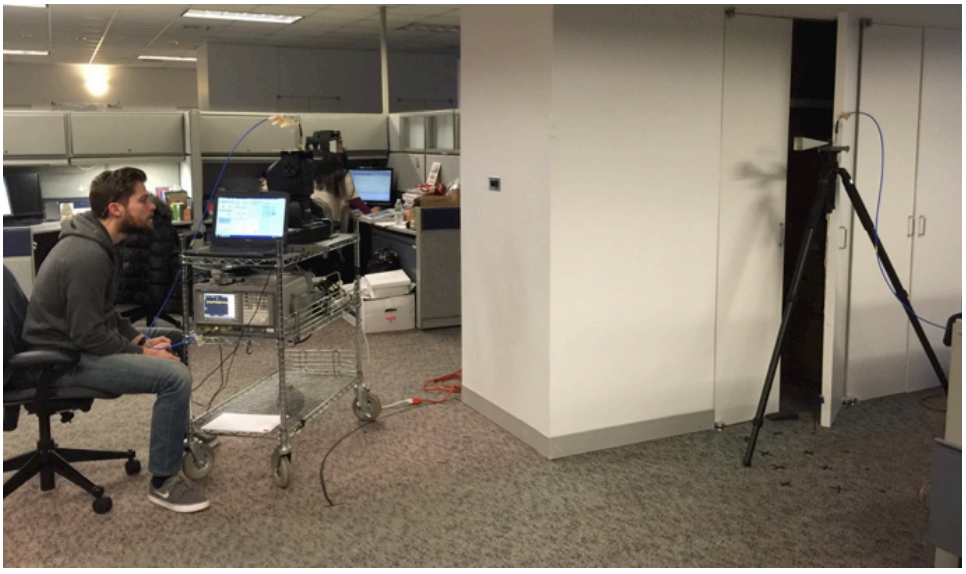

FIGURE 4.21: Indoor drywall corner diffraction measurements at 26 GHz.

location, the 35.5 cm long linear track was used to measure a 20° swath of diffraction angles in the horizontal plane (parallel to the ground). Five consecutive RX linear track locations were used to simulate a contiguous arc around the corner to measure a 100° swath of total diffraction angles, which enabled the RX antenna to move from the deep shadow region to the lit region. There were five consecutive RX linear track locations formed in an arc, as shown in Fig. 4.20. The corresponding diffraction angles for different incident angles can be found in Fig. 4.18 and Table 4.2. A free space calibration was performed at each measured frequency at a TX-RX separation distance of 3 m (d_1+d_2 = 3 m). The relative diffraction loss was obtained by computing the difference between

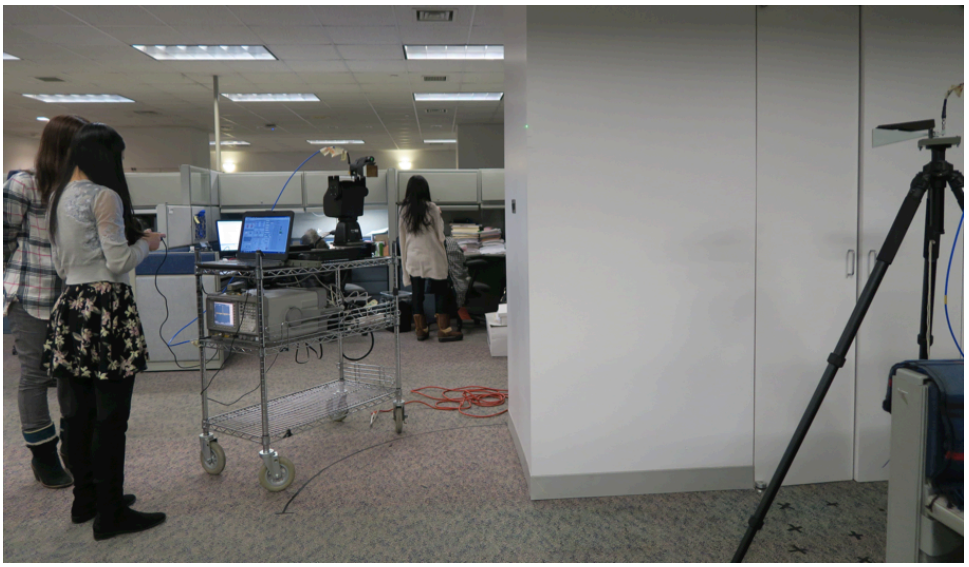

FIGURE 4.22: Indoor drywall corner diffraction measurements at 26 GHz.

FIGURE 4.23: Indoor wooden corner diffraction measurements at 26 GHz.

the calibration received power and the measured power level at each diffraction angle measurement. The measurement procedures of the outdoor measurements were similar to the indoor measurements.

FIGURE 4.24: Indoor wooden diffraction measurements at 26 GHz.

FIGURE 4.25: Indoor plastic board diffraction measurements at 26 GHz.

FIGURE 4.26: Indoor plastic board diffraction measurements at 26 GHz.

FIGURE 4.27: Pillar

FIGURE 4.28: Marble corner.

Chapter 5

Indoor Measurement Results and Analysis

5.1 Indoor V-V Polarization Measurement Results

5.1.1 Drywall Corner Measurements

Drywall is one of the most common materials in the indoor environment as shown in Fig. 4.16. Fig. 5.1, Fig. 5.2, and Fig. 5.3 show the measured relative diffraction losses at 10, 20, and 26 GHz, respectively, as a function of diffraction angle for different incident angles at a drywall corner for V-V polarized antennas. The relative loss at each frequency includes measured relative loss at three different TX incident angles (12°, 23°, and 35°). It is worth noting that the KED model is not a function of incident angle, therefore, relative losses for different incident angles are compared with one KED model in each plot. In the shadow region (for diffraction angles α greater than 0°), a good agreement can be observed between the measurement data and the KED model prediction. When the RX antenna moved from the lit region to the shadow region, the relative diffraction loss increased from 6 dB to approximately 25 dB at a diffraction angle of 20°. The main mechanisms in the lit region are direct transmission through free space and reflections

in the environment, which are not predicted by the KED model. The relative loss in the lit region can be explained by the reduced antenna gain off boresight of the directional antenna. The diffraction loss at a 0° diffraction angle should be 6 dB according to the KED theory, but the observed diffraction loss is less than 6 dB, due to the use of directional antennas. Similar results at 10 GHz were also observed in [17]. Fig. 5.4 shows the measured relative diffraction losses at 10, 20, and 26 GHz as a function of diffraction angle. Due to the reflective indoor environment, the diffraction loss showed no obvious dependence on frequency. The simple KED model provides a reasonable fit for the measurement data in the shadow region and near the shadow boundary for drywall material. Table 5.1 provides the mean error (ME) and standard deviation (SD) values for each frequency at different incident angles and for combined incident angles. The ME values are close to zero, indicating a good overall match between the KED model and the measured data. The high SD values (approximately 5-6 dB) of the model as shown in the Table 5.1, and the oscillation patterns observed in the figures, are likely due to the penetration through the measured drywall material (with metal studs inside the wall).

Table 5.4 shows the measured diffraction loss and Table 5.5 shows predicted diffraction loss (by Eq.(3.7)) in a 10° interval for diffraction angles from 0° to 60°. The results show approximately 0.4 dB greater diffraction loss at 26 GHz than 20 GHz, and 11.8 dB greater loss at 10 GHz than 20 GHz in a diffraction angle interval of 20 - 30°, as shown in Table 5.4. For an interval of 50-60 ° diffraction angle, diffraction loss at 26 GHz is approximately 2.3 dB greater than 20 GHz measurements, and diffraction loss at 10 GHz is 2.1 dB greater than 20 GHz measurements. This clearly shows how indoor environments have less diffraction loss over frequency than predicted by the KED model. Table 5.6 shows the differences between the measured diffraction loss and predicted diffraction loss. The results show approximately 17.0 dB, 2.2 dB, and 1.4 dB differences at 10, 20, and 26 GHz in a diffraction angle interval of 20 - 30°.

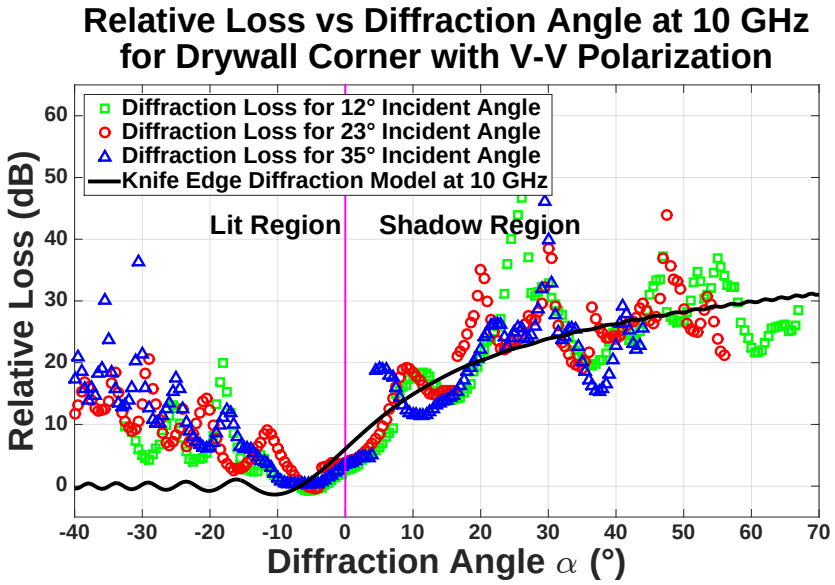

FIGURE 5.1: Indoor drywall corner diffraction measurement results compared to the KED model at 10 GHz for V-V polarized antennas.

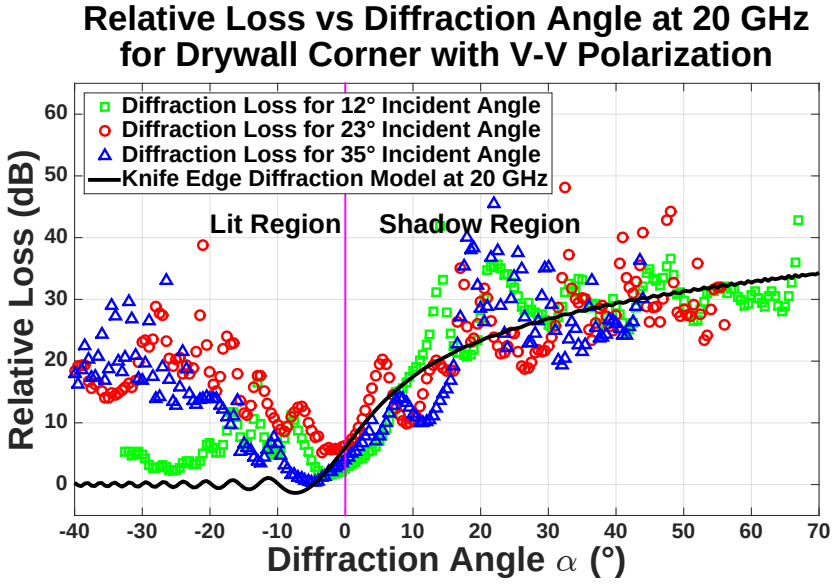

FIGURE 5.2: Indoor drywall corner diffraction measurement results compared to the KED model at 20 GHz for V-V polarized antennas.

5.1.2 Wooden Corner Measurements

Wooden corners with smooth surfaces are also common in the office and at home as shown in Fig. 4.16. The top part of the measured corner is a wooden decoration and the bottom part of the corner is typically drywall. Fig. 5.5, Fig. 5.6, and Fig. 5.7 show the

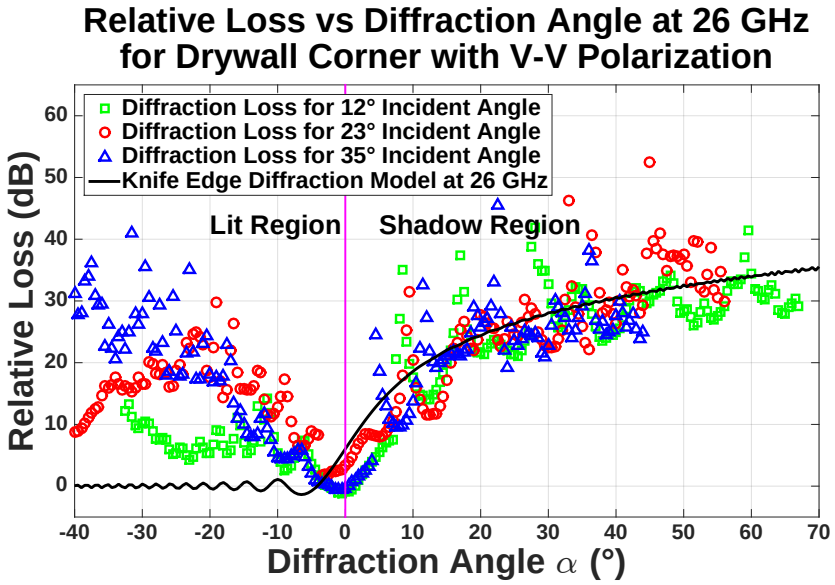

FIGURE 5.3: Indoor drywall corner diffraction measurement results compared to the KED model at 26 GHz for V-V polarized antennas.

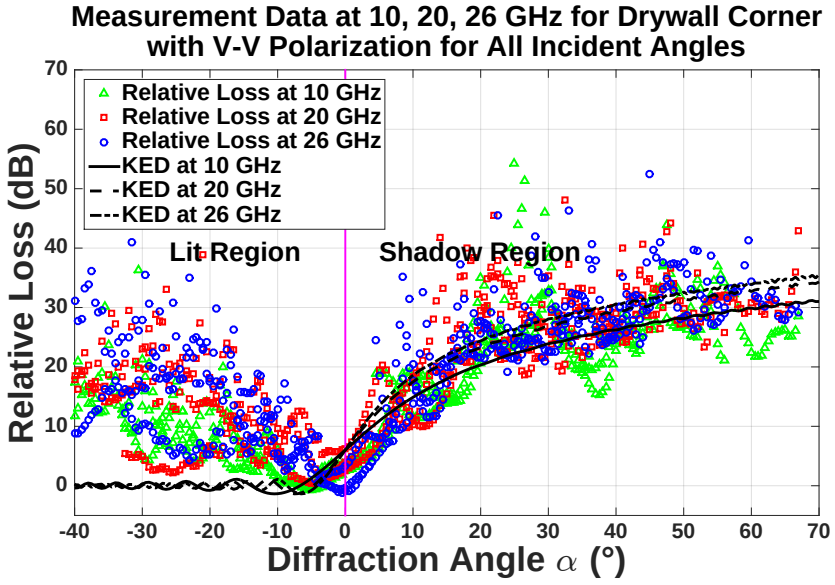

FIGURE 5.4: Indoor drywall corner diffraction measurement results compared to the KED model at 10, 20, and 26 GHz for V-V polarized antennas.

indoor wooden corner measurement results compared to the KED prediction at 10, 20, and 26 GHz, respectively, as a function of diffraction angle at a wooden corner for V-V polarized antennas. The relative loss at each frequency includes measured relative loss for three different TX incident angles (11°, 26°, and 38°). Fig. 5.8 shows the measured relative diffraction losses at 10, 20, and 26 GHz as a function of diffraction angle. Due

TABLE 5.1: Mean error (ME) and standard deviation (SD) between the measurement data and KED model prediction for drywall corner in the indoor environment at 10, 20, and 26 GHz for V-V polarized antennas. "Comb." means measurement data that combines data from all incident angles.

Frequency (GHz)	Incident Angle (°)	ME (dB)	SD (dB)
10	12	0.65	6.75
	23	1.04	4.70
	35	-0.46	5.45
	Comb.	0.49	5.79
20	12	0.63	4.71
	23	-0.02	5.17
	35	-0.50	6.64
	Comb.	0.11	5.43
26	12	-1.95	4.96
	23	-0.25	5.18
	35	-1.80	5.05
	Comb.	-1.34	5.06

to the reflective indoor environment, the diffraction loss showed no obvious dependence on frequency. In the shadow region, the KED model, in general, overestimates the measurement data. Table 5.2 provides the mean error (ME) and standard deviation (SD) values for each frequency at different incident angles and for combined incident angles. According to the negative ME values in Table 5.2, the KED model overestimates the measurement results by 4.06 dB, 4.09 dB and 1.54 dB at 10, 20, and 26 GHz, respectively, in the shadow region and near the shadow boundary. The relative diffraction loss increases to approximately 30 dB at a diffraction angle of 30°. The results between the drywall corner and wooden corner are comparable, indicating that dependence on similar building materials may be negligible for diffraction in the indoor environment. The high SD values (approximately 6 dB) and the oscillation patterns are likely due to

the penetration through the measured material and the reflective test environment. In the comparison to the measurement result, the KED model overestimate the measured data in most cases. From the simulation comparison results in Chapter 4, the KED model is the optimal (with the smallest diffraction loss compared to the other models). Therefore, the absorbing screen model, conducting screen model, and the right wedge screen model overestimate the measurement results (ME values would be much smaller than the KED model) and are not included in this chapter.

Table 5.4 shows the measured diffraction loss and Table 5.5 shows predicted diffraction loss (by Eq.(3.7)) in a 10° interval for diffraction angles from 0° to 60°. The results show approximately 8.5 dB greater diffraction loss at 26 GHz than 20 GHz, and 3.3 dB greater loss at 20 GHz than 10 GHz in a diffraction angle interval of 20 - 30°, as shown in Table 5.4. For an interval of 50-60 ° diffraction angle, diffraction loss at 26 GHz is approximately 3.8 dB greater than 20 GHz measurements, and diffraction loss at 10 GHz is 16.1 dB greater than 20 GHz measurements. Table 5.6 shows the differences between the measured diffraction loss and predicted diffraction loss. The results show approximately -5.9 dB, -5.6 dB, and 1.7 dB differences at 10, 20, and 26 GHz in a diffraction angle interval of 20 - 30°.

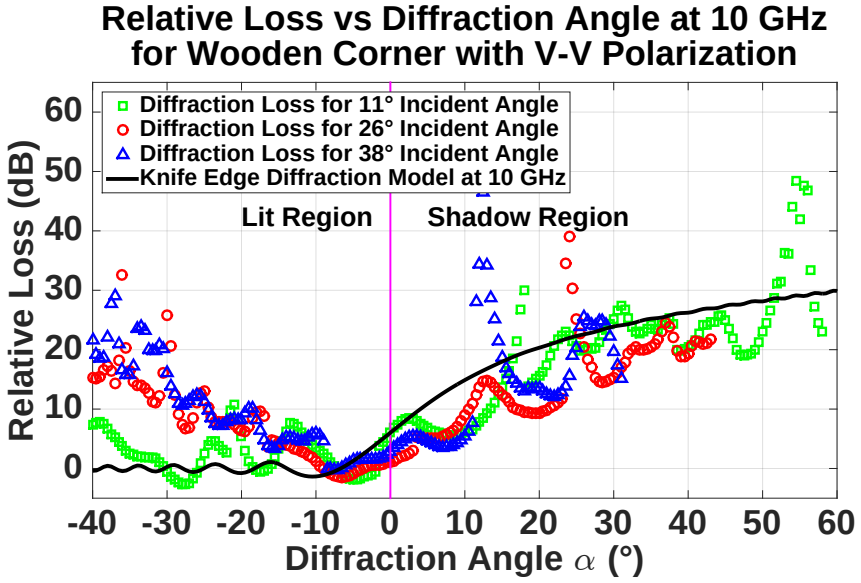

FIGURE 5.5: Indoor wooden corner diffraction measurement results compared to the KED model at 10 GHz for V-V polarized antennas.

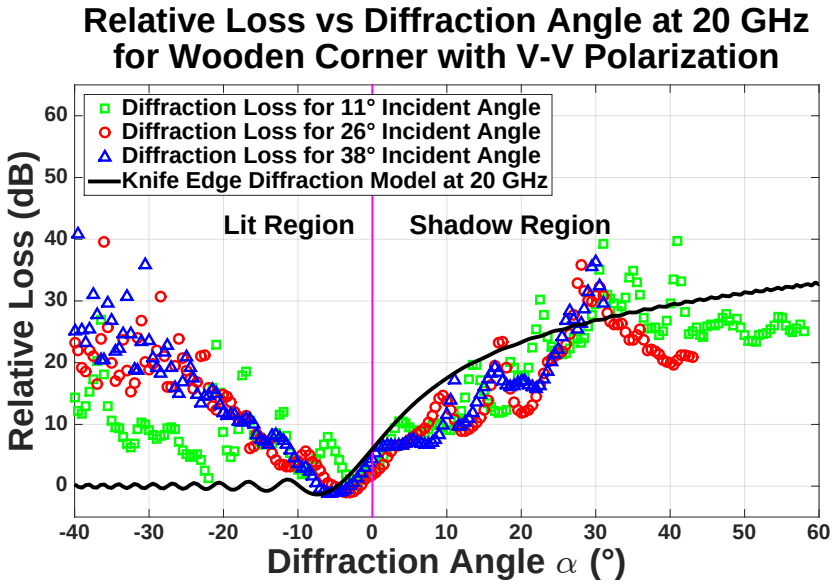

FIGURE 5.6: Indoor wooden corner diffraction measurement results compared to the KED model at 20 GHz for V-V polarized antennas.

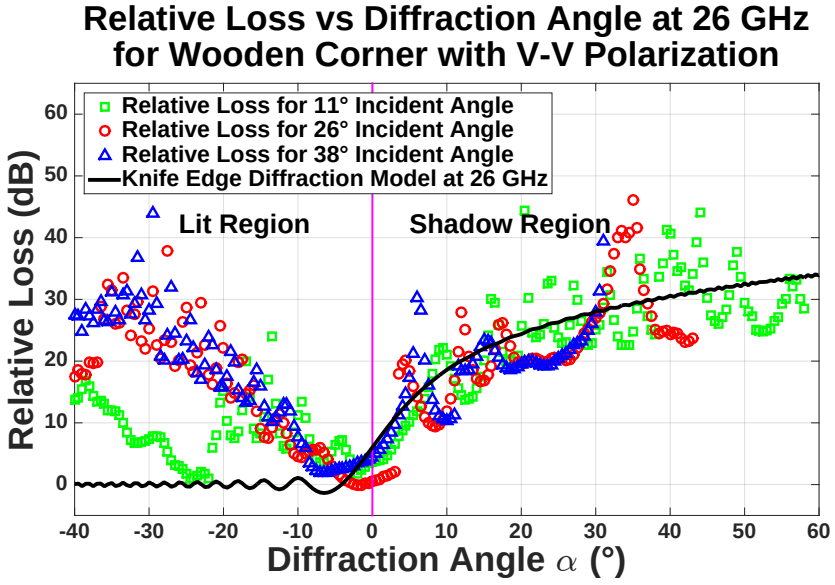

FIGURE 5.7: Indoor wooden corner diffraction measurement results compared to the KED model at 10 GHz for V-V polarized antennas.

5.1.3 Plastic Board Measurements

Diffraction around an irregular object, such as a plastic board, was also measured. Plastic board is commonly used as a decoration or light weight partition as shown in Fig. 4.16. Fig. 5.9, Fig. 5.10, and Fig. 5.11 show the indoor plastic board measurement

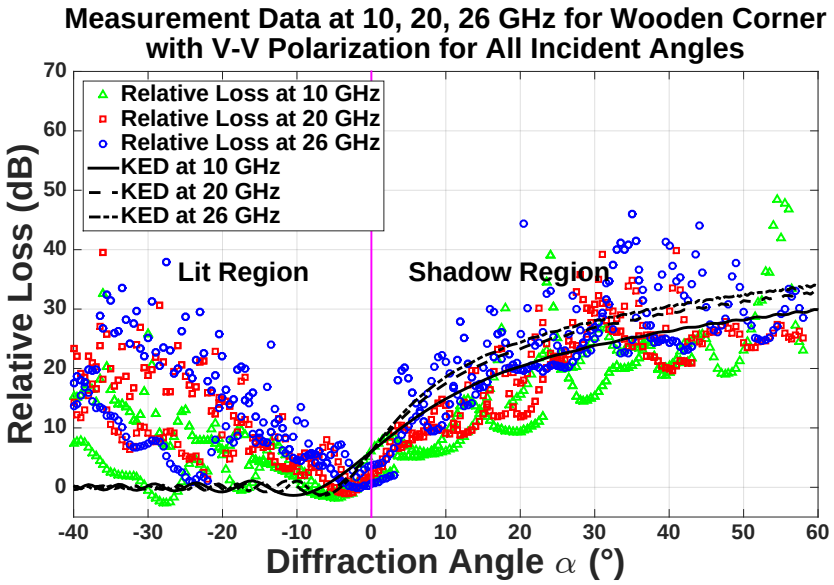

FIGURE 5.8: Indoor wooden corner diffraction measurement results compared to the KED model at 10, 20, and 26 GHz for V-V polarized antennas.

results compared to the KED prediction at 10, 20, and 26 GHz, respectively, as a function of diffraction angle at a wooden corner for V-V polarized antennas. The relative loss at each frequency includes measured diffraction loss at three different TX incident angles (10°, 23°, and 39°). For the shadow region near the shadow boundary (diffraction angle from 0° to 30°), the KED model overestimates the measured relative diffraction loss, but in the deep shadow region, the KED model underestimates the measured relative diffraction loss, likely due to penetration through the semitransparent plastic board. Fig. 5.12 shows the observed relative diffraction losses at 10, 20, and 26 GHz as a function of diffraction angle. Due to the reflective indoor environment, the diffraction loss showed no obvious dependence on frequency. In the shadow region, the KED model, in general, overestimates the measurement data. Table 5.3 provides the mean error (ME) and standard deviation (SD) values for each frequency at different incident angles and for combined incident angles. According to the negative ME values in Table 5.3, the KED model overestimates the measurement results by 3.72 dB, 3.18 dB and 4.15 dB at 10, 20, and 26 GHz, respectively, in the shadow region and near the shadow boundary. The high SD values (approximately 4-7 dB) and the oscillation patterns are highly due to the penetration through the measured material and the reflective test environment.

TABLE 5.2: Mean error (ME) and standard deviation (SD) between the measurement data and KED model prediction for wooden corner in the indoor environment at 10, 20, and 26 GHz for V-V polarized antennas. "Comb." means measurement data that combines data from all incident angles.

Frequency (GHz)	**Incident Angle (°)**	**ME (dB)**	**SD (dB)**
10	**11**	**-1.97**	**5.55**
	26	**-5.47**	**4.41**
	38	**-2.84**	**7.56**
	Comb.	**-3.32**	**5.77**
20	**11**	**-3.19**	**4.27**
	26	**-4.70**	**4.51**
	38	**-4.02**	**4.32**
	Comb.	**-3.88**	**4.36**
26	**11**	**-0.94**	**4.93**
	26	**-1.94**	**5.86**
	38	**-2.11**	**4.76**
	Comb.	**-1.54**	**5.21**

Table 5.4 shows the measured diffraction loss and Table 5.5 shows predicted diffraction loss (by Eq.(3.7)) in a 10° interval for diffraction angles from 0° to 60°. The results show approximately 8.9 dB greater diffraction loss at 20 GHz than 26 GHz, and 5.1 dB greater loss at 10 GHz than 20 GHz in a diffraction angle interval of 20 - 30°, as shown in Table 5.4. For an interval of 50-60 ° diffraction angle, diffraction loss at 26 GHz is approximately 3.1 dB greater than 20 GHz measurements, and diffraction loss at 20 GHz is 8.8 dB greater than 10 GHz measurements. This clearly shows how indoor environments have less diffraction loss over frequency than predicted by the KED model. Table 5.6 shows the differences between the measured diffraction loss and predicted diffraction loss. The results show approximately 4.8 dB, -3.3 dB, and -13.4 dB differences at 10, 20, and 26 GHz in a diffraction angle interval of 20 - 30°.

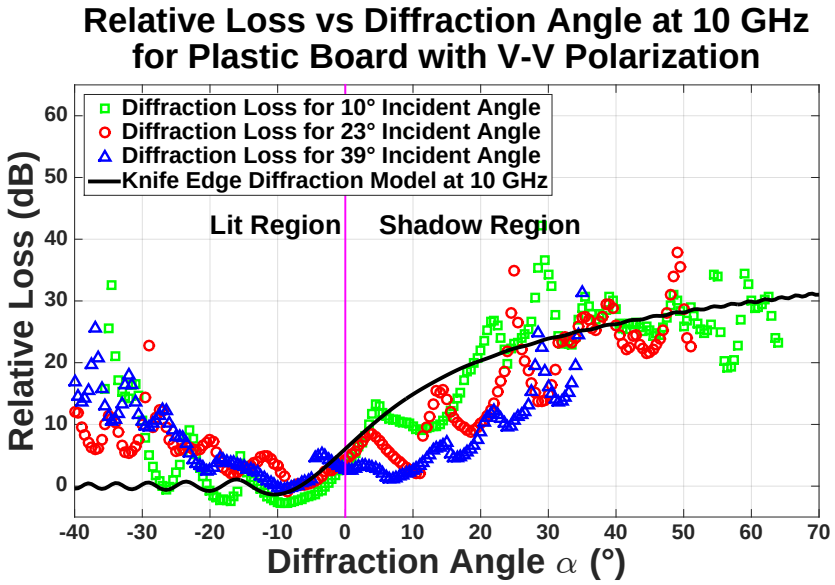

FIGURE 5.9: Indoor plastic board diffraction measurement results compared to the KED model at 10 GHz for V-V polarized antennas.

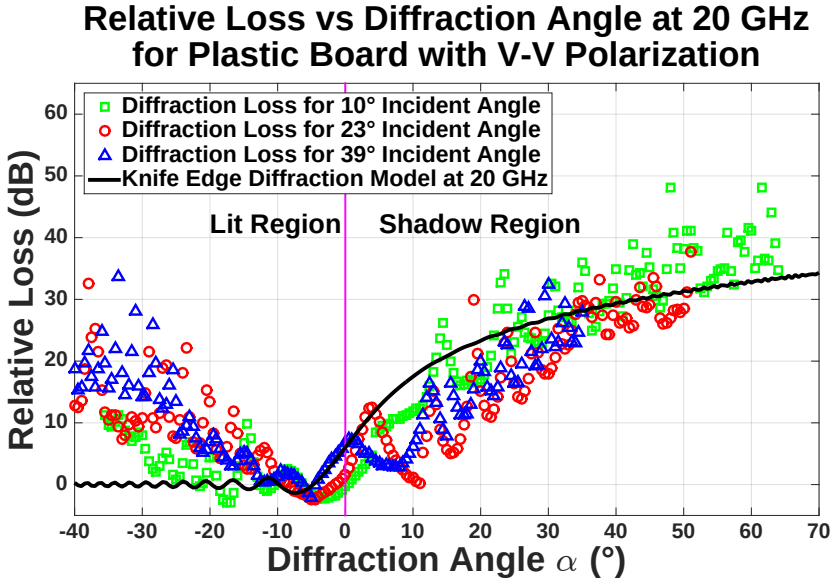

FIGURE 5.10: Indoor plastic board diffraction measurement results compared to the KED model at 20 GHz for V-V polarized antennas.

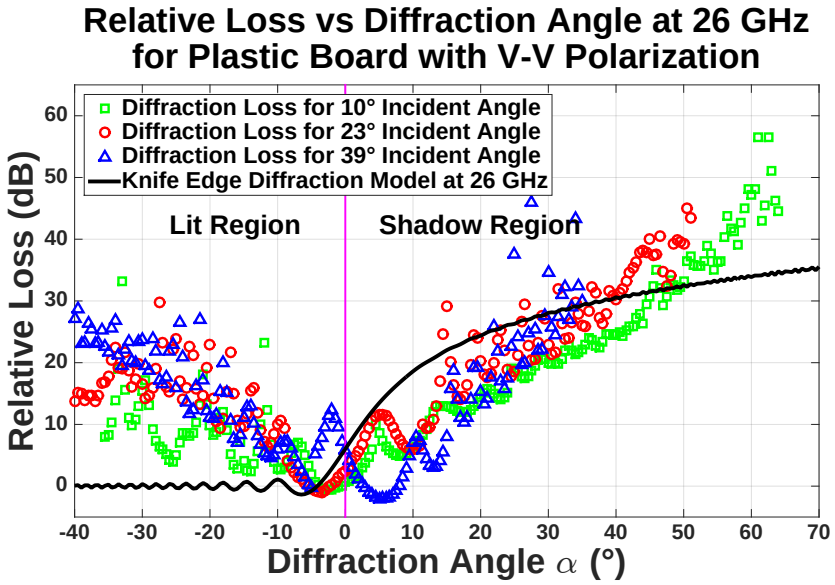

FIGURE 5.11: Indoor plastic board diffraction measurement results compared to the KED model at 26 GHz for V-V polarized antennas.

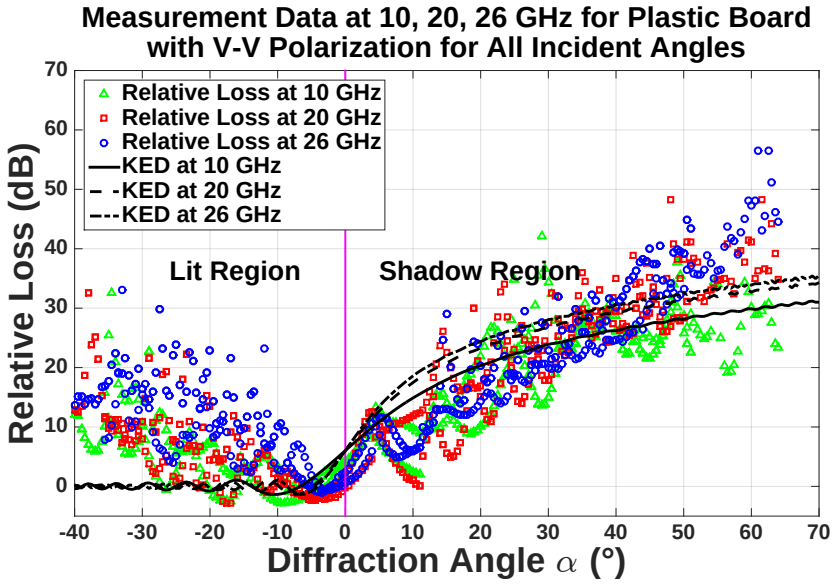

FIGURE 5.12: Indoor plastic board diffraction measurement results compared to the KED model at 10, 20, and 26 GHz for V-V polarized antennas.

5.2 Indoor H-V Polarization Measurement Results

5.2.1 Drywall Corner Measurements

Fig. 5.13, Fig. 5.14, and Fig. 5.15 show the measured relative diffraction losses at 10, 20, and 26 GHz, respectively, as a function of diffraction angle for a drywall corner for

TABLE 5.3: Mean error (ME) and standard deviation (SD) between the measurement data and KED model prediction for plastic board in the indoor environment at 10, 20, and 26 GHz for V-V polarized antennas. "Comb." means measurement data that combines data from all incident angles.

Frequency (GHz)	**Incident Angle (°)**	**ME (dB)**	**SD (dB)**
10	**10**	**-0.55**	**4.51**
	23	**-3.77**	**5.02**
	39	**-9.40**	**3.92**
	Comb.	**-3.72**	**4.56**
20	**10**	**0.41**	**5.24**
	23	**-5.65**	**5.71**
	39	**-6.14**	**4.47**
	Comb.	**-3.18**	**5.24**
26	**10**	**-3.83**	**7.75**
	23	**-2.21**	**5.70**
	39	**-7.57**	**7.83**
	Comb.	**-4.15**	**7.14**

H-V polarized antennas. The relative loss at each frequency includes measured relative loss at three different TX incident angles (12°, 23°, and 35°). The cross-polarization discrimination factors (XPD) are extracted from all H-V measurements. For H-V polarized antennas, the diffraction loss increased with frequency, but for each frequency, the diffraction loss was relatively independent of diffraction angle, indicating a depolarization effect of the diffracted wave at the edge of the corner. In general, due to the depolarization effect, the prediction by KED theory overestimates the diffraction loss in H-V scenario.

TABLE 5.4: Average measured diffraction loss (in dB) in a 10° interval for diffraction angle from 0° to 60° for drywall corner, wooden corner, and plastic board at 10, 20, and 26 GHz. "Comb." means taking average value from the three different materials. The average values are taken by converting the power levels measured in dB scale to linear scale, then calculating average values in linear scale, and converting the values back to dB scale.

Material	Frequency (GHz)	Diffraction Angle(°)					
		0-10	10-20	20-30	30-40	40-50	50-60
Drywall	10	6.43	11.97	39.21	21.12	24.93	27.58
	20	5.59	25.69	37.40	24.99	27.48	25.50
	26	18.46	22.08	27.77	24.16	26.19	27.83
Wooden	10	2.16	15.17	16.36	19.54	18.01	36.60
	20	3.90	11.01	19.63	26.98	25.54	20.55
	26	10.36	17.90	28.09	27.67	31.45	24.40
Pleastic	10	5.28	10.12	27.00	23.94	22.28	24.05
	20	3.44	14.35	21.89	25.58	33.27	32.92
	26	0.62	6.94	12.97	17.76	25.51	36.00
Comb.	10	4.97	12.93	34.71	21.92	22.58	32.55
	20	4.88	21.36	24.23	25.93	30.06	29.08
	26	14.37	18.81	26.24	24.80	28.59	32.10

TABLE 5.5: Average predicted diffraction loss (in dB) using the KED model by (3.7) in a 10° interval for diffraction angle from 0° to 60° at 10, 20, and 26 GHz. "-" means the KED model is independent of material types. The average values are taken by converting the power levels measured in dB scale to linear scale, then calculating average values in linear scale, and converting the values back to dB scale.

Material	Frequency (GHz)	Diffraction Angle(°)					
		0-10	10-20	20-30	30-40	40-50	50-60
-	10	11.25	18.01	22.23	25.13	27.31	29.05
	20	13.24	20.87	25.22	28.13	30.31	32.07
	26	14.11	22.00	26.35	29.27	31.45	33.21

TABLE 5.6: Differences between the measured diffraction loss and predicted diffraction loss (in dB) in a 10° interval for diffraction angle from 0° to 60° for drywall corner, wooden corner, and plastic board at 10, 20, and 26 GHz. "Comb." means taking average value from the three different materials. The average values are taken by converting the power levels measured in dB scale to linear scale, then calculating average values in linear scale, and converting the values back to dB scale.

Material	**Frequency (GHz)**	**Diffraction Angle(°)**					
		0-10	**10-20**	**20-30**	**30-40**	**40-50**	**50-60**
Drywall	**10**	**-4.82**	**-6.04**	**16.98**	**-4.01**	**-2.38**	**-1.46**
	20	**-6.65**	**4.82**	**2.18**	**-3.13**	**-2.83**	**-6.57**
	26	**4.35**	**-0.08**	**1.42**	**-5.11**	**-5.25**	**-5.37**
Wooden	**10**	**-9.09**	**-2.84**	**-5.87**	**-5.59**	**-9.30**	**7.55**
	20	**-9.34**	**-9.86**	**-5.59**	**-1.15**	**-4.77**	**-11.52**
	26	**-3.75**	**-4.10**	**1.74**	**-1.60**	**0**	**-8.81**
Pleastic	**10**	**-5.97**	**-7.89**	**4.77**	**-1.19**	**-5.03**	**-5.00**
	20	**-9.80**	**-6.52**	**-3.33**	**-2.55**	**2.96**	**0.85**
	26	**-13.49**	**-15.06**	**-13.38**	**-11.51**	**-5.94**	**2.79**
Comb.	**10**	**-6.29**	**-5.08**	**12.48**	**-3.21**	**-4.73**	**3.50**
	20	**-8.36**	**0.49**	**-0.99**	**-2.20**	**-0.25**	**-2.99**
	26	**0.26**	**-3.19**	**-0.11**	**-4.47**	**2.86**	**-1.11**

5.2.2 Wooden Corner Measurements

Fig. 5.16, Fig. 5.17, and Fig. 5.18 show the measured relative diffraction losses at 10, 20, and 26 GHz, respectively, as a function of diffraction angle for a wooden corner for H-V polarized antennas. The relative loss at each frequency includes measured relative loss at three different TX incident angles (11°, 26°, and 38°). The XPDs are extracted from all H-V measurements. For H-V polarized antennas, the diffraction loss increased with frequency, but for each frequency, the diffraction loss was relatively independent of diffraction angle, indicating a depolarization effect of the diffracted wave at the edge of the corner. In general, due to the depolarization effect, the prediction by KED theory overestimates the diffraction loss in H-V scenario.

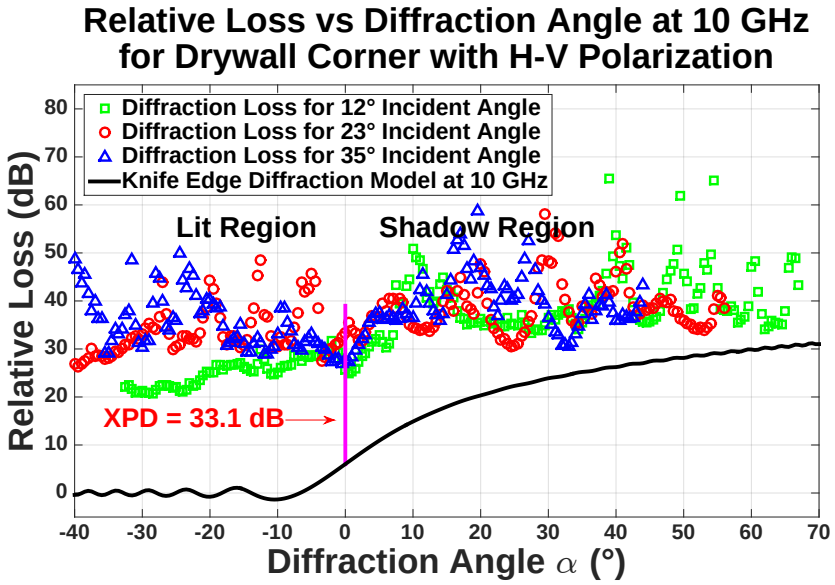

FIGURE 5.13: Indoor drywall corner diffraction measurement results compared to the KED model at 10 GHz for H-V polarized antennas.

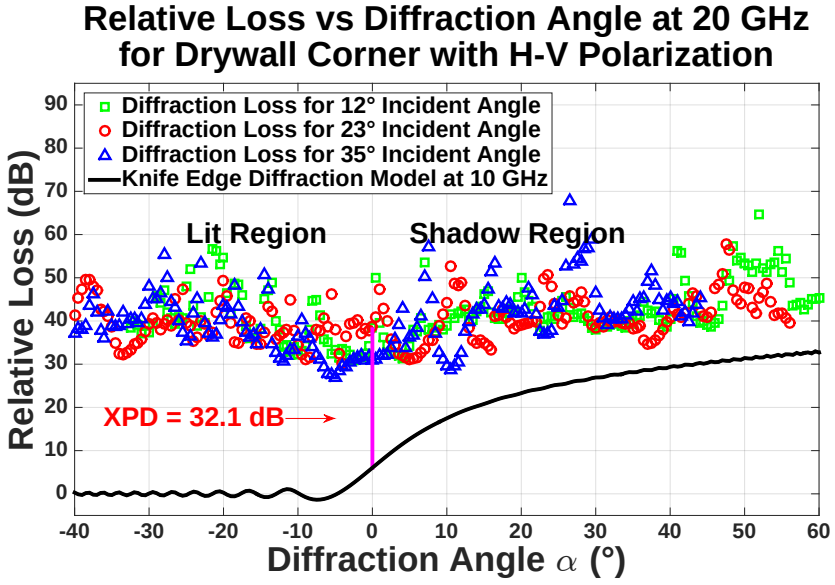

FIGURE 5.14: Indoor drywall corner diffraction measurement results compared to the KED model at 10 GHz for H-V polarized antennas.

5.2.2.1 Plastic Board Measurements

Fig. 5.19, Fig. 5.20, and Fig. 5.21 show the measured relative diffraction losses at 10, 20, and 26 GHz, respectively, as a function of diffraction angle for a plastic board for H-V polarized antennas. The relative loss at each frequency includes measured relative

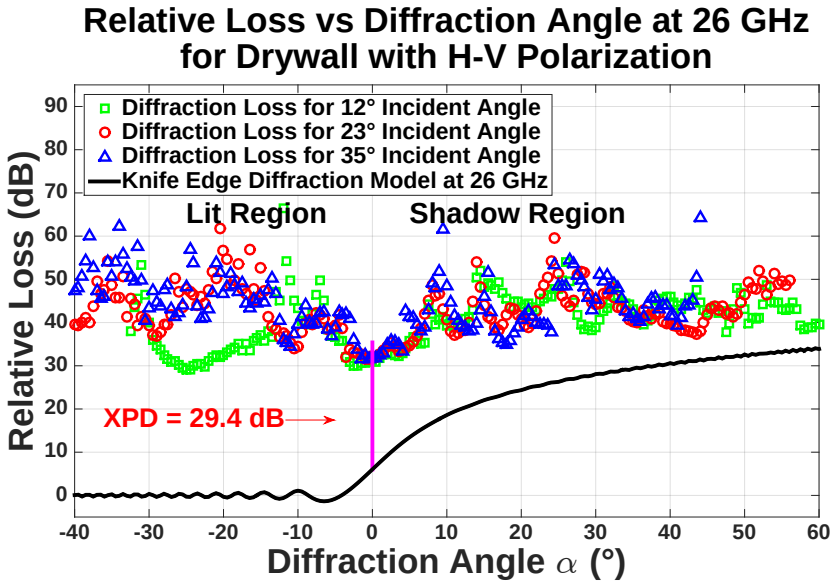

FIGURE 5.15: Indoor drywall corner diffraction measurement results compared to the KED model at 10 GHz for H-V polarized antennas.

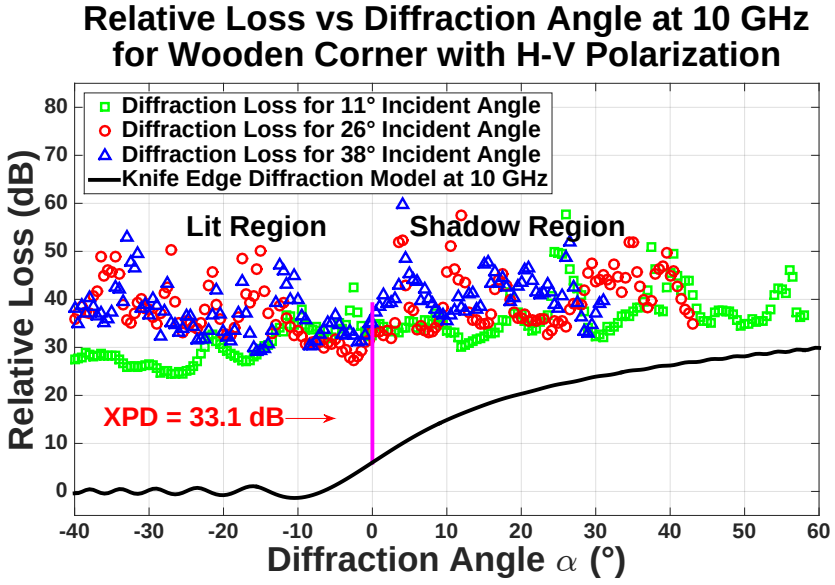

FIGURE 5.16: Indoor wooden corner diffraction measurement results compared to the KED model at 10 GHz for H-V polarized antennas.

loss at three different TX incident angles (10°, 23°, and 39°). The XPDs are extracted from all H-V measurements. For H-V polarized antennas, the diffraction loss increased with frequency, but for each frequency, the diffraction loss was relatively independent of diffraction angle, indicating a depolarization effect of the diffracted wave at the edge of the corner. In general, due to the depolarization effect, the prediction by KED theory

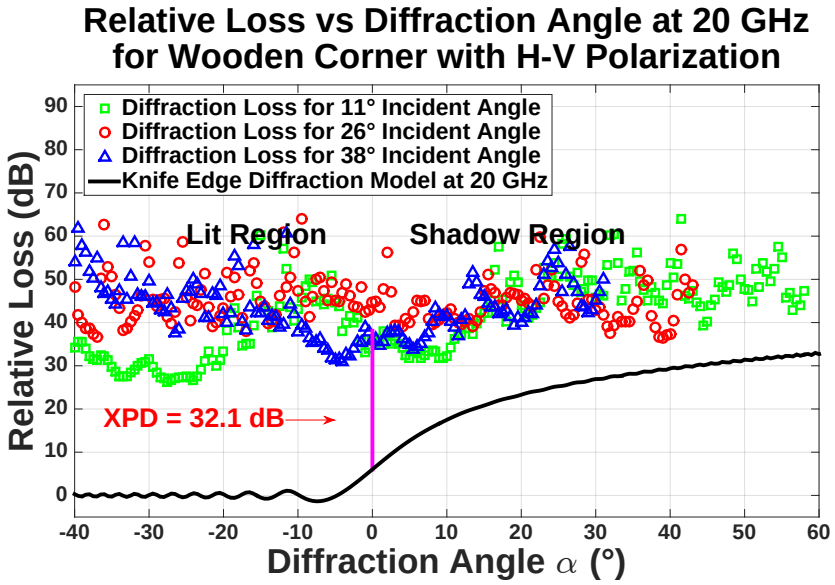

FIGURE 5.17: Indoor wooden corner diffraction measurement results compared to the KED model at 20 GHz for H-V polarized antennas.

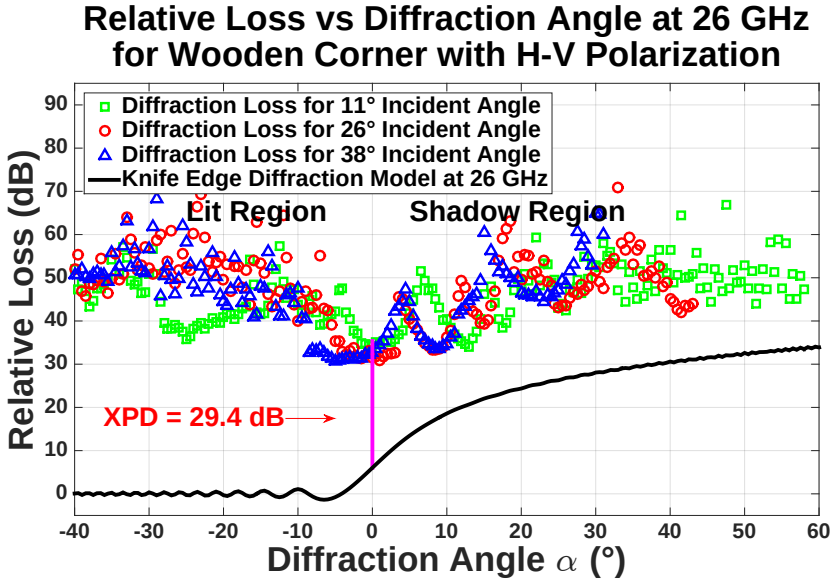

FIGURE 5.18: Indoor wooden corner diffraction measurement results compared to the KED model at 26 GHz for H-V polarized antennas.

overestimates the diffraction loss in H-V scenario.

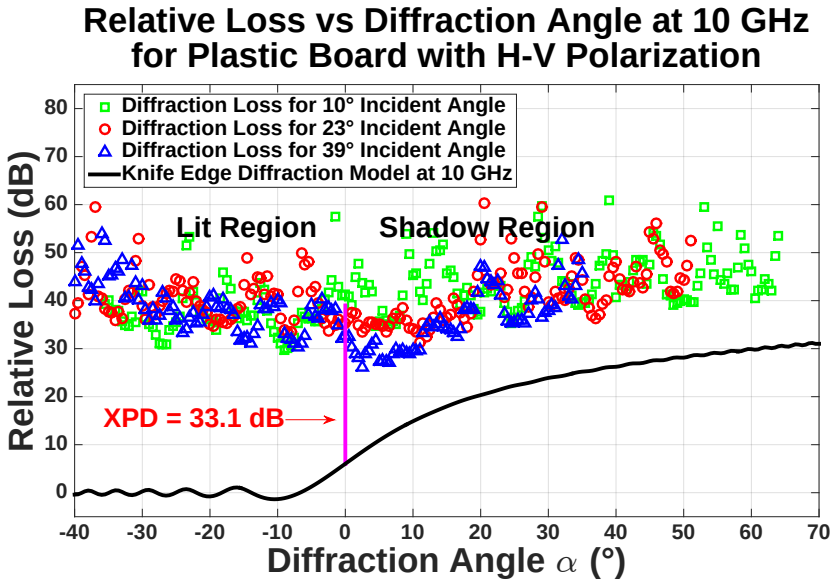

FIGURE 5.19: Indoor plastic board diffraction measurement results compared to the KED model at 10 GHz for H-V polarized antennas.

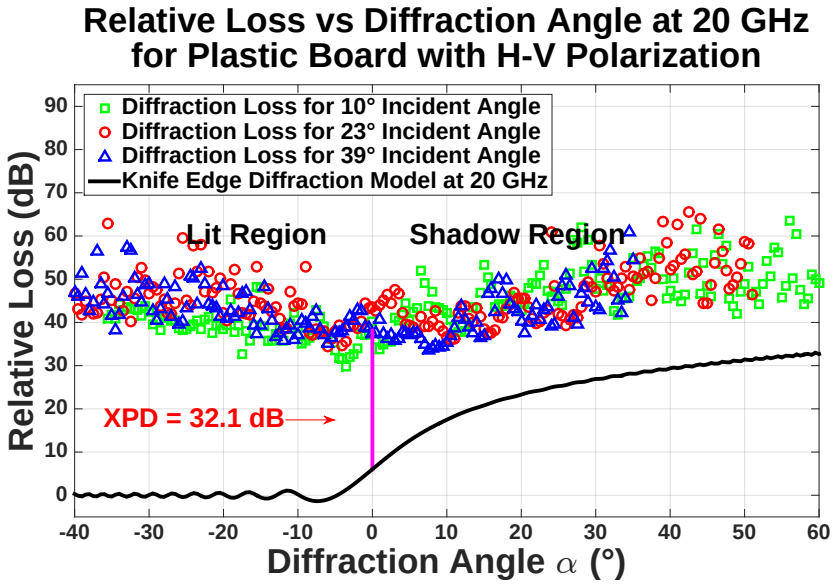

FIGURE 5.20: Indoor plastic board diffraction measurement results compared to the KED model at 20 GHz for H-V polarized antennas.

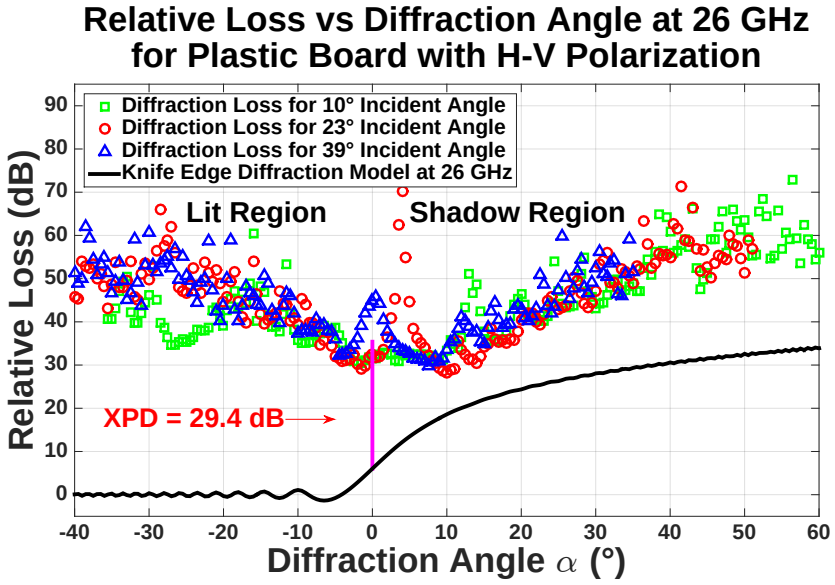

FIGURE 5.21: Indoor plastic board diffraction measurement results compared to the KED model at 26 GHz for H-V polarized antennas.

Chapter 6

Outdoor Measurement Results and Analysis

6.1 Outdoor V-V Polarization Measurement Results

6.1.1 Stone Pillar Measurements

Stone is a commonly used outdoor structural material and stone pillars are typically used for building support or decoration as shown in Fig. 4.16. The surface of the measured stone pillar is rough and the corners of the pillar are rounded. Fig. 6.1, Fig. 6.2, and Fig. 6.3 show the measured relative diffraction losses at 10, 20, and 26 GHz, respectively, as a function of diffraction angle at a stone pillar for V-V polarized antennas. The relative loss at each frequency includes measured relative loss at two different TX incident angles (12° and 23°). It is worth noting that the KED model is not a function of incident angle, therefore, relative losses for different incident angles are compared with one KED model in each plot. The outdoor stone pillar measurement results are compared to prediction by the KED model and the creeping wave model. From the plot, the linear creeping wave model using minimum mean square error (MMSE) estimation provides a better fit to the measured relative diffraction loss in the shadow region than the KED model. The

main propagation mechanisms in the lit region are direct transmission through free space and reflections in the environment, which are not predicted by the KED model and the creeping wave model. The anchor point of the creeping wave model is 6.03 dB, which is the corresponding diffraction loss predicted by the KED model at the 0° diffraction angle. The slope of the linear creeping wave model is 0.75, 0.88, and 0.96 at 10, 20, and 26 GHz, respectively, according to Eq.(3.29). The KED model underestimates diffraction for diffracted angles greater than 20°. Table 6.1 provides the mean error (ME) and standard deviation (SD) values for each frequency at different incident angles and for combined incident angles. The ME values for the creeping wave model are close to zero, which are much less than the ME values of the KED model, indicating a good overall match between the creeping wave model and the measured data. The SD values for creeping wave model (approximately 2-4 dB) are smaller than the SD values for KED model (approximately 6-11 dB).

Fig. 6.4 shows the outdoor stone pillar measurement results compared to the creeping wave model prediction at 10, 20, and 26 GHz for V-V polarized antennas. The relative loss for each frequency includes measured loss at two TX incident angles, and is plotted as a function of diffraction angle. The simple linear creeping wave model provides a reasonable fit data in the shadow region and near the shadow boundary. Table 6.4 shows the measured diffraction loss and Table 6.5 shows predicted diffraction loss (by Eq.(3.28)) in a 10° interval for diffraction angles from 0° to 60°. The results show approximately 2.2 dB greater diffraction loss at 26 GHz than 20 GHz, and 5.1 dB greater loss at 20 GHz than 10 GHz in a diffraction angle interval of 20 - 30°, as shown in Table 6.4. For an interval of 50-60 ° diffraction angle, diffraction loss at 26 GHz is approximately 0.1 dB greater than 20 GHz measurements, and diffraction loss at 20 GHz is 12.7 dB greater than 10 GHz measurements. Table 6.6 shows the differences between the measured diffraction loss and predicted diffraction loss. The results show approximately 1.9 dB, 3.5 dB, and 3.6 dB differences at 10, 20, and 26 GHz in a diffraction angle interval of 20 - 30°.

The ME and SD values at 10, 20, and 26 GHz for combined TX incident angles can be found in Table 6.1. The ME values of the creeping wave model for combined incident angles are less than 0.5, indicating a good match to the measurement results. The absorbing screen model, conducting screen model, and right wedge screen model overestimate the measurement results in the shadow region especially for diffraction angles from 0° to 30° (ME values would be much smaller than the linear creeping wave model) and are not included in this chapter.

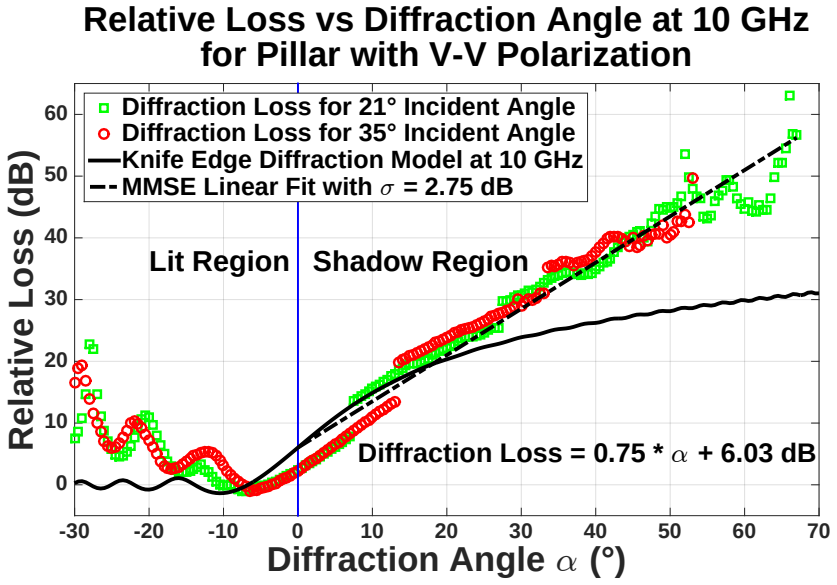

FIGURE 6.1: Outdoor stone pillar diffraction measurement results compared to the KED model and the empirical linear creeping wave model at 10 GHz for V-V polarized antennas. 0.75 is the slope value n in the creeping wave model calculated from Eq.(3.29).

6.1.2 Marble Corner Measurements

Marble is also one of the common outdoor surface materials, and is often used in exterior walls and veneers, flooring, and decorative features as shown in Fig. 4.16. Marble is an extremely hard, metamorphic stone composed of calcite, and is formed as a result of the recrystallization of limestone under the intense pressure and heat of geologic processes. The surface of marble is smooth and the marble corner is usually less rounded than pillar but more rounded than the indoor sharp corner. Fig. 6.5, Fig. 6.6, and Fig. 6.7 show the measured relative diffraction losses at 10, 20, and 26 GHz, respectively, as a function of

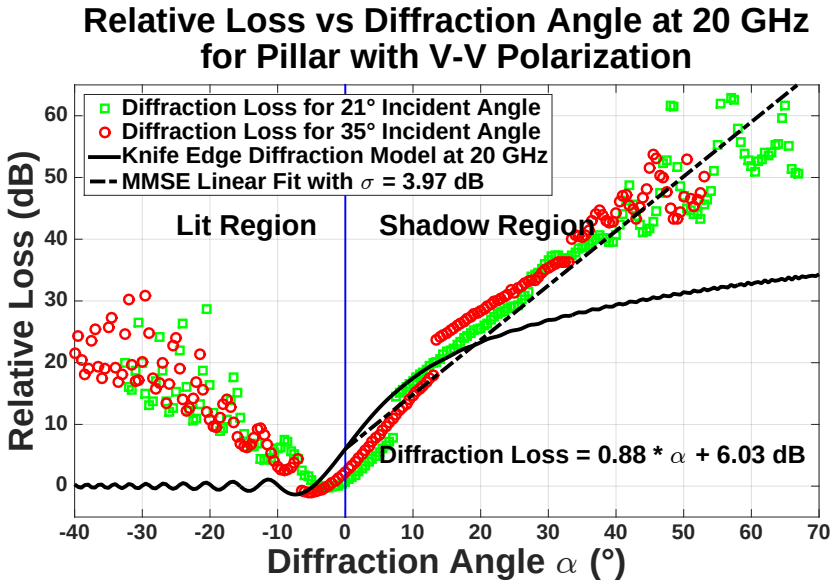

FIGURE 6.2: Outdoor stone pillar diffraction measurement results compared to the KED model and the empirical linear creeping wave model at 20 GHz for V-V polarized antennas. 0.88 is the slope value n in the creeping wave model calculated from Eq.(3.29).

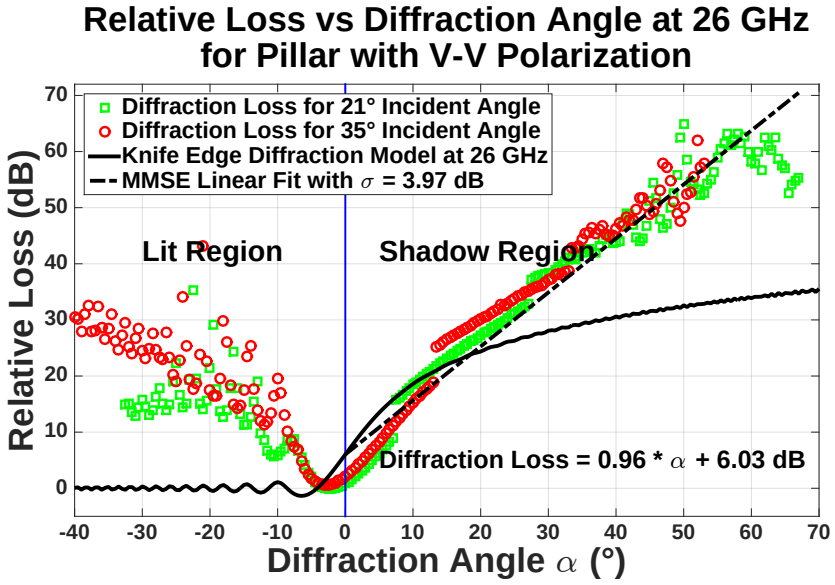

FIGURE 6.3: Outdoor stone pillar diffraction measurement results compared to the KED model and the empirical linear creeping wave model at 26 GHz for V-V polarized antennas. 0.96 is the slope value n in the creeping wave model calculated from Eq.(3.29).

diffraction angle at a marble corner for V-V polarized antennas. The relative loss at each frequency includes measured relative loss at two different TX incident angles (20° and 36°). The outdoor marble corner measurement results are compared to prediction by the KED model and the creeping wave model. From the plot, the linear creeping wave

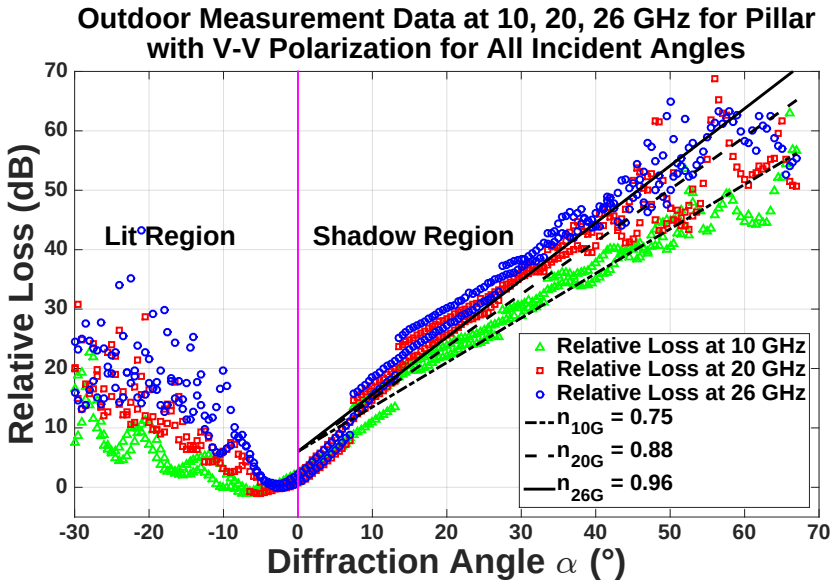

FIGURE 6.4: Outdoor stone pillar diffraction measurement results compared to the KED model at 10, 20, and 26 GHz for V-V polarized antennas.

TABLE 6.1: Mean error (ME) and standard deviation (SD) between the measurement data with the KED model and the empirical linear creeping wave model predictions for stone pillar in the outdoor environment at 10, 20, and 26 GHz for V-V polarized antennas. "Comb." means measurement data that combines data from all incident angles.

Frequency (GHz)	Incident Angle (°)	KED		Linear	
		ME (dB)	SD (dB)	ME (dB)	SD (dB)
10	12	8.07	8.18	-0.17	2.91
	23	5.12	6.52	0.29	2.54
	Comb.	6.76	7.49	0.03	2.75
20	12	9.49	10.20	-0.47	4.92
	23	7.83	7.80	1.62	3.40
	Comb.	8.51	9.23	0.45	4.31
26	12	11.06	11.00	-0.49	4.53
	23	8.42	9.24	1.70	3.12
	Comb.	9.89	10.26	0.48	3.97

model provides a better fit to the measured relative diffraction loss in the shadow region than the KED model. The main mechanisms in the lit region are direct transmission through free space and reflections in the environment, which are not predicted by the

KED model and the creeping wave model. The slope of the creeping wave model is 0.62, 0.77, and 0.96 at 10, 20, and 26 GHz, respectively, according to Eq.(3.29). The KED model underestimates diffraction for diffraction angles greater than 30°. Table 6.2 provides the mean error (ME) and standard deviation (SD) values for each frequency at different incident angles and for combined incident angles. The ME values for the creeping wave model are close to zero (expect for the 26 GHz measurements), which are much less than the ME values of the KED model, indicating a good overall match between the creeping wave model and the measured data. The SD values for creeping wave model (approximately 3-4 dB) are smaller than the SD values for KED model (approximately 5-9 dB).

Fig. 6.8 shows the outdoor marble corner measurement results compared to the creeping wave model prediction at 10, 20, and 26 GHz for V-V polarized antennas. The relative loss for each frequency includes measured loss at two TX incident angles, and is plotted as a function of diffraction angle. The simple linear creeping wave model provides a reasonable fit for the measurement data in the shadow region and near the shadow boundary. Table 6.4 shows the measured diffraction loss and Table 6.5 shows predicted diffraction loss (by Eq.(3.28)) in a 10° interval for diffraction angles from 0° to 60°. The results show approximately 4.5 dB greater diffraction loss at 26 GHz than 20 GHz, and 8.2 dB greater loss at 20 GHz than 10 GHz in a diffraction angle interval of 20 - 30°, as shown in Table 6.4. For an interval of 50-60 ° diffraction angle, diffraction loss at 26 GHz is approximately 11.7 dB greater than 20 GHz measurements, and diffraction loss at 20 GHz is 5.2 dB greater than 10 GHz measurements. Table 6.6 shows the differences between the measured diffraction loss and predicted diffraction loss. The results show approximately 4.0 dB, 5.2 dB, and 8.2 dB differences at 10, 20, and 26 GHz in a diffraction angle interval of 20 - 30°.

The ME and SD values at 10, 20, and 26 GHz for combined TX incident angles can be found in Table 6.2. The ME values of creeping wave model for combined incident angles are small, indicating a good match to the measurement results. Table 6.3 provides the

slope values of the empirical creeping wave MMSE model at 10, 20, and 26 GHz. The measurement conducted at the material with a rougher surface (stone) at 10 and 20 GHz resulted in a larger slope value than the material with a smoother surface (marble). The slope values of the creeping wave model were observed to increase with frequency and the roughness of the diffracted surface. Typically slop values found in the measurements ranged from 0.6 to 1, which can be considered as empirical values used in ray tracing tools. The ME values for creeping wave model in both stone pillar and marble corner are close to zero, indicating a good overall match between the linear creeping wave model and the measured data. Penetration through the marble corner are more dominant than the stone pillar, resulting in higher SD values and more obvious oscillation patterns in the marble corner measurement.

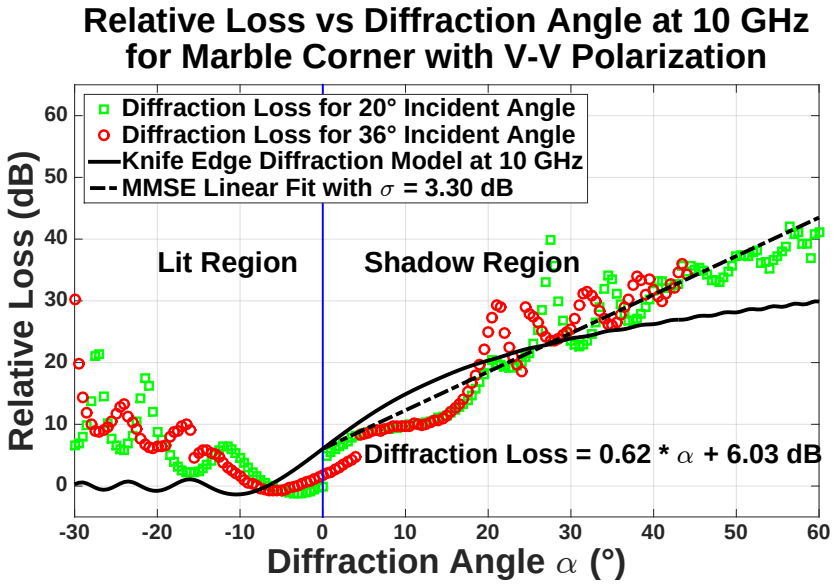

FIGURE 6.5: Outdoor marble corner diffraction measurement results compared to the KED model and the empirical linear creeping wave model at 10 GHz for V-V polarized antennas. 0.62 is the slope value n in the creeping wave model calculated from Eq.(3.29).

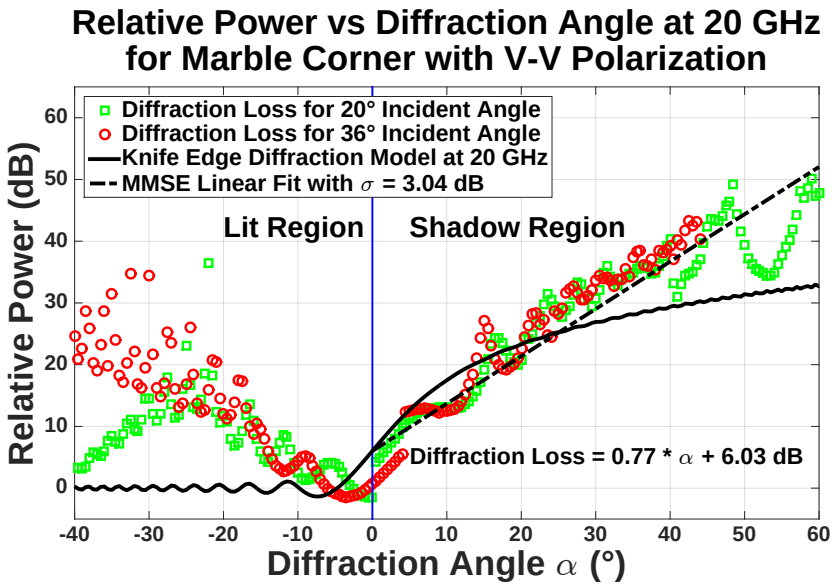

FIGURE 6.6: Outdoor marble corner diffraction measurement results compared to the KED model and the empirical linear creeping wave model at 10 GHz for V-V polarized antennas. 0.77 is the slope value n in the creeping wave model calculated from Eq.(3.29).

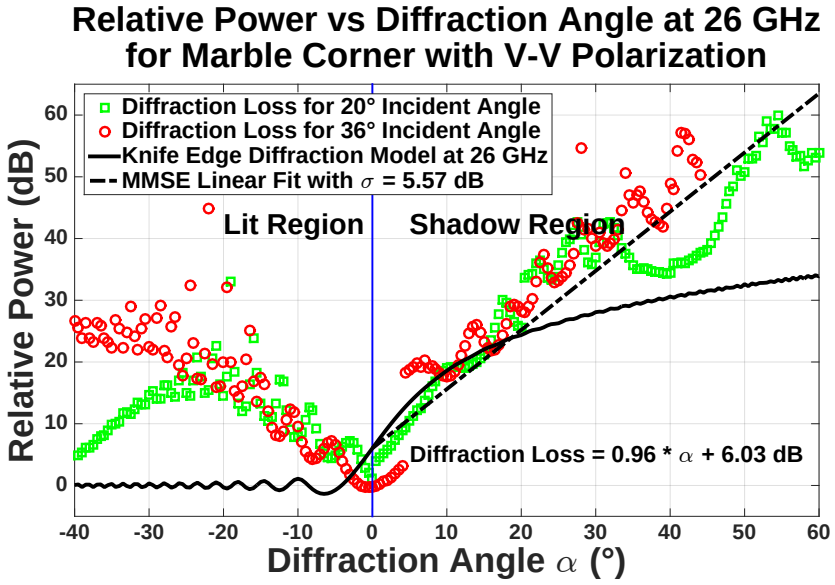

FIGURE 6.7: Outdoor marble corner diffraction measurement results compared to the KED model and the empirical linear creeping wave model at 10 GHz for V-V polarized antennas. 0.95 is the slope value n in the creeping wave model calculated from Eq.(3.29).

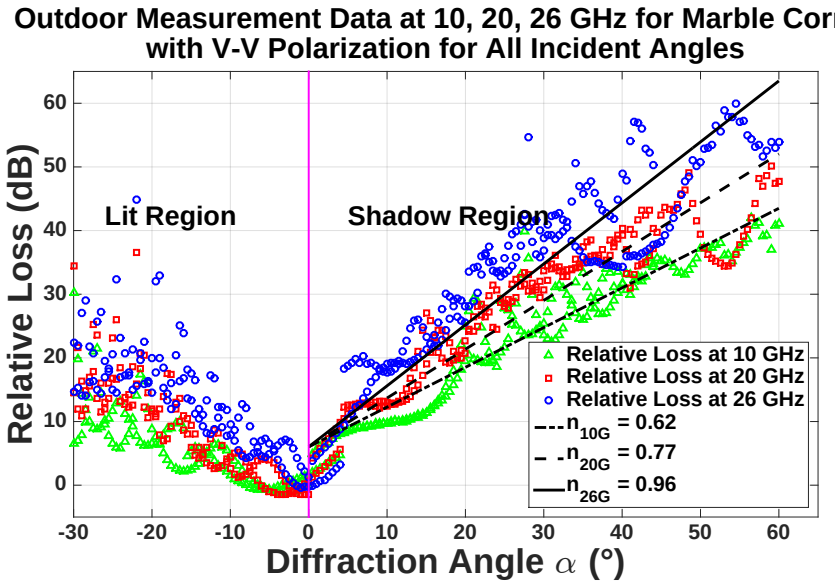

FIGURE 6.8: Outdoor marble corner diffraction measurement results compared to the KED model at 10, 20, and 26 GHz for V-V polarized antennas.

TABLE 6.2: Mean error (ME) and standard deviation (SD) between the measurement data with the KED model and the empirical linear creeping wave model predictions for marble corner in the outdoor environment at 10, 20, and 26 GHz for V-V polarized antennas. "Comb." means measurement data that combines data from all incident angles. CW stands for the creeping wave model.

Frequency (GHz)	Incident Angle (°)	KED		CW	
		ME (dB)	SD (dB)	ME (dB)	SD (dB)
10	20	2.09	5.80	-0.66	3.17
	36	0.20	4.94	0.09	3.48
	Comb.	1.28	5.45	-0.34	3.30
20	20	3.94	5.96	-0.34	4.53
	36	2.38	5.66	1.77	3.04
	Comb.	3.28	5.84	0.55	3.97
26	20	8.01	8.34	4.79	5.01
	36	7.57	8.83	7.98	6.26
	Comb.	7.82	8.55	6.14	5.57

6.2 Outdoor H-V Polarization Measurement Results

6.2.1 Stone Pillar Measurements

Fig. 6.9, Fig. 6.10, and Fig. 6.11 show the measured relative diffraction losses at 10, 20, and 26 GHz, respectively, as a function of diffraction angle at a stone pillar for H-V

TABLE 6.3: The slope values (calculated from Eq.(3.29)) of the linear creeping wave model for the stone pillar and marble corner measurements at 10, 20, and 26 GHz for V-V polarized antennas.

Frequency (GHz)	**Stone**	**Marble**
10	**0.76**	**0.63**
20	**0.90**	**0.78**
26	**0.98**	**0.98**

TABLE 6.4: Average measured diffraction loss (in dB) in a 10° interval for diffraction angles from 0° to 60° for stone pillar and marble corner at 10, 20, and 26 GHz. "Comb." means taking average value from the two different materials. The average values are taken by converting the power levels measured in dB scale to linear scale, then calculating average values in linear scale, and converting the values back to dB scale.

Material	**Frequency (GHz)**	**Diffraction Angle(°)**					
		0-10	**10-20**	**20-30**	**30-40**	**40-50**	**50-60**
Stone	**10**	**9.24**	**20.22**	**27.03**	**34.36**	**40.71**	**46.98**
	20	**10.81**	**23.95**	**32.12**	**40.33**	**51.22**	**59.74**
	26	**11.61**	**25.50**	**34.26**	**43.23**	**53.89**	**59.78**
Marble	**10**	**8.00**	**15.42**	**28.35**	**29.94**	**34.31**	**38.81**
	20	**13.91**	**23.70**	**32.93**	**39.18**	**43.66**	**44.02**
	26	**15.47**	**24.98**	**41.05**	**42.92**	**49.29**	**55.72**
Comb.	**10**	**8.66**	**18.45**	**27.74**	**32.69**	**32.04**	**37.13**
	20	**12.63**	**23.83**	**32.54**	**39.79**	**48.91**	**56.84**
	26	**13.96**	**25.25**	**38.87**	**43.08**	**52.17**	**58.21**

polarized antennas. The relative loss at each frequency includes measured relative loss at two different TX incident angles (12° and 23°). The cross-polarization discrimination factors (XPD) are extracted from all H-V measurements. For H-V polarized antennas, the diffraction loss increased with frequency and diffraction angle. The depolarization effect of the diffracted wave is obvious in the deep shadow region (for diffraction angle greater than 30°). By extracting XPD from the measured H-V data, the relative

TABLE 6.5: Average predicted diffraction loss (in dB) using the creeping wave linear model by Eq.(3.28) in a 10° interval for diffraction angles from 0° to 60° for stone pillar and marble corner at 10, 20, and 26 GHz. "Comb." means taking average value from the two different materials. The average values are taken by converting the power levels measured in dB scale to linear scale, then calculating average values in linear scale, and converting the values back to dB scale.

Material	Frequency (GHz)	Diffraction Angle(°)					
		0-10	10-20	20-30	30-40	40-50	50-60
Stone	10	10.11	17.60	25.10	32.59	40.08	47.57
	20	10.94	19.77	28.60	37.42	46.25	55.08
	26	11.45	21.07	30.69	40.31	49.93	59.55
Marble	10	9.36	15.61	21.85	28.10	34.34	43.18
	20	10.22	17.89	25.56	33.22	40.89	48.56
	26	11.42	21.00	30.58	40.17	49.75	59.33
Comb.	10	9.75	16.72	23.77	30.90	38.10	45.91
	20	10.59	18.93	27.34	35.81	44.35	52.94
	26	11.44	21.04	30.64	40.24	49.84	59.44

diffraction losses agree well with the KED model.

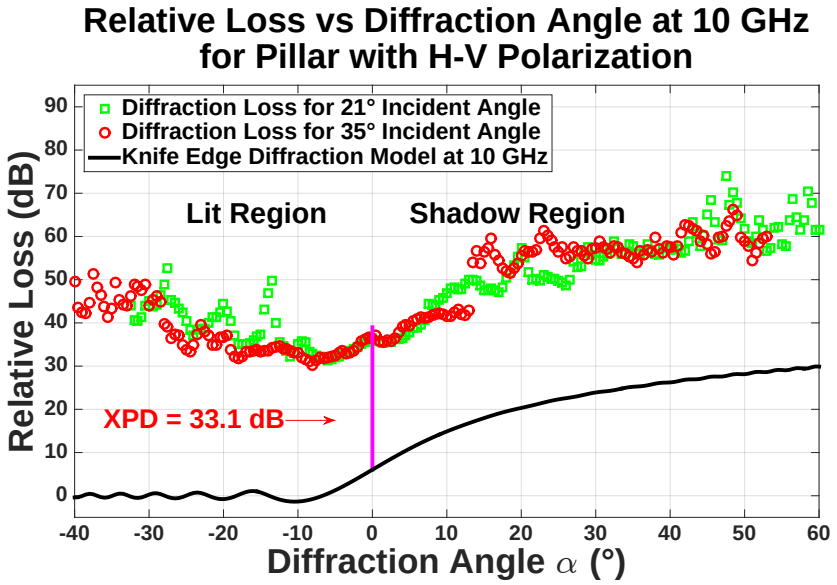

FIGURE 6.9: Outdoor stone pillar diffraction measurement results compared to the KED model at 10 GHz for H-V polarized antennas.

TABLE 6.6: Differences between the measured diffraction loss and predicted diffraction loss (in dB) in a 10° interval for diffraction angles from 0° to 60° for stone pillar and marble corner at 10, 20, and 26 GHz. "Comb." means taking average value from the two different materials. The average values are taken by converting the power levels measured in dB scale to linear scale, then calculating average values in linear scale, and converting the values back to dB scale.

Material	Frequency (GHz)	Diffraction Angle(°)					
		0-10	10-20	20-30	30-40	40-50	50-60
Stone	10	-0.87	2.62	1.93	1.77	0.63	-0.59
	20	-0.13	4.18	3.52	2.91	4.97	4.66
	26	0.16	4.43	3.57	2.92	3.96	0.23
Marble	10	-1.36	-0.19	6.50	1.84	-0.03	-4.37
	20	3.69	5.81	7.37	5.96	2.77	-4.54
	26	4.05	3.98	10.47	2.75	-0.46	-3.61
Comb.	10	-1.09	1.73	3.97	1.79	-6.06	-8.78
	20	2.04	4.90	5.20	3.98	4.56	3.90
	26	2.52	4.21	8.23	2.84	2.33	-1.23

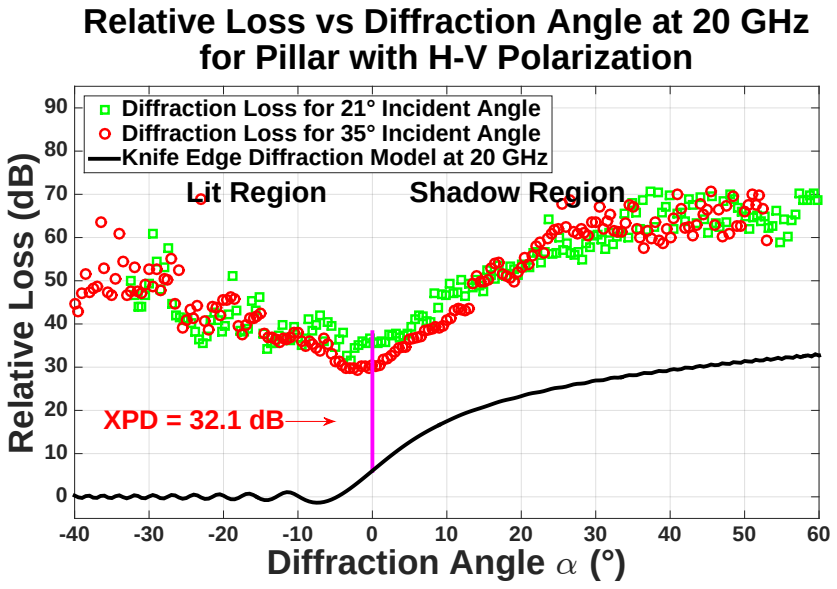

FIGURE 6.10: Outdoor stone pillar diffraction measurement results compared to the KED model at 20 GHz for H-V polarized antennas.

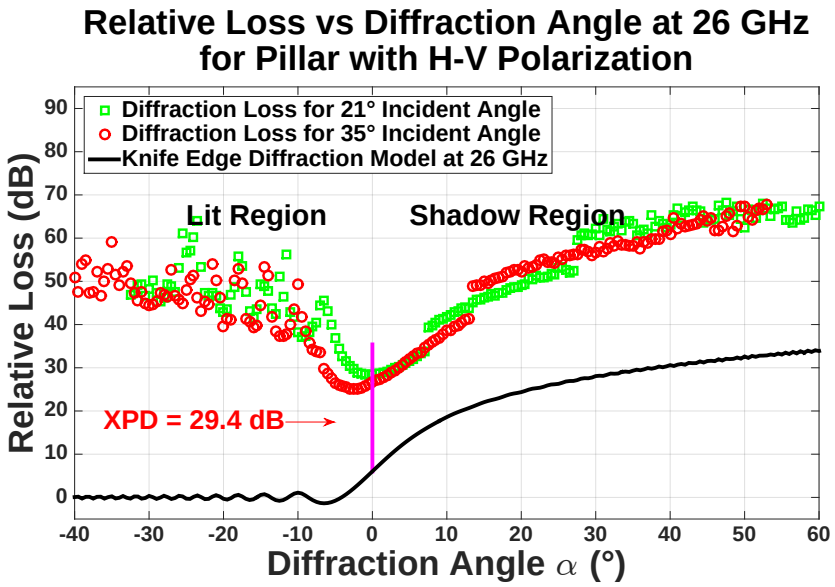

FIGURE 6.11: Outdoor stone pillar diffraction measurement results compared to the KED model at 26 GHz for H-V polarized antennas.

6.2.2 Marble Corner Measurements

Fig. 6.12, Fig. 6.13, and Fig. 6.14 show the measured relative diffraction losses at 10, 20, and 26 GHz, respectively, as a function of diffraction angle at a marble corner for H-V polarized antennas. The relative loss at each frequency includes measured relative loss at two different TX incident angles (12° and 23°). The cross-polarization discrimination factors (XPD) are extracted from all H-V measurements. For H-V polarized antennas, the diffraction loss increased with frequency (expect for the 26 GHz measurements) and diffraction angle. The depolarization effect of the diffracted wave is obvious in the deep shadow region (for diffraction angle greater than 30°). By extracting XPD from the measured H-V data, the relative diffraction losses agree well with the KED model.

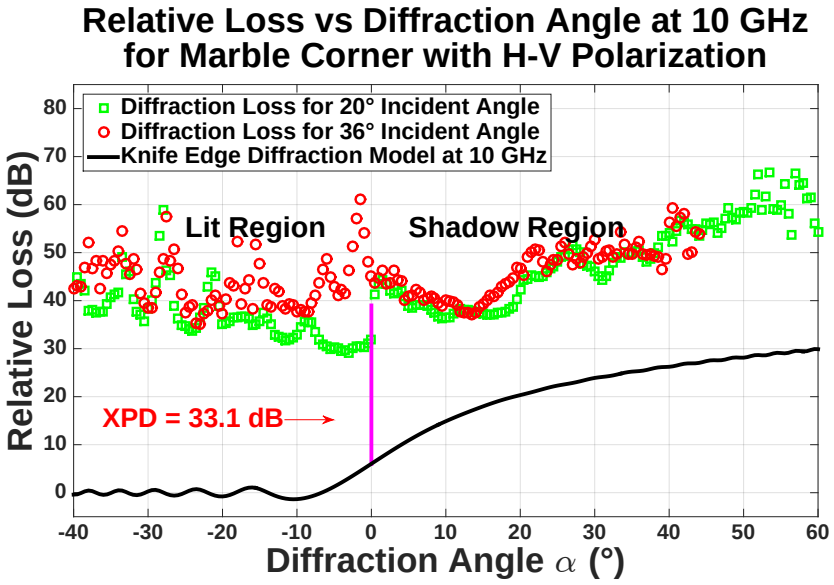

FIGURE 6.12: Outdoor marble corner diffraction measurement results compared to the KED model at 10 GHz for H-V polarized antennas.

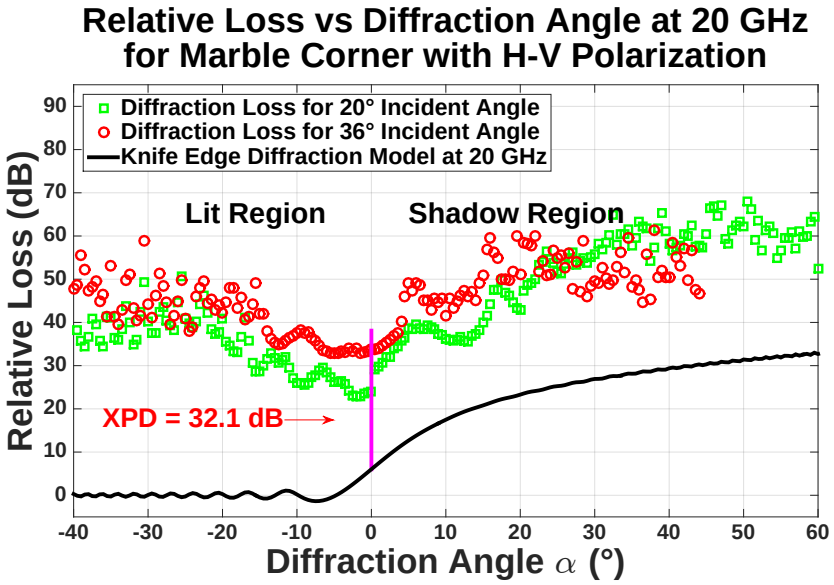

FIGURE 6.13: Outdoor marble corner diffraction measurement results compared to the KED model at 20 GHz for H-V polarized antennas.

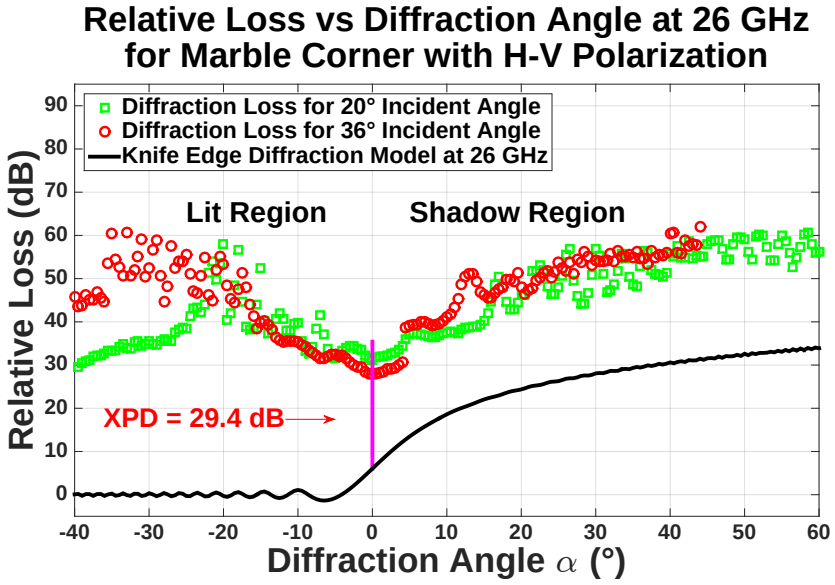

FIGURE 6.14: Outdoor marble corner diffraction measurement results compared to the KED model at 26 GHz for H-V polarized antennas.

Chapter 7

Conclusion

This report presented indoor and outdoor diffraction measurements conducted for different materials (drywall, wood, plastic, stone, and marble) at 10, 20, and 26 GHz. The measurements were performed in order to understand, quantify and model the behavior of diffraction mechanism, and to develop accurate and general diffraction loss models with simple calculation, which can be used in building ray tracers for cmWave and mmWave. This report presented two diffraction models, namely the Knife Edge Diffraction model and the empirical linear creeping wave model. The knife edge diffraction model is applicable to corners with sharp edges, and is commonly used in ray tracing tools due to its simplicity and accuracy for diffraction loss prediction. The empirical linear creeping wave model is applicable to building features that exhibit curved and rounded surfaces. The linear creeping wave model has a fixed anchor point of 6 dB (from diffraction loss at a diffraction angle of 0° in the KED model) and a variable slope value was obtained from measurement data using minimum mean square error (MMSE) estimation.

The indoor measurements around the drywall corner showed a relatively good agreement between the measured relative diffraction loss and prediction by the KED model with approximately 5-6 dB standard deviations for all frequencies, incident angles, and materials tested. For measurements conducted around the wooden corner, the KED model

overestimated the relative diffraction loss (by approximately 4 dB) in the shadow region and near the shadow boundary (the KED model is not sufficient for predicting relative loss in the lit region). Diffraction around an irregular object, such as plastic board, followed a trend similar to the KED prediction, but not as well as the regular 90° corner. Theoretical KED analysis as described by (3.7) would predict that for an interval of 30 - 40° diffraction angle, 20 GHz would have on average (taking average of the measured three materials) 1.1 dB more loss than at 26 GHz, and that 20 GHz would have 4.0 dB more loss than at 10 GHz. The results also showed approximately -3.2 dB, -2.2 dB, and -4.5 dB differences between the measured diffraction loss and predicted diffraction loss by the KED model at 10, 20, and 26 GHz in a diffraction angle interval of 30 - 40°. Due to the reflective indoor environment and penetration through the measured materials, the relative diffraction loss was observed to be less dependent on frequency than might be expected. This clearly shows how indoor environments have less diffraction loss over frequency than predicted by the KED model. As shown in Chapter 5, the KED model can be used in ray tracing tools to calculate diffraction loss (along with a random varying component modeled as nearly 0 mean Gaussian random variable with 5-6 dB standard deviation) in the indoor environment at 10, 20 and 26 GHz. For objects with irregular shapes, the KED model can also be used in ray tracing tools to predict diffraction loss (but keeping in mind about 2 - 4 dB overestimation error, which could be subtracted out).

The work here showed that diffraction loss for an outdoor building corner with rounded edges can be better predicted by a simple linear creeping wave model rather than the KED model. The slope of the creeping wave model increased with frequency, and the material with a rougher surface (stone) had a larger slope value than the material with a smoother surface (marble) at the same frequency. The creeping wave model analysis as described by (3.28) would predict that for an interval of 30 - 40° diffraction angle, 26 GHz would have 2.9 dB (for stone pillar) and 7.0 dB (for marble corner) more loss than at 20 GHz, and that 20 GHz would have 4.9 dB (for stone pillar) and 5.1 dB (for marble corner) more loss than at 10 GHz. For an interval of 30 - 40° diffraction angle,

the results showed that 26 GHz would have on average (taking average of the measured two materials) 4.4 dB more loss than at 20 GHz, and that 20 GHz would have 4.9 dB more loss than at 10 GHz. The results also showed approximately 1.8 dB, 3.0 dB, and 2.8 dB differences between the measured diffraction loss and predicted diffraction loss by the creeping wave model at 10, 20, and 26 GHz in a diffraction angle interval of 30 - 40°. Given in Chapter 6, the creeping wave model, as a function of diffraction angle, is empirically based, but the model can be used in ray tracing tools, by introducing typical slope values ranged from 0.6 to 1 found in the measurements.

The cross-polarization discrimination factors (XPD) were extracted from all H-V measurements. For H-V polarized antennas, the diffraction loss increased with frequency, but for each frequency, the diffraction loss was relatively independent of diffraction angle, indicating a depolarization effect of the diffracted wave in the shadow region in the indoor environment. In general, we showed in Chapter 5 and 6 that due to the depolarization effect, the prediction by KED theory overestimates the diffraction loss in the H-V scenario. The indoor results showed that for a 30° diffraction angle, 26 GHz would have 0.9 dB more loss than at 20 GHz, and that 20 GHz would have 1.2 dB more loss than at 10 GHz. This clearly shows the relative diffraction loss for cross-polarization configuration was observed to be less dependent on frequency than might be expected. By comparing the KED prediction and the corresponding XPD values to the average measured relative diffraction loss for H-V polarization, the KED overestimate the measured data by 13.8 dB, 14.0 dB and 1.3 dB at 10. 20, and 26 GHz, respectively. The diffraction losses were observed to increase with frequency and diffraction angle in the outdoor environment. The outdoor results showed that for a 30° diffraction angle, 26 GHz would have on average 5.5 dB more loss than at 20 GHz, and that 20 GHz would have 1.1 dB more loss than at 10 GHz. By comparing the KED prediction and the corresponding XPD values to the average measured relative diffraction loss for H-V polarization, the KED overestimate the measured data by 5.4 dB, 1.0 dB and 0.6 dB at 10. 20, and 26 GHz, respectively. Chapter 5 and 6 showed that the depolarization effect of the diffracted wave is obvious in the deep shadow region (for diffraction angle greater

than 30°). By extracting the XPD from the measured H-V data, the relative diffraction losses agree well with the KED model.

The simple KED model and linear creeping wave model can be used in indoor and outdoor environments, respectively, to estimate propagation loss due to diffraction by building corners for network simulations and ray-tracers with good accuracy and easy calculation. According to the measurements provided in this report, diffraction is expected to be less important at mmWave than cmWave due to smaller wavelengths, and diffraction is not a major propagation mechanism in microcell and femtocell deployments with directional antennas. This work showed that in the indoor environment for an interval of 30 - 40°, the results showed 3.2 dB, 2.2 dB, and 4.5 dB less diffraction loss than predicted by the KED model at 10, 20, and 26 GHz, respectively. The outdoor measurement showed 1.8 dB, 3.0 dB, and 2.8 dB more diffraction loss than the predicted values calculated by the creeping wave model at 10, 20, and 26 GHz, respectively, in a diffraction angle interval of 30 - 40°. The results will allow wireless engineers to accurately model the propagation mechanism of diffraction for various materials at 10, 20, and 26 GHz when designing systems for cmWave and mmWave deployment.

Appendix A

Measurement Database Description

A.1 Folders Structure Hierarchy

The flow diagram of the folder structure hierarchy is shown in Fig. A.1, where the initial base folder contains the `Diffraction Measurement Data` with all associated indoor and outdoor measurements in the subfolders. Inside the `Indoor Measurement Data` and `Outdoor Measurement Data` folders are frequency subfolders (`10 GHz`, `20 GHz`, and `26 GHz`) and static information file (`Indoor_Static_Info.xlsx` or `Outdoor_Static_Info.xlsx`). Inside the frequency subfolders are measurement location subfolders (Location 1, Location 2, and/or Location 3), corresponding to different material types. Located in the measurement location folders are raw data files, labeled as `Diff_26GHz_L2_M2_HV.txt` for instant, where L indicates the measurement location number for different material types, M indicates measurement number for different TX incident angles, and HV indicates horizontal-to-vertical polarization combination. Each measurement location folder includes measurement at two or three incident angles for two antenna polarization combinations (VV and HV).

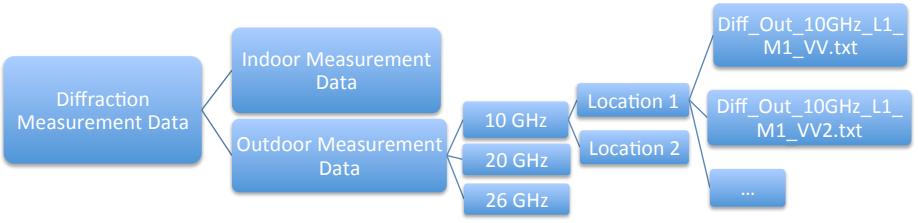

FIGURE A.1: File structure hierarchy from the main base folder down to the specific measurement folder. Each of the boxes in the figure represents a folder.

A.2 Measurement Data Files

Each measurement raw data file includes data for two or three TX incident angles and two antenna polarization combinations. For each TX incident angle and antenna polarization combination, a total of 200 diffraction angles were measured, in step increment of 0.5°, corresponding to a total of 100° measured diffraction angles. An example of the raw data file is shown in Fig. A.2, where the first column contains diffraction angle α in degree and the second column contains relative diffraction loss measured in decibel. The relative diffraction loss is obtained by subtracting free space path loss at 3 m distance (equals $d_1 + d_2$) from the measured path loss using spectrum analyzer at different diffraction angles.

A.3 Measurement Static Information Files

In addition to the collected raw data, complimentary static information files are provided for each measurement, for each measurement location (L1, L2, and/or L3), at each TX incident angle (M1, M2, and/or M3), and for each antenna polarization combination (VV and HV). An example row of the static information file is shown in Fig. A.3, which refers to a measurement file with the following settings and configuration:

```
Alpha (degree) Diffraction Loss (dB)
44.0000  50.3620
43.5000  52.2450
43.0000  52.8089
42.5000  56.0963
42.0000  56.9241
41.5000  57.0940
41.0000  54.1292
40.5000  47.9009
40.0000  48.8910
39.5000  44.7891
39.0000  41.8330
38.5000  42.3350
38.0000  42.7434
37.5000  43.1303
37.0000  44.2905
36.5000  45.8851
36.0000  47.7160
35.5000  46.9950
35.0000  45.7132
34.5000  47.0081
34.0000  50.6069
33.5000  44.5000
33.0000  41.4450
32.5000  39.8770
32.0000  39.3070
```

FIGURE A.2: Example of .txt raw data file for one TX incident angle and antenna polarization combination measurement acquired during the measurement campaign.

- Frequency: 26 GHz
- Location: 2
- Measurement: 2
- Material: Marble
- TX Height (m): 1.4
- RX Height (m): 1.4
- TX Polarization: H
- TX Polarization: V
- d_1 (m): 1.4
- d_2 (m): 1.4

- beta (degrees)

- Filename: $Diff\_Out\_26GHz\_L2\_M2\_HV.txt$

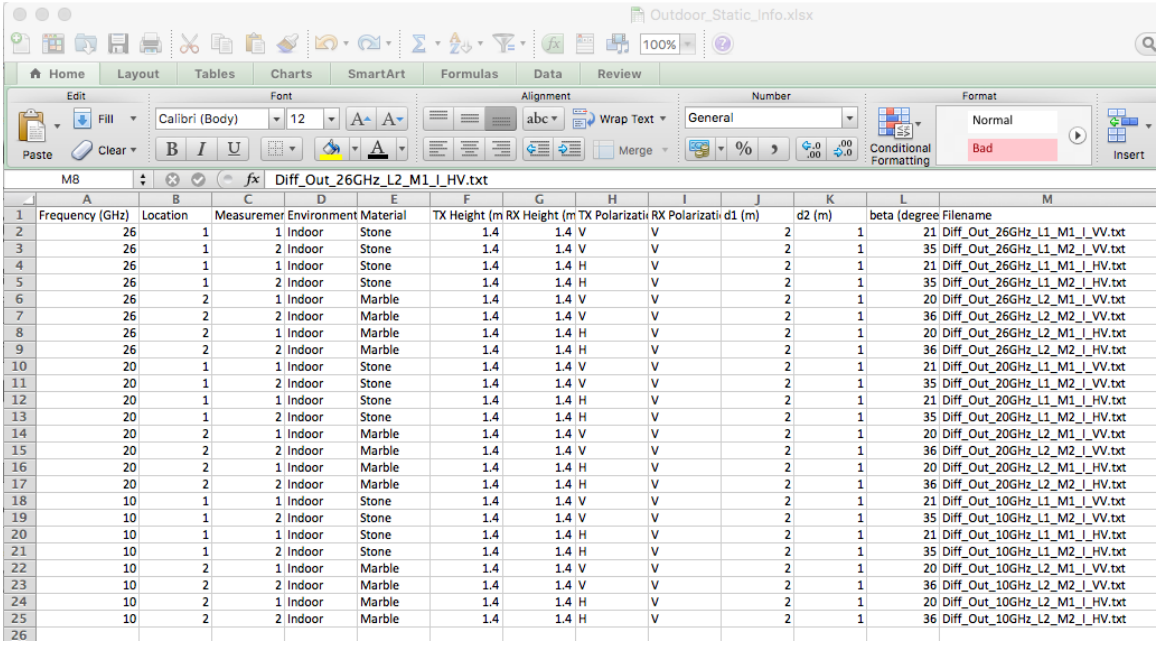

	A	B	C	D	E	F	G	H	I	J	K	L	M
1	Frequency (GHz)	Location	Measuremer	Environment	Material	TX Height (m	RX Height (m	TX Polarizati	RX Polarizati	d1 (m)	d2 (m)	beta (degree	Filename
2	26	1	1	Indoor	Stone	1.4	1.4	V	V	2	1	21	Diff_Out_26GHz_L1_M1_I_VV.txt
3	26	1	2	Indoor	Stone	1.4	1.4	V	V	2	1	35	Diff_Out_26GHz_L1_M2_I_VV.txt
4	26	1	1	Indoor	Stone	1.4	1.4	H	V	2	1	21	Diff_Out_26GHz_L1_M1_I_HV.txt
5	26	1	2	Indoor	Stone	1.4	1.4	H	V	2	1	35	Diff_Out_26GHz_L1_M2_I_HV.txt
6	26	2	1	Indoor	Marble	1.4	1.4	V	V	2	1	20	Diff_Out_26GHz_L2_M1_I_VV.txt
7	26	2	2	Indoor	Marble	1.4	1.4	V	V	2	1	36	Diff_Out_26GHz_L2_M2_I_VV.txt
8	26	2	1	Indoor	Marble	1.4	1.4	H	V	2	1	20	Diff_Out_26GHz_L2_M1_I_HV.txt
9	26	2	2	Indoor	Marble	1.4	1.4	H	V	2	1	36	Diff_Out_26GHz_L2_M2_I_HV.txt
10	20	1	1	Indoor	Stone	1.4	1.4	V	V	2	1	21	Diff_Out_20GHz_L1_M1_I_VV.txt
11	20	1	2	Indoor	Stone	1.4	1.4	V	V	2	1	35	Diff_Out_20GHz_L1_M2_I_VV.txt
12	20	1	1	Indoor	Stone	1.4	1.4	H	V	2	1	21	Diff_Out_20GHz_L1_M1_I_HV.txt
13	20	1	2	Indoor	Stone	1.4	1.4	H	V	2	1	35	Diff_Out_20GHz_L1_M2_I_HV.txt
14	20	2	1	Indoor	Marble	1.4	1.4	V	V	2	1	20	Diff_Out_20GHz_L2_M1_I_VV.txt
15	20	2	2	Indoor	Marble	1.4	1.4	V	V	2	1	36	Diff_Out_20GHz_L2_M2_I_VV.txt
16	20	2	1	Indoor	Marble	1.4	1.4	H	V	2	1	20	Diff_Out_20GHz_L2_M1_I_HV.txt
17	20	2	2	Indoor	Marble	1.4	1.4	H	V	2	1	36	Diff_Out_20GHz_L2_M2_I_HV.txt
18	10	1	1	Indoor	Stone	1.4	1.4	V	V	2	1	21	Diff_Out_10GHz_L1_M1_I_VV.txt
19	10	1	2	Indoor	Stone	1.4	1.4	V	V	2	1	35	Diff_Out_10GHz_L1_M2_I_VV.txt
20	10	1	1	Indoor	Stone	1.4	1.4	H	V	2	1	21	Diff_Out_10GHz_L1_M1_I_HV.txt
21	10	1	2	Indoor	Stone	1.4	1.4	H	V	2	1	35	Diff_Out_10GHz_L1_M2_I_HV.txt
22	10	2	1	Indoor	Marble	1.4	1.4	V	V	2	1	20	Diff_Out_10GHz_L2_M1_I_VV.txt
23	10	2	2	Indoor	Marble	1.4	1.4	V	V	2	1	36	Diff_Out_10GHz_L2_M2_I_VV.txt
24	10	2	1	Indoor	Marble	1.4	1.4	H	V	2	1	20	Diff_Out_10GHz_L2_M1_I_HV.txt
25	10	2	2	Indoor	Marble	1.4	1.4	H	V	2	1	36	Diff_Out_10GHz_L2_M2_I_HV.txt
26													

FIGURE A.3: Example of .xlsx static information file for indoor measurements.

Bibliography

[1] T. S. Rappaport, R. W. Heath, Jr., R. C. Daniels, and J. N. Murdock, *Millimeter Wave Wireless Communications*. Pearson/Prentice Hall, 2015.

[2] T. S. Rappaport, *Wireless Communications: Principles and Practice*, 2nd ed. Upper Saddle River, NJ: Prentice Hall, 2002.

[3] J. Ryan, G. R. MacCartney, Jr., and T. Rappaport, "Partition-based path loss models from indoor office wideband measurements at 28 GHz and 73 GHz," in *IEEE Global Telecommunications Conference (GLOBECOM)*, Dec. 2016, submitted paper.

[4] Z. Pi and F. Khan, "An introduction to millimeter-wave mobile broadband systems," *IEEE Communications Magazine*, vol. 49, no. 6, pp. 101–107, June 2011.

[5] Samsung Electronics, "Millimeter waves may be the future of 5G phones," June 2013. [Online]. Available: http://spectrum.ieee.org/telecom/wireless/millimeter-waves-may-be-the-future-of-5g-phones

[6] Nokia Solutions and Networks, "FutureWorks NSN White Paper: Looking ahead to 5G," Dec. 2013. [Online]. Available: http://networks.nokia.com/file/28771/5g-white-paper

[7] T. S. Rappaport, S. Sun, R. Mayzus, H. Zhao, Y. Azar, K. Wang, G. N. Wong, J. K. Schulz, M. K. Samimi, and F. Gutierrez, Jr., "Millimeter Wave Mobile Communications for 5G Cellular: It Will Work!" *IEEE Access*, vol. 1, pp. 335–349, 2013.

[8] M. K. Samimi, K. Wang, Y. Azar, G. N. Wong, R. Mayzus, H. Zhao, J. K. Schulz, S. Sun, F. Gutierrez, Jr., and T. S. Rappaport, "28 GHz angle of arrival and angle of departure analysis for outdoor cellular communications using steerable beam antennas in New York City," in *2013 IEEE 77th Vehicular Technology Conference (VTC Spring)*, June 2013, pp. 1–6.

[9] G. R. MacCartney, Jr. and T. S. Rappaport, "73 GHz millimeter wave propagation measurements for outdoor urban mobile and backhaul communications in New York City," in *2014 IEEE International Conference on Communications (ICC)*, June 2014, pp. 4862–4867.

[10] G. R. Maccartney, T. S. Rappaport, S. Sun, and S. Deng, "Indoor office wideband millimeter-wave propagation measurements and channel models at 28 and 73 GHz for ultra-dense 5g wireless networks," *IEEE Access*, vol. 3, pp. 2388–2424, 2015.

[11] T. S. Rappaport, G. R. MacCartney, M. K. Samimi, and S. Sun, "Wideband millimeter-wave propagation measurements and channel models for future wireless communication system design (invited paper)," *IEEE Transactions on Communications*, vol. 63, no. 9, pp. 3029–3056, Sept. 2015.

[12] H. L. Bertoni, *Radio propagation for modern wireless systems.* Pearson Education, 1999.

[13] H. Zhao, R. Mayzus, S. Sun, M. Samimi, J. Schulz, Y. Azar, K. Wang, G. Wong, F. Gutierrez, and T. S. Rappaport, "28 GHz millimeter wave cellular communication measurements for reflection and penetration loss in and around buildings in new york city," in *IEEE International Conference on Communications (ICC)*, June 2013, pp. 5163–5167.

[14] W. Asen, "Comparison of measurements with prediction methods for propagation by diffraction at 88-108 MHz," *IEEE Transactions on Antennas and Propagation*, vol. 52, no. 6, pp. 1499–1504, June 2004.

[15] T. Russell, C. Bostian, and T. Rappaport, "A deterministic approach to predicting microwave diffraction by buildings for microcellular systems," *IEEE Transactions on Antennas and Propagation*, vol. 41, no. 12, pp. 1640–1649, Dec. 1993.

[16] W. Zhang, "Fast two-dimensional diffraction modeling for site-specific propagation prediction in urban microcellular environments," *IEEE Transactions on Vehicular Technology*, vol. 49, no. 2, pp. 428–436, Mar. 2000.

[17] N. Tervo, C. Dias, V. Hovinen, M. Sonkki, A. Roivainen, J. Meinila, and M. Latva-aho, "Diffraction measurements around a building corner at 10 GHz," in *2014 1st International Conference on 5G for Ubiquitous Connectivity (5GU)*, Nov. 2014, pp. 187–191.

[18] P. Tenerelli and C. Bostian, "Measurements of 28 GHz diffraction loss by building corners," in *The Ninth IEEE International Symposium on Personal, Indoor and Mobile Radio Communications*, vol. 3, Sep. 1998, pp. 1166–1169.

[19] A. Alejos, M. Sanchez, and I. Cuinas, "Measurement and analysis of propagation mechanisms at 40 GHz: Viability of site shielding forced by obstacles," *IEEE Transactions on Vehicular Technology*, vol. 57, no. 6, pp. 3369–3380, Nov. 2008.

[20] M. Jacob, S. Priebe, R. Dickhoff, T. Kleine-Ostmann, T. Schrader, and T. Kurner, "Diffraction in mm and sub-mm wave indoor propagation channels," *IEEE Transactions on Microwave Theory and Techniques*, vol. 60, no. 3, pp. 833–844, March 2012.

[21] J. Lu, P. Cabrol, D. Steinbach, and R. Pragada, "Measurement and characterization of various outdoor 60 GHz diffracted and scattered paths," in *IEEE Military Communications Conference (MILCOM)*, Nov. 2013, pp. 1238–1243.

[22] J. Hansryd, J. Edstam, B.-E. Olsson, and C. Larsson, "Non-line-of-sight microwave backhaul for small cells," *Ericsson Review*, vol. 22, 2013.

[23] A. Maltsev, R. Maslennikov, A. Sevastyanov, A. Lomayev, A. Khoryaev, A. Davydov, and V. Ssorin, "Characteristics of indoor millimeter-wave channel at 60 ghz in

application to perspective wlan system," in *2010 Proceedings of the Fourth European Conference on Antennas and Propagation (EuCAP)*, April 2010, pp. 1–5.

[24] A. Maltsev, E. Perahia, R. Maslennikov, A. Sevastyanov, A. Lomayev, and A. Khoryaev, "Impact of polarization characteristics on 60-GHz indoor radio communication systems," *IEEE Antennas and Wireless Propagation Letters*, vol. 9, pp. 413–416, 2010.

[25] H. Sawada, S. Kato, K. Sato, H. Harada *et al.*, "Intra-cluster response model and parameter for channel modeling at 60 ghz (part 3)," *IEEE Document*, pp. 802–11, 2010.

[26] M. Kvicera, P. Valtr, T. Korinek, P. Pechac, M. Grabner, V. Kvicera, and A. Martellucci, "Short-term terrain diffraction measurements: Preliminary results," in *European Conference on Antennas and Propagation (EuCAP)*, April 2013, pp. 52–55.

[27] I. Rodriguez, H. C. Nguyen, T. B. Sorensen, J. Elling, J. A. Holm, P. Mogensen, P. Mogensen, and B. Vejlgaard, "Analysis of 38 ghz mmwave propagation characteristics of urban scenarios," in *Proceedings of European Wireless Conference*, May 2015, pp. 1–8.

[28] R. Luebbers, "Finite conductivity uniform gtd versus knife edge diffraction in prediction of propagation path loss," *IEEE Transactions on Antennas and Propagation*, vol. 32, no. 1, pp. 70–76, Jan. 1984.

[29] P. Pathak, G. Carluccio, and M. Albani, "The uniform geometrical theory of diffraction and some of its applications," *IEEE Antennas and Propagation Magazine*, vol. 55, no. 4, pp. 41–69, Aug 2013.

[30] R. Kouyoumjian and P. Pathak, "A uniform geometrical theory of diffraction for an edge in a perfectly conducting surface," *Proceedings of the IEEE*, vol. 62, no. 11, pp. 1448–1461, Nov. 1974.

[31] H. Wang and T. Rappaport, "A parametric formulation of the UTD diffraction coefficients for a dielectric wedge," in *IEEE Antennas and Propagation Society International Symposium*, vol. 1, June 2004, pp. 962–965.

[32] V. Erceg, A. Rustako, and R. Roman, "Diffraction around corners and its effects on the microcell coverage area in urban and suburban environments at 900 MHz, 2 GHz, and 6 GHz," in *IEEE Global Telecommunications Conference (GLOBECOM)*, Nov. 1994, pp. 52–57.

[33] T. Imai and T. Fujii, "Propagation loss in multiple diffraction using ray-tracing," in *IEEE Antennas and Propagation Society International Symposium*, vol. 4, July 1997, pp. 2572–2575.

[34] R. Luebbers, "Comparison of lossy wedge diffraction coefficients with application to mixed path propagation loss prediction," *IEEE Transactions on Antennas and Propagation*, vol. 36, no. 7, pp. 1031–1034, Jul 1988.

[35] ——, "A heuristic utd slope diffraction coefficient for rough lossy wedges," *IEEE Transactions on Antennas and Propagation*, vol. 37, no. 2, pp. 206–211, 1989.

[36] K. Rizk, J.-F. Wagen, and F. Gardiol, "Two-dimensional ray-tracing modeling for propagation prediction in microcellular environments," *IEEE Transactions on Vehicular Technology*, vol. 46, no. 2, pp. 508–518, 1997.

[37] K. Rizk, R. Valenzuela, D. Chizhik, and F. Gardiol, "Application of the slope diffraction method for urban microwave propagation prediction," in *IEEE Vehicular Technology Conference*, vol. 2. IEEE, 1998, pp. 1150–1155.

[38] K. Remley, H. Anderson, and A. Weisshar, "Improving the accuracy of ray-tracing techniques for indoor propagation modeling," *IEEE Transactions on Vehicular Technology*, vol. 49, no. 6, pp. 2350–2358, Nov 2000.

[39] H. R. Anderson, "Building corner diffraction measurements and predictions using utd," *IEEE Transactions on Antennas and Propagation*, vol. 46, no. 2, pp. 292–293, 1998.

[40] Y. I. Nechayev, C. C. Constantinou, and L. Lukama, "Comparison of measured and theoretical diffracted fields around building corners at 2.4 GHz," in *IEEE Vehicular Technology Conference*, vol. 2, 2001, pp. 728–732.

[41] R. J. Luebbers, "A heuristic UTD slope diffraction coefficient for rough lossy wedges," *IEEE Transactions on Antennas and Propagation*, vol. 37, no. 2, pp. 206–211, Feb. 1989.

[42] H. K. Chung and H. L. Bertoni, "Application of isolated diffraction edge (IDE) method for urban microwave path loss prediction," in *IEEE Vehicular Technology Conference (VTC-Spring)*, vol. 1, April 2003, pp. 205–209.

[43] P. H. Pathak, G. Carluccio, and M. Albani, "The uniform geometrical theory of diffraction and some of its applications," *IEEE Antennas and Propagation Magazine*, vol. 55, no. 4, pp. 41–69, Aug. 2013.

[44] A. G. Kanatas, I. D. Kountouris, G. B. Kostaras, and P. Constantinou, "A UTD propagation model in urban microcellular environments," *IEEE Transactions on Vehicular Technology*, vol. 46, no. 1, pp. 185–193, Feb 1997.

[45] H. M. El-Sallabi, G. Liang, H. L. Bertoni, and P. Vainikainen, "Influence of diffraction coefficient on ray prediction of power and delay spread in urban microcells," in *IEEE Vehicular Technology Conference*, vol. 1, 2002, pp. 16–20.

[46] W. Qu, X. Jia, Z. Weigang, and W. Chong, "Research and simulation of signal diffraction loss based on UTD theory," in *International Congress on Image and Signal Processing (CISP)*, Oct. 2012, pp. 1847–1850.

[47] R. C. Hansen, "Geometric theory of diffraction." *IEEE Press Selected Reprint Series, New York*, vol. 1, 1981.

[48] D. McNamara, C. Pistorius, and J. Malherbe, "The uniform geometrical theory of diffraction," *Artech House, London*, 1990.

[49] S. K. Soni and A. Bhattacharya, "New heuristic diffraction coefficient for modeling of wireless channel," *Progress In Electromagnetics Research*, vol. 12, pp. 125–137, 2010.

[50] J.-F. Rouviere, N. Douchin, and P. F. Combes, "Diffraction by lossy dielectric wedges using both heuristic utd formulations and fdtd," *IEEE Transactions on Antennas and Propagation*, vol. 47, no. 11, pp. 1702–1708, 1999.

[51] L. Piazzi and H. L. Bertoni, "Effect of terrain on path loss in urban environments for wireless applications," *IEEE Transactions on Antennas and Propagation*, vol. 46, no. 8, pp. 1138–1147, Aug. 1998.

[52] S.-W. Lee and G. Deschamps, "A uniform asymptotic theory of electromagnetic diffraction by a curved wedge," *IEEE Transactions on Antennas and Propagation*, vol. 24, no. 1, pp. 25–34, Jan. 1976.

[53] V. A. Borovikov, "Diffraction by impedance wedge with curved faces," in *Proceedings of International Seminar/Workshop on Direct and Inverse Problems of Electromagnetic and Acoustic Wave Theory*, Nov. 1998, pp. 25–27.

[54] J. Keller, "Diffraction of a convex cylinder," *IRE Transactions on Antennas and Propagation*, vol. 4, no. 3, pp. 312–321, July 1956.

[55] T. Negishi, V. Picco, D. Spitzer, D. Erricolo, G. Carluccio, F. Puggelli, and M. Albani, "Measurements to validate the UTD triple diffraction coefficient," *IEEE Transactions on Antennas and Propagation*, vol. 62, no. 7, pp. 3723–3730, July 2014.